UNIVERSITÀ DI TRENTO

FONDAZIONE EDMUND MACH

Doctoral School in
Agrifood and Environmental Sciences

Enrico Pandrin

Laboratory investigation of bedload morphological effects and dynamics under varying flow confinement.

Supervisor(s)
Prof. Walter Bertoldi, Prof. Marco Tubino
Tutor
Prof. Walter Bertoldi

37 Cycle, 2021

To those we love

ACKNOWLEDGMENTS

I would like to begin by expressing my deepest gratitude to my supervisors, Professor Walter Bertoldi and Professor Marco Tubino. Your patience, guidance, and support over these years have been the cornerstone of my journey, and I will always be grateful for your mentorship. I am also incredibly thankful to my family—my mother, my father, and my sister—whose unwavering support and love have carried me through every challenge. Your encouragement has meant the world to me. A very special thanks goes to Carlotta, who has taught me to treasure every memory and always look at life from a fresh perspective. Finally, I want to thank all my colleagues for the wonderful moments we shared. The joy of working together has made this adventure all the more rewarding. Thank you all for being an essential part of this incredible experience.

Thank you.

TABLE OF CONTENTS

Acknowledgments iii

List of Acronyms viii

Chapter 1: Introduction 1

1.1 Bedload Estimation: Essential yet Challenging 1

1.1.1 Sediment Budgeting Approach 4

1.1.2 Virtual Velocity Approach 4

1.1.3 Morphological Change Detection and Survey Frequency 5

1.1.4 Path Length Computation and Tracer Employment 6

1.2 The Laboratory Scale 7

1.3 Aim of This Work 8

Chapter 2: Materials and Methods 9

2.1 Experimental setup: Pi flume 9

2.2 Theoretical Background: The Exner Equation 10

2.3 Bedload morphological imprint investigation 14

2.3.1 Experiments and run setup 14

2.4 DoD analysis 16

2.5 The PiQs framework 18

2.6 Tracers displacement investigation 18
2.7 Tracer Implementation and Initial Analysis 18
2.7.1 Experiments and run setup 19
2.7.2 Tracers extraction 20

Chapter 3: River active width 29
3.1 Research questions 29
3.2 Experimental design 29
3.2.1 Morphological changes 30
3.2.2 Bedload activity 31
3.3 Results 31
3.3.1 MAW and BAW variability analysis 31
3.3.2 Morphological Active Width - MAW 32
3.3.3 Bedload Active Width - BAW 33
3.3.4 BAW and MAW comparison 34
3.4 Discussion 35

Chapter 4: Non-morphological bedload 41
4.1 Experimental design 41
4.2 Research questions 41
4.2.1 What is the non-morphological bedload? 42
4.2.2 Non-morphological bedload components 42
4.3 Results 43
4.3.1 Non-morphological bedload components estimation 44

4.3.2 Non-morphological bedload intensity 48
4.4 Discussion 49

Chapter 5: Tracers displacement analysis 53
5.1 Research questions 53
5.2 Experimental design 53
5.2.1 Tracer position and topographic information 55
5.3 Results 55
5.3.1 Tracer position and DEMs-DoDs coupling 56
5.3.2 Tracers distribution 59
5.3.3 Distance between modes and fill area 61
5.3.4 The effect of discharge on tracer displacement 63
5.4 Discussion 64

Chapter 6: Bedload estimation 70
6.1 Introduction 70
6.2 Research questions 71
6.3 Methods 72
6.4 Results 73
6.5 Bedload estimation 74
6.6 Path length estimation 75
6.7 Discussion 75

Chapter 7: Conclusion 81

APPENDIX A: 84

A.1 DEM and DoD scheme 84

LIST OF ACRONYMS

BAA Bedlaod Active Area

BAW Bedload Active Width

DEM Digital Elevation Model

DoD DEM of Difference

envBAW Bedload active width computed from bedload activity map envelopes

envMAW Morphological active width computed from morphological changes map envelopes

MAA Morphological Active Area

MAW Morphological Active Width

Abstract

Gravel-bedded rivers are crucial to riverine ecosystems worldwide, offering vital ecosystem services and often experiencing significant human impacts. Water, sediment, and vegetation interaction are central to river morphodynamics. Understanding these interactions is essential for effective river management and restoration. Despite advancements in topographic survey technologies and flume experiments, key aspects of bedload transport and riverbed morphology remain unclear, especially regarding the time scales of morphological changes. The spatial patterns of morphological changes and sediment dynamics, including entrainment, transport, and rest stages, are also poorly understood due to the spatial-temporal variability of bedload transport and challenges in direct flood measurements and modelling. Indirect methods such as geophones, tracers, and sediment volume budgeting have addressed these gaps. Morphological methods, based on sediment mass conservation, estimate sediment transport by tracking changes in river morphology. However, these methods are time-intensive, and their accuracy remains uncertain. While useful for rivers with high spatial-temporal variability, further understanding of bedload dynamics is needed to validate these approaches. This thesis utilizes laboratory experiments to address these knowledge gaps to investigate sediment transport dynamics and morphological imprints in a controlled environment. This approach provides deeper insights into the relationship between bedload and its morphological imprint. We investigate how bedload active width and morphological active width differ across various types of gravel-bed morphology and how these active widths change over different temporal scales. It will also explore the underlying mechanisms responsible for the differences between bedload and its morphological imprint. In addition, we analyse the temporal and spatial trends of tracer distributions in response to changes in flow rate within a consistent morphology, aiming to separately assess the influence of flow rate and morphological factors. We explore

the influence of the main deposition areas on the path taken by sediments. We find that the difference between the morphological and bedload active width depends on the river confinement. Morphological active width envelope from high temporal resolution DoDs improve bedload active width estimates, in particular in low confined systems. Not all areas experiencing bedload transport undergo morphological changes, which is central to the distinction between bedload and morphological active widths. This difference is attributed to near-equilibrium transport and the compensation and filtering processes. Compensation processes were observed to increase with discharge with their effects amplified when survey frequency decreases. In a broader context, compensation affects not only the active width but also the volume of sediment transported. The research underscores the critical role of compensation in sediment dynamics, particularly as the time between topographic surveys increases. The intensity of bedload transport in these areas is also substantial. In contrast, the influence of filtering processes shows a slight reduction with increasing discharge and decreasing survey frequency, with bedload activity in these areas being considerably lower than in compensation zones. Tracer displacement exhibited a clear correlation with river confinement and bed morphology. Tracers are more likely to settle in depositional zones. The spacing between distribution modes and depositional areas offered further insights into tracer behaviour. In particular depositional zones act as attractors resulting in multi-modal distributions. This finding provides valuable insights into the frequency of river observations and has important implications for the application of methods such as the virtual velocity approach, where the volume of eroded sediment is directly proportional to the bedload flow rate. The findings of this research offer significant contributions to understanding the complex interplay between bedload transport, morphological changes, and river confinement.

Rio Blanco gravel-bed river - Coyhaique, Aysén region, Chile (2023)

CHAPTER 1
INTRODUCTION

Gravel-bed rivers are fundamental components of riverine ecosystems worldwide, providing essential ecosystem services while being significantly impacted by human activities. The increasing recognition of the ecological and geomorphological importance of these rivers has spurred growing scientific interest in both flood protection for communities and the preservation of their ecological integrity. At the core of river morphodynamics lies the interaction between water, sediment, and vegetation. A comprehensive understanding of these interactions is crucial for effective river management and restoration (Wohl et al., 2015).

In particular, elucidating the processes that govern the interactions between these key components and assessing the influence of anthropogenic activities on these mechanisms are of paramount importance for the sustainable management of river systems (Wohl et al., 2015). Despite substantial efforts by the scientific community, the complexities of water-sediment interactions remain only partially understood. In gravel-bedded rivers, sediment transport occurs primarily through rolling, sliding, and saltation along the riverbed. This mode of transport, known as bedload, takes place in close contact with the riverbed.

1.1 Bedload Estimation: Essential yet Challenging

Predicting sediment transport using theoretical and empirical relationships often results in considerable uncertainty, particularly in settings where the spatial variability of sediment transport is difficult to account for. In gravel-bedded rivers, sediment transport exhibits significant lateral heterogeneity and is frequently confined to a limited portion of the river width (Ashmore et al., 2011; Ferguson, 2003; Gomez, 1991).

The concept of river active width, defined as the riverbed area where sediment transport occurs, is recognized as a key parameter for predicting sediment dynamics and bedload flux (Ashmore, 1991; Ashmore and Church, 1998; Ashmore et al., 2011; Bertoldi, Ashmore, and Tubino, 2009; S. Peirce et al., 2018).

Despite the established importance of active width, its spatial extent and temporal variability remain difficult to quantify. This is primarily due to challenges associated with tracking bedload transport during flood events and the highly unpredictable nature of sediment transport. Even in rivers with wide and complex channel networks, bedload transport and morphological changes are often observed in only a single channel which makes bedload investigation more challenging.(Ashmore, 1991; Bertoldi, Zanoni, and Tubino, 2009).

Direct bedload measurements, while reliable, are extremely challenging due to the high-energy conditions under which sediment is mobilized (Williams et al., 2015). Moreover, in rivers characterized by high spatial variability, obtaining continuous and spatially distributed bedload measurements is nearly infeasible (Ashmore, 2013; Habersack and Laronne, 2001), often leading to significant inaccuracies (Wilcock, 2001).

Various direct measurement methods, such as pressure difference bedload samplers

(Helley and Winchell, 1971; Lucía et al., 2013; Piton and Recking, 2016) and bedload traps (Kondolf, 2016), provide accurate point measurements but are limited in their ability to capture the full spatial and temporal variability of sediment transport (Bunte and Abt, 2003; K. Bunte and Abt, 2005; Vericat et al., 2006).

Sediment traps and settling ponds offer an alternative means of estimating bedload flux with greater accuracy, yet they fail to represent spatial variability adequately and are impractical for use in wide rivers (Garcia et al., 1999; Habersack et al., 2001; Reid et al., 1980; Rickenmann et al., 2012; Vericat and Batalla, 2010).

Due to the above-mentioned difficulties related to direct bedload measurements, it is possible to resort to the so-called "indirect methods". These methods study the effects of bedload with the aim of providing estimates on transport. Among these, morphological methods study morphological changes in order to estimate the bedload flux. The most recent review on the morphological method is presented by Vericat et al., 2017.

The pioneering work of Exner (1925) provided a theoretical framework for linking sediment transport variability to changes in sediment volume within a control volume. This approach, along with subsequent refinements (Hubbell, 1964), is based on the study of sediment budget.

$$\frac{\partial q_s}{\partial x} + \frac{\partial q_s}{\partial y} + (1-p)\frac{\partial \eta}{\partial t} + \frac{\partial C}{\partial t} = 0 \tag{1}$$

where q_s is the bedload flux per unit width, p is sediment porosity, η is bed elevation, and C is mixture concentration. The variables x, y, and t represent the streamwise, cross-wise, and temporal coordinates, respectively. Assuming C remains constant over time, the equation simplifies to:

$$\frac{\partial q_s}{\partial x} + \frac{\partial q_s}{\partial y} + (1-p)\frac{\partial \eta}{\partial t} = 0 \tag{2}$$

This relationship led to the development of the so-called 'inverse method,' pioneered by Ashmore and Church, 1998. The method formalized the possibility of inferring sediment transport from observed morphological changes over time using the Exner equation.

With the advent of repeated topographic surveys for measuring sediment storage, the inverse method evolved into a more general approach, now referred to as the "morphological method" (Brewer and Passmore, 2002; Church, 2006).

By integrating the Exner equation, it can be rewritten as:

$$\frac{\Delta Q_s}{\Delta x} + (1-p)\frac{\Delta \eta}{\Delta t} = 0 \tag{3}$$

where Q_S is the bedload flux computed over a unit length of channel width. The formula leads to:

$$(1-p)\Delta V = (Q_{s,in} - Q_{s,out})\Delta t \tag{4}$$

where ΔV is the sediment volume variation computed for the area unit and is computed from the $\Delta\eta$. This equation represents the mathematical foundation of the morphological method. The practical application of this approach remains challenging due to the high uncertainty associated with $Q_{s,in}$, and $Q_{s,out}$ (Grams et al., 2013). Achieving a well-

constrained sediment budget, where all ΔV, $Q_{s,in}$, and $Q_{s,out}$ are reliably quantified, remains rare (Erwin et al., 2012; Vericat et al., 2017).

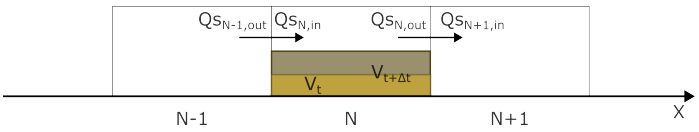

Figure 1 – The morphological method scheme as a succession of sediment reservois.

The morphological method can be schematised as a succession of sediment reservoirs (Figure 1). Each reservoir models a portion of the channel domain between two cross sections. The volume balance for the N-channel portion can be written as follows:

$$Q_{s,in} - Q_{s,out} = \frac{V_{t+\Delta t} - V_t}{\Delta t} \tag{5}$$

where $Q_{s,in}$ and $Q_{s,out}$ are the sediment discharge from upstream and to downstream, respectively, V_t and $Vt + \Delta t$ is the volume of sediment measured at time t and $t + \Delta t$. Equation 5 can be written as:

$$\Delta Q_s \times \Delta t = \Delta V \tag{6}$$

where Δt is the time between surveys (or the time during which sediment transport occurs), ΔV can be computed from repeated topographic surveys, and ΔQ_s is the difference between the sediment discharge in and out. Time and ΔV are known quantities, from which ΔQ_s can be obtained. If two Digital Elevation Models (Digital Elevation Model (DEM)s) are available and both are consistent with the same reference system and projection (Passalacqua et al., 2015), it is possible to compute their difference, yielding a map that illustrates the morphological changes between the two surveyed time points (Williams, 2012). From this map the volume of eroded or deposited sediment can be easily computed. Given that

$$\Delta Q_s = Q_{s,in} - Q_{s,out} \tag{7}$$

$Q_{s,in}$ and $Q_{s,out}$ remain unknown.

The underlying principle of the morphological method is based on sediment volume measurements obtained through repeated topographic surveys over time. By conducting topographic surveys at appropriate intervals, ideally following each flood event, it is possible to compute the ΔV term, which represents the volume variation within the surveyed reach. Given that the temporal interval between surveys (ΔT) is known, the net sediment transport difference, $Qs_{in} - Qs_{out}$, can be derived. This formulation is always valid as it follows the principle of mass balance, providing insights into sediment transport variations across space. However, it does not directly quantify sediment flux since $Q_{s,in}$ and $Q_{s,out}$ remain unknown. The morphological method described herein yields the spatial distribution of sediment transport variations. Two distinct approaches can be employed to derive the spatial distribution of sediment transport, as outlined in the following sections. Both approaches involve determining an unknown sediment flux, from which the distribution of bedload variation can be translated into bedload transport.

1.1.1 Sediment Budgeting Approach

The sediment budgeting approach can be applied at different timescales: from the event scale to the multi-event scales this method produces the spatial distribution of the bedload flux since the bedload flux is known in a certain section. The sediment budgeting approach determines the necessary boundary flux ($Q_{s,in}$ or $Q_{s,out}$) to initiate the numerical solution by employing two different strategies:

1. A zero-flux section can be incorporated within the reach, such as a gravel-sand transition (McLean and Church, 1999), an upstream lake or reservoir that does not release sediment, or an upstream dam (A. Brenna et al., 2020; Merz et al., 2006).

2. Alternatively, the reach can be subdivided into smaller sub-reaches. The known sediment flux can be specified at the boundary of one of these sub-reaches. If a net-depositional sub-reach transitions into a net-erosional sub-reach, a zero-flux boundary condition can be assumed, providing a lower-bound estimation of the sediment flux. If this condition is not applicable, sediment flux can be estimated through continuous bedload monitoring at a boundary (Grams et al., 2013). Alternatively, sediment flux can be derived using empirical (Erwin et al., 2012) or theoretical (Anderson and Pitlick, 2014) sediment transport models. In such cases, the length of each sub-reach should exceed the sediment step length to prevent sediment eroding from the upstream sub-reach from artificially passing through the downstream sub-reach.

As noted by Ashmore and Church, 1998, topographic calculations of scour and fill volumes likely include a non-negligible amount of fine sand and gravel, which may bypass the control volume via saltation or suspension. This introduces a potential bias in sediment flux estimation (Vericat et al., 2017).

1.1.2 Virtual Velocity Approach

The virtual velocity approach estimates sediment transport based on the mean velocity of bedload material. This method assesses the distance travelled by sediment during a flood event using tracers. Thus, this method should be applied at the event scale since the implementation of tracers provides better results once the tracer displacement is surveyed after a single flood to avoid sediment burial. For larger time scales, the approach loses its effectiveness as it becomes difficult to monitor the position of the tracers over a long period due to the distance travelled and the effects of burial. This approach relies on the ability to track the distance travelled of a representative sample of the entire sediment population present. It is therefore of paramount importance that the tracers placed and mobilised move on average as the entire population of sediments moved during the event studied. Furthermore, when evaluating mass flow, it is important to consider the time during which the sediment is actually put into motion, leaving aside the step-and-rest alternation but evaluating the motion from the entrainment phase to the stop phase. The virtual velocity approach is a valuable alternative to the sediment budgeting approach, in particular in large gravel-bed rivers (Brenna et al., 2019; Mao et al., 2017).

The virtual velocity is defined as:

$$v_b = \frac{P_L}{T} \tag{8}$$

where L is the path length and T is the time interval between surveys. This distance is divided by the duration of sediment entrainment or the total duration of the flood event. The velocity computed in this manner is referred to as *virtual* because it does not account for intermittent rest phases between transport steps.

By coupling the virtual velocity value with the volume of moving material, an estimate of sediment transport can be obtained. As proposed by Church, 2006; Haschenburger and Church, 1998, sediment transport can be estimated using the equation:

$$Qs = v_b d_s w_s (1 - p) \rho_s \tag{9}$$

where v_b is the virtual velocity, d_s is the erosion depth, w_s is the active width, p is porosity, and ρ_s is the sediment density. The scour depth can be obtained using scour chains (Laronne et al., 1994) and tracers (Hassan and Ergenzinger, 2005). When detailed topographic data is available, the equation can be modified to incorporate the total volume of eroded sediment (Vericat et al., 2017):

$$Qs = \frac{v_b \sum V_e (1 - p) \rho_s}{L_c} \tag{10}$$

where $\sum V_e$ is the eroded volume derived from repeated topographic surveys, and L_c is the channel domain streamwise length. In the two above formulations of the virtual velocity approach, the mass flow is given by the virtual velocity of the sediment and a volume of sediment that is considered to have passed through a given portion of the channel. This approach assumes that the volume of sediment eroded is representative of the volume of sediment transited and thus considers only the morphological component of transport, neglecting the non-morphological component (e.g. Piton and Recking, 2017).

1.1.3 Morphological Change Detection and Survey Frequency

As discussed earlier, advancements in survey technology now provide high precision and accuracy, allowing for a detailed representation of the riverbed with remarkable spatial resolution (Vericat et al., 2017).

However, sediment volume computation is affected by survey frequency due to local compensation effects (Lindsay and Ashmore, 2002). Compensation occurs when alternating scour and deposition processes take place at the same location between two survey periods. While the net difference between surveys can be computed, the intermediate morphological changes remain undetected.

Since topographic surveys cannot be conducted during floods, the event scale dictates the survey frequency of the topographic surveys and thus the morphological measurements that can directly influence bedload estimation. Although compensation effects have been investigated (Lindsay and Ashmore, 2002), the relationship between compensation dynamics, morphology, and discharge remains insufficiently understood.

Additionally, the noise introduced by morphological change detection in topographic

surveys could be significant. However, the impact of thresholding (removing all DoD values that in absolute value are less than a certain threshold) in DoDs compared to compensation effects has yet to be fully quantified. As Vericat et al., 2017 highlighted in response to J. Laronne, the influence of flow rate on filtered areas in morphological change computations requires further investigation.

1.1.4 Path Length Computation and Tracer Employment

When a known flow section cannot be incorporated into the analysis domain, the virtual velocity approach can be utilized. Both Equation 9 and Equation 10 require the path length to be known, which can be estimated through two primary methods: tracer studies or analysis of sediment transport about morphological unit distribution.

Comprehensive reviews on tracer studies can be found in the works of Hassan and Ergenzinger, 2005, Vázquez-Tarrío et al., 2019, and Liébault et al., 2024. In R. S. Pyrce and Ashmore, 2003, the authors investigated the relationship between particle path length and morphological changes in a gravel-bed river. Based on previously published data, they summarized key factors influencing path length, including morphology, channel width, sediment grain size, and discharge conditions. Their findings suggest that path length is strongly influenced by morphological scale, with the longitudinal distribution of tracers potentially exhibiting positive skewness or multimodality showing preferred stop positions (Church and Hassan, 1992a). Moreover, when a river features regularly spaced scour and deposition zones or well-defined morphological units, these factors significantly regulate path length. Morphology plays a key role not only in tracer displacement but in tracer entrainment as well, as pointed out by A. Brenna and Surian, 2023; Mao and Surian, 2010.

Tracers implementation presents several limitations, including low recovery rates Vázquez-Tarrío et al., 2019, burial McDowell and Hassan, 2020; Pierce and Hassan, 2020, and label decay Hassan and Bradley, 2017. To address these challenges, estimating path length based on the spacing between geomorphic units and determining the distance between sediment sources (scour areas) and sinks (fill areas) can provide valuable insights.

Neill, 1971 first explored this approach in meandering rivers, evaluating travel distance as half the wavelength of a meander. Subsequent investigations in gravel-bed rivers have been conducted by Ferguson and Ashworth, 1992 and Goff and Ashmore, 1994a, among others. A pioneering laboratory-scale study by Kasprak et al., 2015 confirmed the significance of river bars as zones of tracer accumulation in braiding networks.

Tracer displacement is also influenced by particle size, as conceptualized in Einstein's initial formulation and further developed by Vázquez-Tarrío et al., 2019. Field observations by Mao et al., 2020 confirm that particle size affects sediment mobility and resting time, the duration a tracer remains stationary before subsequent movement. These factors play a crucial role in shaping the overall dynamics of tracer transport.

R. S. Pyrce and Ashmore, 2003 emphasized the need for further investigation into the relationship between path length and morphological pattern distribution, particularly as the extent and magnitude of morphological changes evolve Ashmore and Church, 1998; Vericat et al., 2017.

1.2 The Laboratory Scale

Laboratory experiments are of considerable importance in the study of river morphology (Paola et al., 2009). In nature, the monitoring of certain variables can be quite complicated and often isolating the driving variables of the processes studied is quite impossible. Integrating empirical field data with controlled experimental studies enables the refinement of numerical models, enhancing both calibration and predictive accuracy. A more comprehensive understanding of sediment transport processes, combined with the increasing availability of large datasets, will facilitate the advancement of morphological methods (Pyrce and Ashmore, 2003) . In fact, although the morphological method has long been known, less well known are the space-time scales to be considered, which parameters to take into account and therefore the conditions under which it is most effective in assessing bottom transport. Ultimately, these improvements will enhance the reliability of numerical simulations and deepen our understanding of underlying geomorphological mechanisms Vericat et al., 2017. The laboratory scale provides significant advantages in the study of river morphodynamics. It allows direct observation and measurement of the processes underlying river morphodynamics, working in clear water and avoiding the dangers of studying the same phenomena during river floods. It also makes it possible to isolate the guiding variables that underlie morphodynamic processes and allows considerable control over them (e.g. slope, flow and grain-size). Finally, in the laboratory, it is possible to study phenomena that in nature have very long timescales by conducting experiments at reduced timescales, resulting in considerable energy savings. As we will see in the following chapters, the study of bedload transport and tracer displacement are two good examples of how the laboratory can allow us to investigate phenomena that would be impossible to study in the field. Since it is not the aim of this work to simulate a specific case but to focus on the processes at work, the experimental setup used was tested to ensure fully turbulent motion conditions (Re>2000 and Re*>70). These conditions have been verified in previous work carried out with the same experimental setup. Although the model can be seen as a simplification of reality, this is exactly what makes the use of this methodology worthwhile. In addition, the results obtained do not preclude the possibility of, where possible, proceeding to verification by means of experimental data or comparing the results obtained with theoretical results.

Laboratory-scale experiments provide a controlled environment to investigate the relationship between bedload transport and its morphological imprint. The ability to regulate key system variables allows for the isolation of specific processes Paola et al., 2009. Additionally, advances in image analysis techniques since Hergault et al., 2010; Papanicolaou et al., 1999; Radice et al., 2006 have significantly improved the capacity to track bedload movement through imagery analysis. Continuous, but very punctual, bedload measurements are described by Curran et al., 2015; Zaidan et al., 2024. Although very reliable, they often lack the spatial resolution necessary to capture bedload variability comprehensively.

Notably, the methodology developed by Redolfi et al., 2017, which leverages variations in image saturation as a proxy for bedload intensity, has demonstrated effectiveness in laboratory experiments for mapping bedload activity areas.

1.3 Aim of This Work

The objective of this thesis is based on the study of the indirect method as a useful tool for analysing the dynamics of solid transport in gravel-bed rivers. The morphological method is widely used to assess solid transport dynamics and produce bedload transport estimates. Although it has long been studied, the relationship between bedload transport and its consequences on morphology remains partly obscure. This work aims to shed more light on the potential and limitations of the morphological approach by studying the relationship between bedload and its morphological imprint, using observations at the laboratory scale, including the use of tracers.

Specifically, the study will focus on:

- Evaluating the impact of survey frequency on estimating morphological variations under different discharge conditions.
- Investigating the morphological imprint of bedload transport by analyzing variations in active width, and comparing the active area in terms of bedload with the active area in terms of morphology across different flow conditions.
- Identifying the conditions under which the morphological imprint is more or less pronounced and determining when bedload activity can be inferred from morphological changes.
- Examining tracer displacement under varying discharge conditions and using repeated topographic surveys to assess the influence of flow on tracer travel distances.
- Assessing the relationship between tracer distribution patterns and major morphological structures, determining when these structures can be used to define sediment path length.
- Evaluating the applicability of the morphological method using the virtual velocity approach, specifically analyzing the effects of survey frequency and the relationship between morphological changes and tracer displacement.

These analyses will enhance our understanding of sediment transport processes and identify key factors influencing tracer dynamics. Furthermore, they will contribute to the refinement of indirect sediment transport estimation methods, particularly the morphological approach, and provide valuable insights into the optimal conditions for their application.

CHAPTER 2
MATERIALS AND METHODS

This chapter provides a comprehensive description of the experimental setup and theoretical background employed to achieve the research objectives. It details the main characteristics of the instruments used, the parameters selected for the experiments, and the preliminary data elaboration process.

2.1 Experimental setup: Pi flume

The Pi flume (Figure 3 and Figure 4) is a laboratory channel at the Hydraulics Laboratory at the University of Trento, Italy. This artificial channel consists of a reinforced concrete base structure, 25 meters long and 2.9 meters wide. An aqueduct equipped with a pump (G) and flow meter (K), allows the recirculation of water from a trench (D) located downstream of the channel to a stilling basin (B) located upstream. The flow meter (k) has a logger time resolution of $0.01 l/s$. From the stilling basin (B), water can flow through the channel and back to the downstream trench (D). The flow rate can be controlled manually from the controls panel or automatically by custom-built software. The internal structure of the channel is filled with fine sediment (C), homogeneous, with a grain size of $1.03 mm$, a porosity of 0.37, and a submerged relative density of 1.63. The corresponding grain size distribution curve is presented in Figure Figure 2.

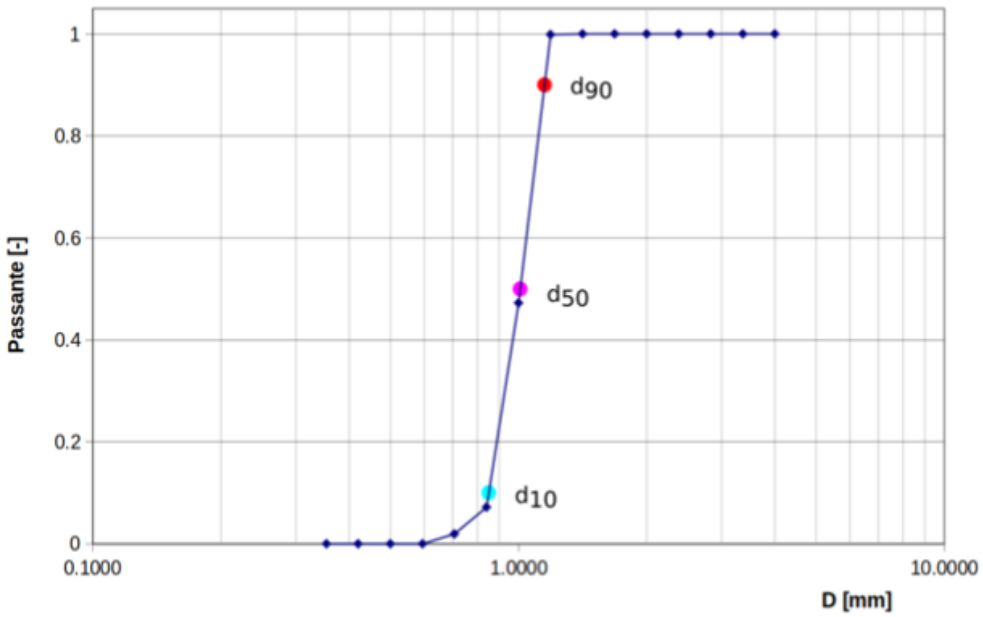

Figure 2 – Sediment grain-size curve.

The main components of the experimental setup are illustrated below with reference to Figure 4. For the present study, an internal 0.6-meter-wide channel was constructed. The rationale behind this specific geometry lies in the capabilities of a wide range of morphology (from braiding to wandering) involving a reasonable range of discharge as shown in Garcia Lugo et al., 2015. Upstream of the stilling basin, a dry sediment container (A) is positioned. A helical screw conveyor, with adjustable rotation speeds, facilitates sediment dosing. This sediment is introduced into the channel via a chute, with the inflow rate controlled manually or through custom-built software. At the downstream end, after crossing a threshold, water and sediment are collected in the downstream trench (J). The sediment is retained within a filtering crate (E) placed on load cells (F) with a logging time resolution of 1 minute and a precision of $0.01\ kg$, allowing continuous measurement of solid outflow rates. The channel slope is adjusted using a flattening blade (O), which flattens the channel bed based on the slope of the supporting tracks (N). For all experiments conducted in this study, the channel slope was set to $0.01\ m/m$. A topographic survey system is implemented using a laser (J) mounted on a movable bridge (I), which runs on longitudinal rails (H). This laser system provides an elevation accuracy of $0.1\ mm$ within an acquisition range of $[-10, +10]\ mm$. The survey area and spatial resolution of the collected points can be configured via custom-built software.

A Nikon D3100 SLR camera (M) equipped with a Nikkor 28 mm/f2.8D AF lens is mounted approximately 3 meters above the sand bed on a movable bridge (L) running along rails (H). The optical axis is oriented perpendicularly to the bed surface and aligned with the channel centerline. This setup enables systematic photographic surveys of the entire channel length, with each image covering an approximate area of $3 \times 2\ m^2$ and a resolution of $1\ mm^2$. Additionally, two stationary SLR cameras (P and Q) are positioned 3 meters above the bed to capture the last 6 meters of the channel, ensuring an image overlap of approximately $0.3\ m$.

Ground control markers are placed along the central channel to facilitate topographic referencing and image orthorectification. Uniform illumination during photographic surveys is ensured using LED strips positioned along both channel banks. The entire experimental setup is enclosed with opaque drapes to minimize external light interference.

A series of controlled experiments were conducted to simulate flood events under constant discharge conditions and to evaluate the impact of bedload transport on riverbed morphology. The experimental setup was designed to capture a range of morphological configurations, including braided networks, wandering single channels, and alternate bar formations.

2.2 Theoretical Background: The Exner Equation

To determine appropriate flood durations, we derived a time scale for riverbed evolution using the Exner equation. This equation, which expresses mass balance in a control volume, takes the following form:

$$\frac{\partial q_s}{\partial x} + \frac{\partial q_s}{\partial y} + (1-p)\frac{\partial \eta}{\partial t} + \frac{\partial C}{\partial t} = 0 \tag{11}$$

Where:

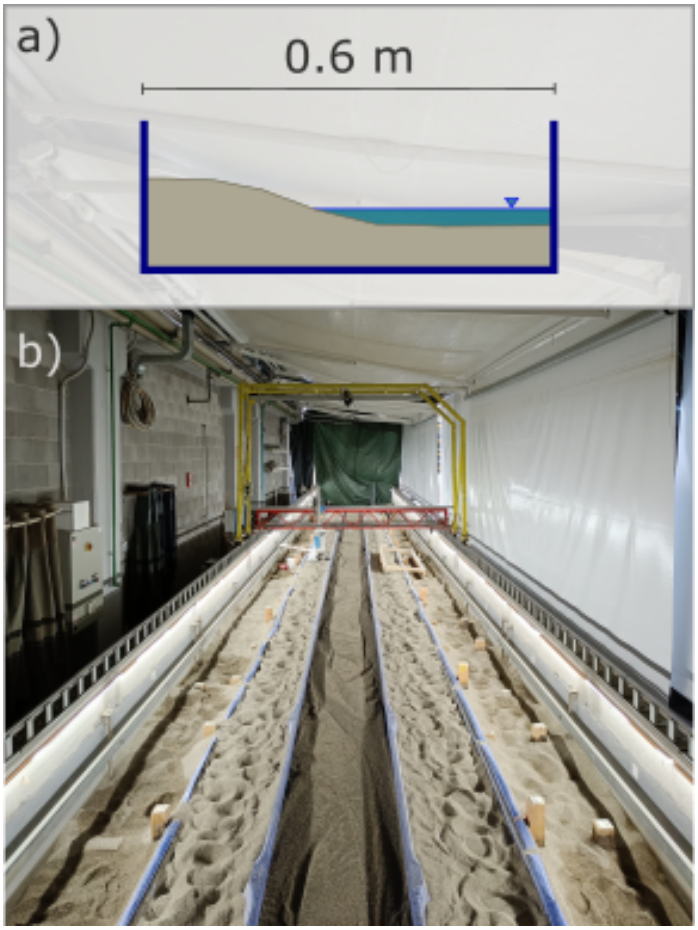

Figure 3 – a) The π flume cross section with water, sediment and artificial banks. b) Photo of the π flume taken from upstream to downstream. Are visible the movable bridge in yellow and the laser movable bridge in red. The inner channel banks are visible in blue.

- q_s is the bedload flux,
- p is sediment porosity,
- η is bed elevation,
- C is mixture concentration,
- x, y, t are the stream-wise, cross-wise coordinates, and time, respectively.

Assuming that C is constant over time, the equation simplifies to:

$$\frac{\partial q_s}{\partial x} + \frac{\partial q_s}{\partial y} + (1-p)\frac{\partial \eta}{\partial t} = 0 \tag{12}$$

To make the Exner equation dimensionless, we can scale the terms with specific length, time, velocity and sediment flux:

$$x^* = \frac{x}{L_0}, \quad U^* = \frac{U}{U_0}, \quad \eta^* = \frac{\eta}{D_0}, \quad q_s^* = \frac{q_s}{\sqrt{\Delta g D_s^3}\Phi(\theta_0)}, \quad t^* = \frac{t}{T_B} \tag{13}$$

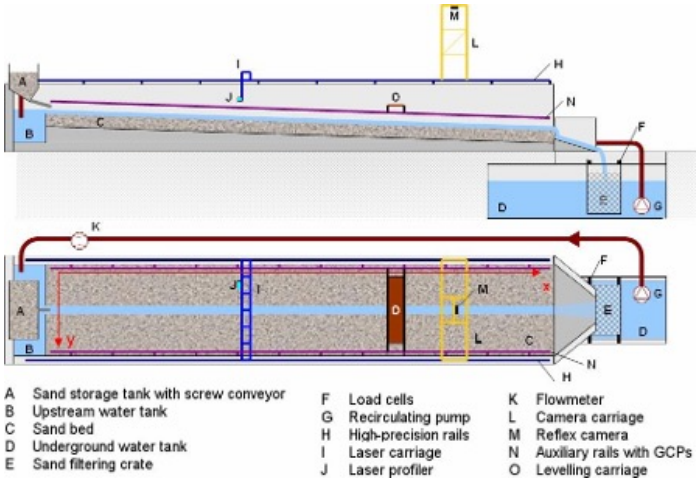

Figure 4 – The π flume scheme where the main components and the laser reference coordinate system are shown. Cross-section (top) and upper view (bottom).

Substituting these dimensionless quantities into the Exner equation, we obtain:

$$\frac{\partial q_s^*}{\partial x^*}\frac{\sqrt{\Delta g D_s^3}\Phi(\theta_0)}{L_0} + (1-p)\frac{\partial \eta^*}{\partial t^*}\frac{D_0}{T_B} = 0 \tag{14}$$

From this, the time scale for riverbed evolution T_B is derived as:

$$T_B = (1-p)\frac{L_0 D_0}{\sqrt{\Delta g D_s^3}\Phi(\theta_0)} \tag{15}$$

The specific flow of bedload q_s is related to solid discharge Q_s as follows:

$$q_s = \sqrt{\Delta g D_s^3}\Phi(\theta_0) \tag{16}$$

$$Q_s = W\sqrt{\Delta g D_s^3}\Phi(\theta_0) \tag{17}$$

Thus, the Exner time scale can be rewritten in terms of solid discharge:

$$T_B = (1-p)\frac{L_0 D_0}{Q_s/W} \tag{18}$$

This time scale represents the rate of morphological evolution and serves as a fundamental parameter in defining experimental durations.

This relationship varies directly with the characteristic length scales L_0, D_0, and W, and inversely with the solid discharge Q_s. Considering the scheme in Figure 5, it is possible to propose an interpretation of Exner's time scale.

Let us consider a channel section of length L_0, width W, and water depth D_0, assuming that both the water surface and riverbed are stationary. Furthermore, we assume that the downstream cross-section is impermeable to sediment transport. If the channel section is subjected to a solid discharge Q_s, the Exner time scale of riverbed evolution corresponds to the time required for the sediment to fill the current water volume.

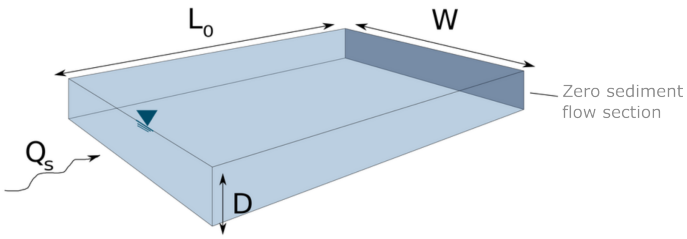

Figure 5 – Exner time-time scale interpretation scheme.

Thus, the Exner time scale provides a characteristic measure of the rate of riverbed evolution. This parameter can be used to characterize laboratory experiments and to define their duration so that the magnitude of bedload remains theoretically constant.

In Equation (Equation 18), the parameter p is a constant that characterizes sediment porosity. To study morphological variations that scale with the channel width W, the characteristic length L_0 is set equal to W. Special attention must be paid to both D_0 and Q_s.

The current depth D_0, in the absence of experimental data, can be approximated using a uniform flow equation. Using Chézy's formula, the flow discharge Q can be written as:

$$Q = \Omega C \sqrt{g R_H S} \tag{19}$$

where:

- Ω is the wetted cross-sectional area,
- C is the Chézy roughness coefficient,
- g is gravitational acceleration,
- R_H is the hydraulic radius, and
- S is the channel slope.

For the Chézy roughness coefficient C, we adopt the following formulation:

$$C = 2.5 \ln \left(\frac{11 D}{k D_s} \right) \tag{20}$$

where:

- D is the water depth,
- k is a calibrated parameter based on previous experiments under similar conditions, and
- D_s is the sediment grain size.

Given that:

$$\Phi = \frac{Q_s W \Delta g D_s^3}{L_0} \tag{21}$$

we can compute the dimensionless solid discharge Φ.

2.3 Bedload morphological imprint investigation

2.3.1 Experiments and run setup

To investigate the effects of bedload transport on riverbed topography, a series of consecutive flood simulations were conducted. Each simulation run was bracketed by topographic surveys to capture the morphological changes induced by the bedload. An example hydrogram for the 0.7 L/s flow rate is presented in **??**.

Approximately two minutes after starting the test, the flow rate reaches the set target. Through continuous feedback from the flow meter, the inverter acts on the number of revolutions of the pump. This produces some variability on the output flow rate figure, which, however, is mitigated at the outlet of the stilling basin.

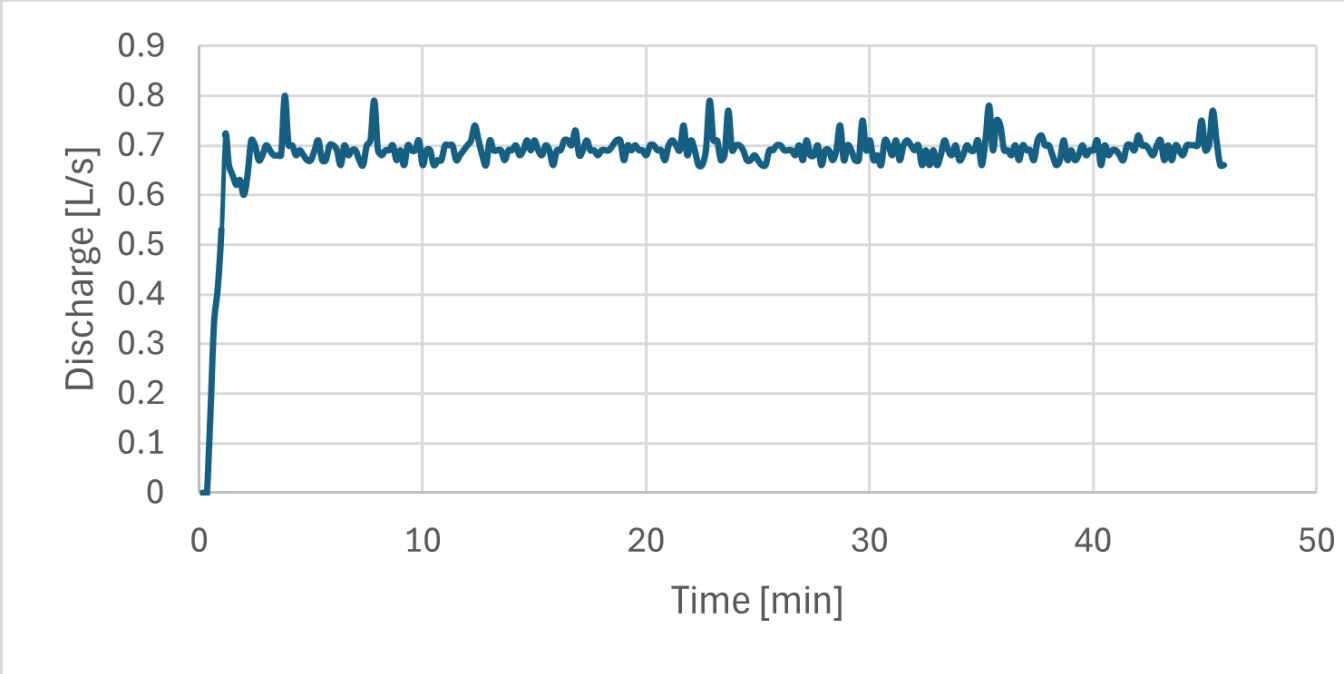

Figure 6 – Example of DEMs varying flowing discharge.

To isolate the effects of discharge variation, all simulations were performed under conditions of constant discharge. Additionally, the runs were carried out under near-equilibrium conditions to minimize the influence of long-term processes such as incision or aggradation. This objective was achieved by evaluating the sediment flux at both the inlet and outlet of the channel flume. In this way, the morphology studied is that generated by the constant flow that is made to flow. Thus, the flowing discharge can be considered as the formative discharge or, in other words, as the bankfull discharge or mean annual

flood. Furthermore, the duration of each run was set to half of an Exner time, leading to shorter runs for higher discharges. This approach ensured that the bed evolution rate, as computed in the previous section, remained theoretically constant. A preliminary estimate of the Exner time was derived from previous experiments conducted under similar conditions. Starting from a flat-bed morphology, a long-duration run with constant discharge was initiated. The run duration was set to 30 Exner times, allowing the constant discharge to adequately develop the bed morphology. During this run, solid discharge at the channel outlet was monitored to provide feedback to the screw conveyor, ensuring that the sediment input and output remained balanced. By continuously monitoring the solid discharge at the outlet and adjusting the inlet accordingly, equilibrium conditions were determined. Once equilibrium was achieved, the Exner time was updated to reflect the new solid discharge measurements.

The last 10 Exner times of the long-duration run were monitored using a fixed camera, providing a time-lapse of channel evolution. Additionally, bedload transport was continuously monitored at the outlet, yielding valuable information without interruptions.

After 30 Exner times of morphological development, an initial topographic survey was performed, followed by a run lasting 0.5 Exner times. A series of nine simulated floods, each lasting 0.5 Exner times, were conducted, with topographic surveys performed before and after each run. The selection of 0.5 Exner times for each test was driven by the constraints of the laboratory instrumentation, representing the maximum achievable time discretization. For a flow rate of 2.0 l/s, the Exner time is approximately 30 minutes, making 0.5 Exner times equivalent to 15 minutes. This time frame represents the lower limit and was chosen to minimize the impact of pump startup effects, ensuring that the water flow reached the desired regime along the entire length of the channel.

During the flood phase, fixed SLR cameras positioned above the final section of the channel continuously captured images, enabling the creation of time-lapse sequences that documented channel evolution. The images obtained through this method provided valuable qualitative data, offering insights into channel dynamics, including the number of channels and their evolution over time.

Topographic surveys

The spatial discretization for measuring riverbed elevations was determined by a balance between morphological and practical considerations. On the one hand, it was necessary to identify the bedforms of interest, specifically those with characteristic dimensions and spatial scales relevant to the phenomenon under study. On the other hand, the discretization had to allow for agile surveying and manageable data processing. Thus, a compromise was sought between a spatial resolution that effectively captured the morphological changes and a data size that remained computationally feasible. Bedforms such as gravel bars, which scale with the channel width W in planform and with the water depth D in profile, were of particular interest.

It is well known that bedforms like gravel bars exhibit anisotropic spatial variability. This morphological structure dimension scales crosswise with the water depth and streamwise with the channel width. Given the constant speed of the laser survey along the trans-

verse axis (approximately 40 seconds to traverse the entire channel width), the longitudinal advance depended heavily on the chosen spatial discretization. Consequently, the laser surveys were conducted with a spatial resolution of 5 mm along the transverse axis (1/120th of the channel width W) and 50 mm along the longitudinal axis (1/12th of the channel width W). To account for the slope of the channel and the limited acquisition range, and to avoid complex vertical adjustments of the laser, the decision was made to conduct the surveys using the full extent of the available laser measurement range. Moreover, the surveyed area was positioned at a distance from the initial conditions to minimize their influence, while being close to the downstream section, which is nearest to the outflow sediment measurement system. As a result, a survey length of 14 meters, corresponding to 23 channel widths, was achieved.

This setup produced a total of 280 cross-sections, each comprising 144 data points, and the entire survey took approximately five hours to complete. After the long preparation run and after each run, a topographical survey is carried out. This consists of DEM (Digital Elevation Model) in ASCII grid format. For each discharge, a total of 9 floods and 10 topographic surveys are reproduced. General information about water discharge, sediment flow, run duration, and the ratio between wet width and total width is reported in Table 1.

Table 1 – Main run parameters and measured variables for each discharge value.

Discharge [L/s]	Sediment flow [g/s]	Run duration [minute]	Exner time [minute]	Wet/Total Width [-]	Stream power [-]	Planform style
0.5	0.25	81	109	0.85	0.07	Braiding
0.7	0.33	47	74	0.82	0.11	Braiding
1.0	0.78	25	48	0.88	0.14	Braiding
1.5	2.39	20	30	0.92	0.20	Wandering
2.0	3.34	15	20	0.95	0.25	Wandering

2.4 DoD analysis

The digital Elevation Models (DEMs), generated by laser surveys and processed through the flume management software, undergo initial processing to achieve a more manageable file structure for further analysis. These surveys are converted via a script into files with an ASCII grid structure, forming a matrix in which each cell corresponds to a spatial discretization element. Additionally, the script produces a detrended DEM, from which the initial bed slope (0.01 m/m) is subtracted. This detrended DEM is particularly useful as it enhances the visibility of the river bed morphology.

From these DEMs, DEMs of Difference (DEM of Difference (DoD)s) can be derived through straightforward subtraction. Since DEMs are represented as matrices, their point-by-point components can be subtracted using the formula:

$$DoD_{2-1}[i,j] = DEM_2[i,j] - DEM_1[i,j] \tag{22}$$

where i and j represent the rows and columns of the matrix and 1 and 2 represent consecutive epochs. This process yields a matrix of differences between two consecutive

surveys, DEM1 and DEM2. In this difference matrix, values less than zero indicate excavation, while values greater than zero represent deposition.

However, as shown in Figure 8, the simple subtraction of DEMs introduces significant background "noise", primarily attributable to surface roughness. To address this issue, a filtering process was applied to the data. The first step involved applying a moving average along the cross-section. This was done by imposing a moving average of size $(3, 1)$ across the entire section, weighted according to the kernel:

$$\text{ker} = \begin{bmatrix} 1 \\ 2 \\ 1 \end{bmatrix} \tag{23}$$

In addition, a filter was applied to the DoD data. Given that the laser's accuracy in measuring elevations exceeds the grain size, small changes, such as the movement of a single particle, could be misinterpreted as excavation or deposition. Therefore, data filtering aims to distinguish between areas in the DoD that reflect actual excavation or deposition and those that are merely background noise or local scour and fill phenomenon. The study is focused on analyzing larger bed forms that scale with channel width rather than depth (such as ripples, dunes, and antidunes).

The filtering process is divided into two main steps. The first step, known as threshold analysis, eliminates background noise by setting all DoD values below a threshold (Th1) to zero. By applying a threshold of 2.0 mm, background roughness is effectively removed. A second threshold (Th2) is then introduced to define areas of significant excavation and deposition. All scour or fill that, in absolute value, exceeds the Th2 threshold set at 15 mm remain as such. For DoD absolute values between Th1 and Th2, a secondary filtering process is applied.

This secondary step, known as neighbourhood analysis, follows the steps below:

1. Isolated scour of fill clusters are eliminated if the number of cells that belong to each cluster is less than 6.

2. Isolated area where the DoD values are zero but are surrounded by non-zero values are filled with the neighbourhood mean if the cluster number of cells is greater than 6.

3. The nature (scour, no-change, or fill) of the DoD cells is analyzed: for each DoD cell, the 8 surrounded cells nature is evaluated and the number of scour, fill, or zero cells is computed. The nature of the core cell is confirmed once at least 5 cells with the same nature are found in the neighbourhood. Otherwise, the cell value is set to zero.

4. Step 1. and 2. are repeated to despeckle the DoD domain.

An example of the effects of the filtering process is reported in Figure 9, where the main scour (red) and fill (blue) areas are highlighted. Background noise and small areas are filtered out. The filtering process does not produce appreciable alterations in the total volume of sediment computed from the DoD.

In Figure 10 an example of DoDs taken at the maximum temporal discretization is presented for each discharge.

2.5 The PiQs framework

As previously discussed, during the flood phase, two cameras positioned approximately 3 meters above the channel capture one photograph per minute. The two SLR cameras are arranged to produce slightly overlapping images, covering a total investigation length of about six meters. Ground Control Points (GCPs) are placed on top of the inner canal banks, with their coordinates known in relation to the canal's reference system.

Taking advantage on the algorithm developed by Redolfi et al., 2017, the time-lapse was used to obtain maps of bedload activity. The images are rectified using a MATLAB script that takes into account the lens characteristics and the GCPs coordinates. This process establishes a direct correspondence between each pixel in the image and a coordinate in the channel's reference system. RGB images are converted to the HSV (Hue, Saturation, Value) colour space. The difference between two consecutive images can then be calculated in terms of the saturation (S) component. As demonstrated by Redolfi et al., 2017, the saturation component provides greater signal homogeneity and is less impacted by shadow noise from the banks. By using the change in saturation (ΔS) as a proxy for sediment transport activity, it is possible to obtain maps of bedload activity. A threshold on the saturation value [0,255] is applied to these maps to calibrate the model, ensuring that saturation differences above the threshold correspond to actual transport activity. This threshold is determined through a manual calibration process where a set of images for each discharge is analyzed to find the best-fitting threshold.

Figure 11 illustrates an example of a saturation difference map between two successive images taken during a constant flow rate of 1.0 L/s. From these comparisons, it is possible to quantify which portions of the riverbed are affected by transport.

In Figure 12 areas where bedload is detected are presented for different discharges. Colours show the magnitude of difference in saturation that is used as a proxy of bedload as reported in Redolfi et al., 2017.

2.6 Tracers displacement investigation

2.7 Tracer Implementation and Initial Analysis

The objective of these experiments is to trace the position of the tracers placed in the channel using photographic surveys. We want to investigate the influence of morphology on tracer displacement and, at a fixed morphology, the effect of different flow rates. For this reason, the experiments will be conducted on a morphology generated by a constant formative flow rate of 1.0 L/s. On this morphology, a set of 12 tests will be performed during which a constant flow rate will interact with the tracers. To evaluate the effect of different flow rates, three sets of 12 runs each will be performed at three different constant flow rates: 1.0 L/s,0.7 L/s, and 0.5 L/s. For more details on the experimental design, please refer to section 5.2.

Discharge Q $[l/s]$	Bedlaod $Q_s[l/s]$
0.5	0.18 ± 0.12
0.7	0.33 ± 0.18
1.0	0.78 ± 0.30

Table 2 – Discharge and solid discharge for the three runs.

2.7.1 Experiments and run setup

To study the effects of water discharge and bed morphology in tracer displacement we carried out a series of experiments involving the same channel described at the beginning of this chapter, and fluorescent and paramagnetic tracers. To avoid the effects of different transported materials, we used as tracers the same sand present in the laboratory flume. A specific coating is applied to make them fluorescent and paramagnetic (poleykettDevelopmentDualSignature, blackEverythingGoesSomewhere2013, hardyHighPrecisionTracing2019) without changing their density and size. Tracers can be detected using UV light and can be harvested using a magnet.

The experiments involved placing a crosswise stripe of tracers where bedload is expected as shown in Figure 13. Tracers are placed in semi-dry condition, this means that the channel is wet but no water is flowing. This prevents some tracers from being washed away by the current during the hydration phase of the channel.

The position of the tracers is monitored by photographic surveys in an area of 3×2 meters. In order to be able to monitor the maximum area available from the photographic survey, a wooden frame was therefore constructed to fit the banks of the inner channel. UV-led stripes were placed on this 2.2-meter-long frame to uniformly illuminate the portion of the channel affected by the analysis. Following some trials on the movement of tracers at the maximum flow rate, it was decided to carry out tests lasting 15 minutes for all flow rates. In fact, for the highest flow rate, after 15 minutes it was observed that either many tracers moved downstream leaving the analysis domain or remained fixed in the positions reached. All runs therefore lasted 15 minutes.

Given the limited duration of the tests, accurately measuring the solid flow rate is challenging, especially considering the time required for morphological evolution, which was approximately 70 minutes for the 1 l/s flow rate. Due to the inherent uncertainty of the flow meter (± 0.025 l/s) and the load cells (± 0.01 kg), it was not possible to obtain a precise measurement of the bedload flow rate. In the absence of precise measurements for the incoming solid flow rate, data from previous tests conducted in the same laboratory, using an identical experimental setup, were referenced. The tests were designed to achieve equilibrium and bedload discharge value from previous experiments is used to obtain this condition at the reach scale without artificially overfeeding or underfeeding the channel. Thus, the inlet sediment management system was calibrated to ensure mass balance, based on the bedload flow rate data. By averaging the results of the steady-state tests and conducting an analysis of the screw conveyor calibration, the sediment discharge values were obtained and are reported in Table 2:

2.7.2 Tracers extraction

Starting from the RGB images, we need to extract the tracer, define their position on the photo coordinate system and then convert this coordinate in the laboratory flume coordinate system. An example of RGB image is shown in Figure 14.

The algorithm of tracer extraction is schematize below.

Preliminary operation

The first operation involves correcting barrel distortion, which causes vertical and horizontal lines to curve outward from the centre of the image. Although this distortion is minimal with the lens used, it is corrected using the 'lensfunpy2' library. Next, the photos are cropped to exclude areas outside the monitored region, reducing computational time and saving memory.

Tracers detection

The extraction of tracers takes place through operations on the RGB band. Each band is extracted and, after numerous attempts, the fluorescent band was extracted successfully applying the following formula:

$$F = ((G - R) > -10)(350 < V < 700)(G > 100)(R < 190) \tag{24}$$

where F is the fluorescent band and R, G, B are the red, green, and blue bands respectively. V is the value and it is the sum of the red, green, and blue bands. This creates a binary map (Figure 15) in which for each pixel 1 indicates the presence of fluorescence and 0 indicates its absence. This image was subjected to light filtering to fill in individual non-fluorescent pixels surrounded by fluorescent pixels and to remove individual fluorescent pixels surrounded by non-fluorescent areas.

Fluorescent area polygonization

To obtain geometric information on the fluorescent area, such as the position of the centroid in the photo reference system, the surface area of the individual fluorescent areas, and their perimeter, the binary map was vectorised using the GDAL library available in Python. This allows us to convert the fluorescent areas in the binary map into polygons. For each polygon, it was possible to derive the position, area, and area-over-perimeter ratio (Figure 16).

Polygons with area-to-perimeter ratios lower than 2 are eliminated to avoid elongated polygons caused by water surface reflections.

Number of tracer estimation

In the initial phase of the run, the tracers hit by the current begin to move downstream from the feeding point. At this stage, the tracers are positioned very close together and the fluorescent halo detected by the algorithm may include more than a single tracer. In order to associate each fluorescent polygon with the number of tracers belonging to it, a

threshold was manually identified to discern whether there was a single tracer or more than one. 100 examples of single tracers and 100 examples of multiple tracers belonging to a single polygon were extracted from different runs. Analysing the area of the polygons and the photos where single tracers are easier to recognize, it was observed that generally single tracers generate a fluorescent halo ranging from $6mm^2$ to $40mm^2$. Polygons comprising two tracers, on the other hand, always have an area exceeding $70mm^2$. Thus, polygons with an area of less than $6mm^2$ are eliminated. The areas of polygons from 4 to $36mm^2$ were associated with the presence of a single tracer, while for areas above $35mm^2$, the number of tracers was estimated by approximating the total area of the polygon in mm^2 divided by $36mm^2$ to the nearest integer. In this way, it was possible to estimate the number of tracers in each polygon. This manually calibrated threshold is only necessary in the early stages when the moving tracers are very close together. In the intermediate and final phases of the run, the tracers are generally spaced a little apart and the algorithm detects individual tracings with very good results.

Centroids extraction

For each polygon, the centroid and its planar coordinates in the photographic reference system were calculated. The planar coordinates were entered into a matrix, as many times as the number of estimated tracers within the polygon. The coordinates were then translated into the laboratory flume reference system (the laser reference system) to enable dialogue with the topographic surveys. Since only moving tracers are of interest, the initial deposition area is excluded using a mask from the initial photo, buffered by 6 pixels (approximately a little bit more than double the diameter of one tracer). Since only tracers that have moved relative to the feeding point are of interest, the fluorescent halo detected in the first image of the time-lapse was used as a mask for all subsequent images. In Figure 16 in fact, tracers that belong to the feeding point are not detected by the polygonization algorithm.

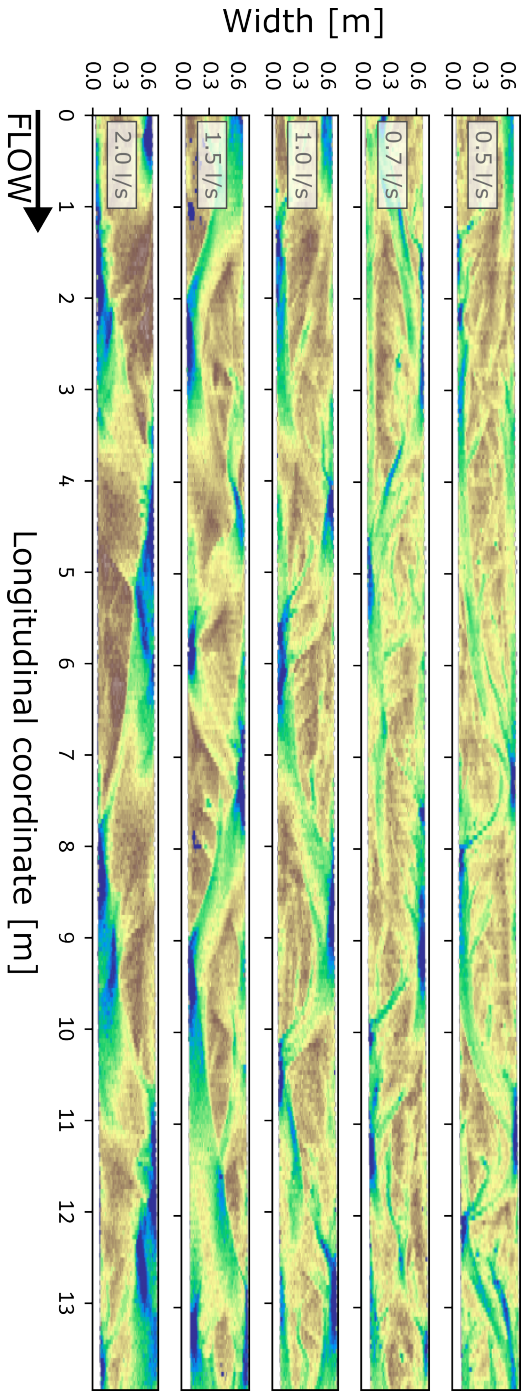

Figure 7 – Example of DEMs varying flowing discharge.

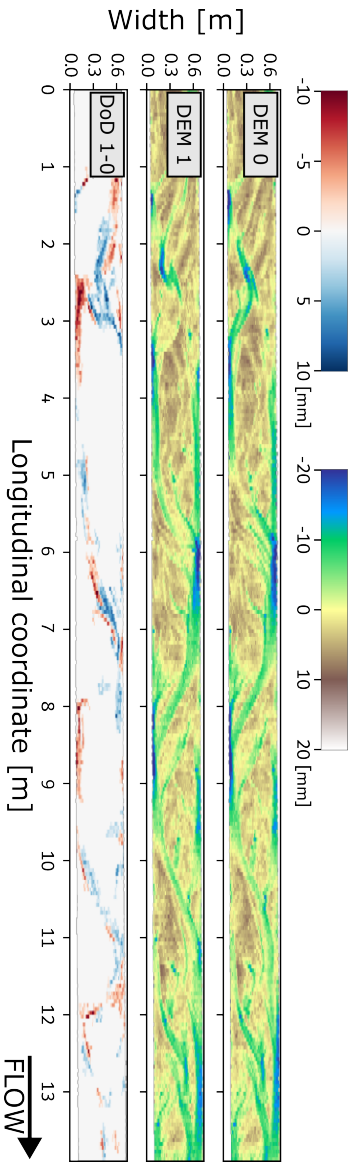

Figure 8 – Example DoD computed as the difference between two DEMs.

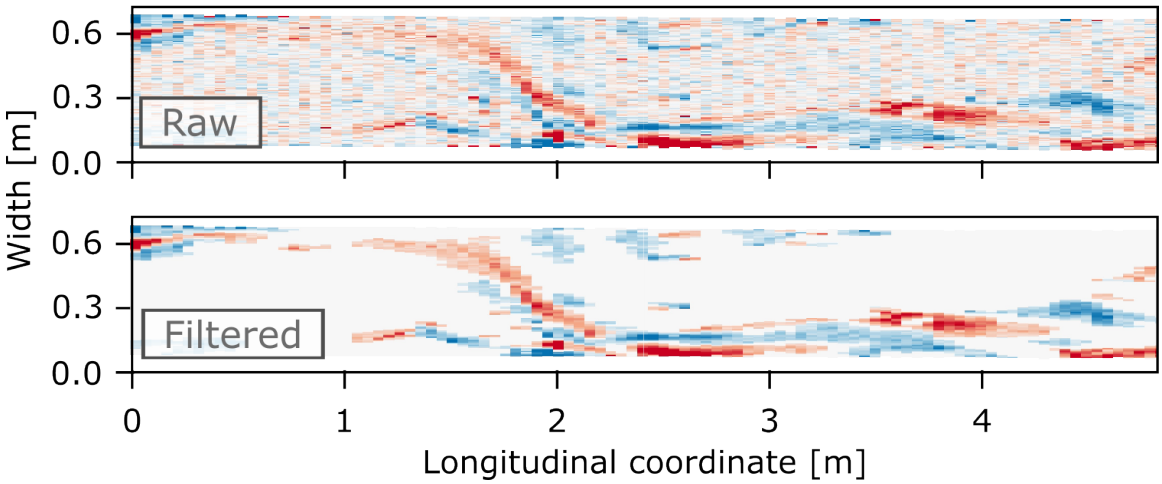

Figure 9 – Example of DoD filtering process. The filtering process aims to highlight bedforms that scale with the channel width and remove small areas and background noise

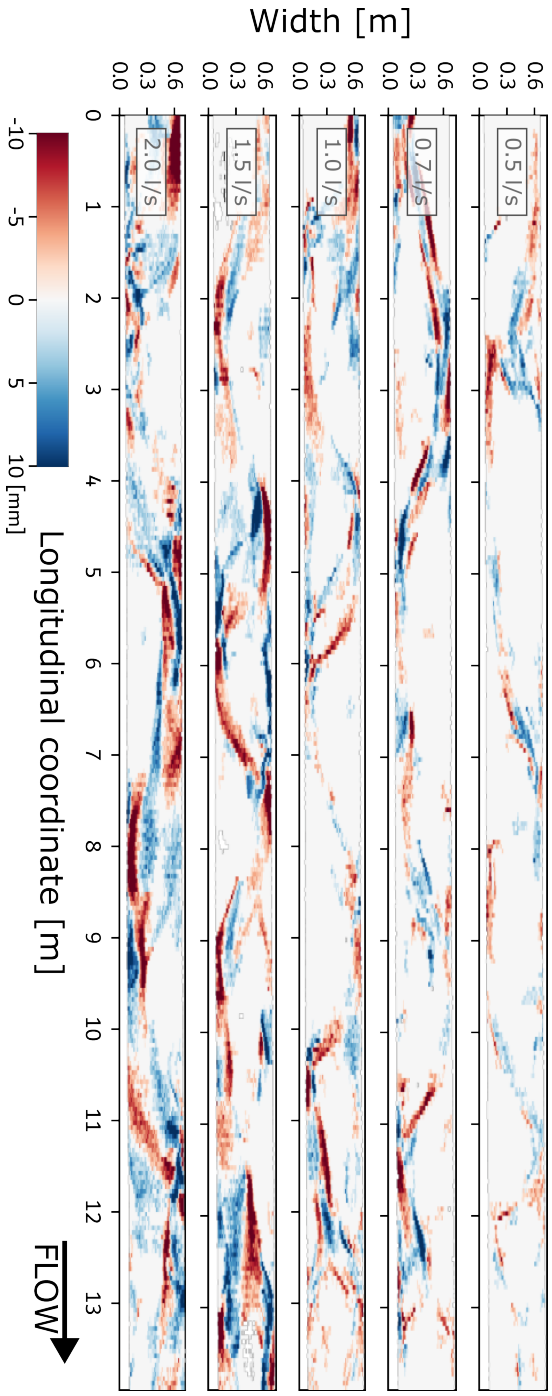

Figure 10 – Example of DoDs varying flowing discharge.

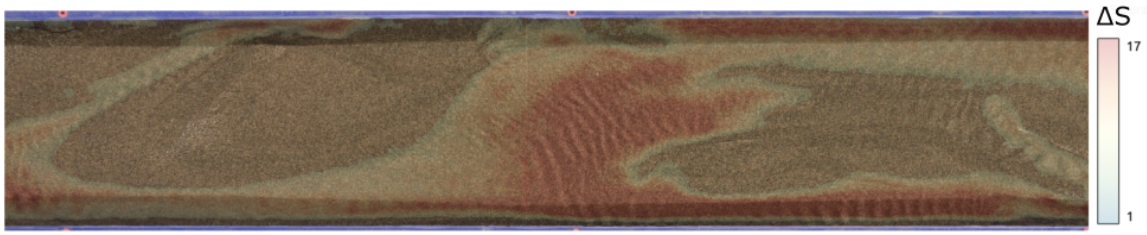

Figure 11 – Example of difference in saturation between consecutive maps. This information is used as a proxy for bedload intensity.

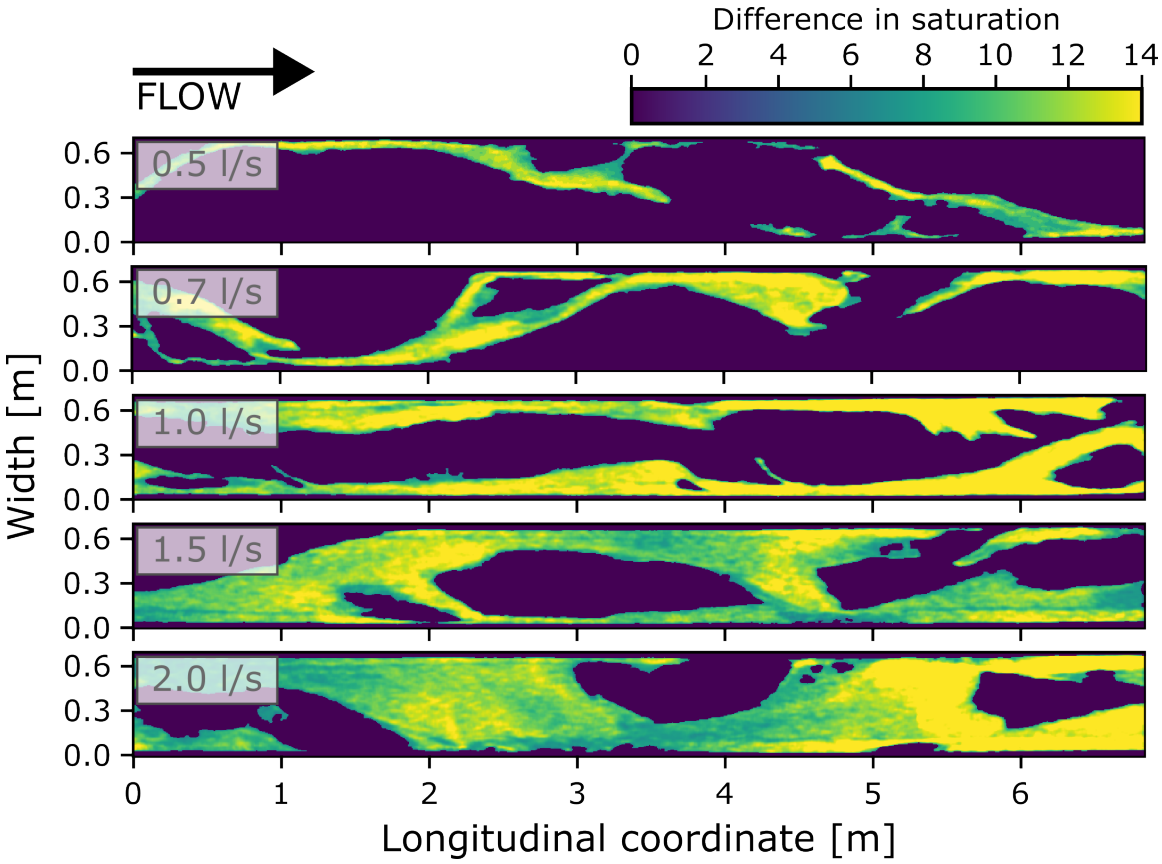

Figure 12 – Example of bedload intensity map for each of the available discharges. Bedload intensity is expressed as difference in saturation.

Figure 13 – Tracers are manually placed in the flume channel.

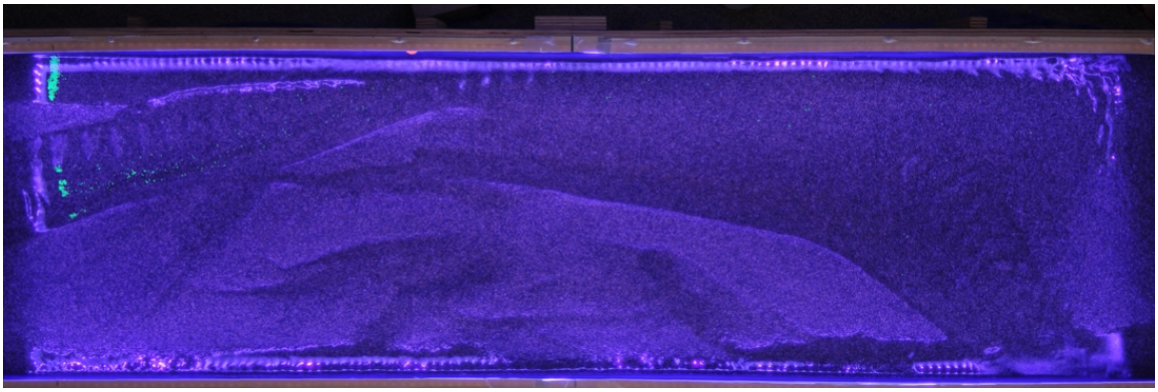

Figure 14 – Example of RGB photo survey. Tracers are fluorescent and located on the top-left part. Flow from left to right.

Figure 15 – An example of fluorescent band extraction. Traces are detected where the matrix value is 1 (white) and are not detected where the matrix value is 0 (black). Flow from left to right.

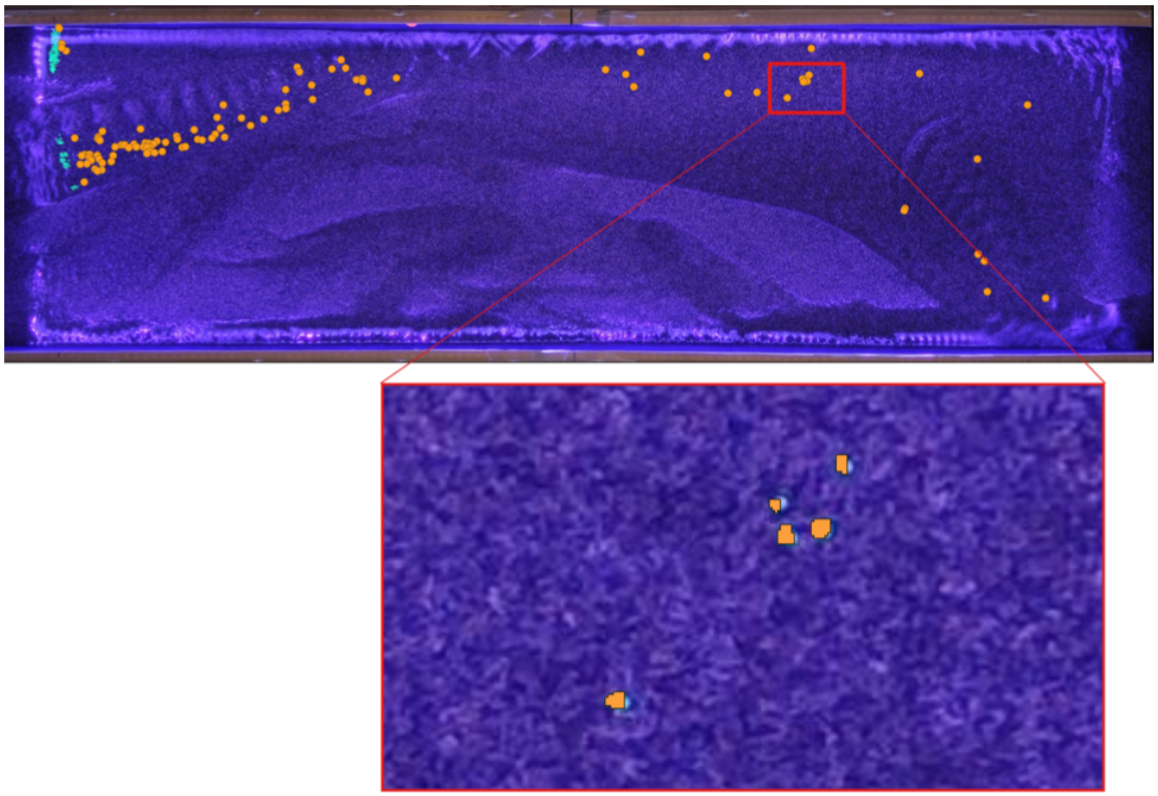

Figure 16 – An example of band extraction, vectorization, and centroids extraction. Each centroid is associated with a planimetric coordinate.

CHAPTER 3
RIVER ACTIVE WIDTH

The active width of rivers is a parameter widely employed to evaluate morphological dynamics in gravel-bed rivers. As discussed in chapter 1, multiple approaches exist to quantify the active width of a river. In this chapter, we focus on two specific metrics: the morphological active width, defined as the proportion of the channel exhibiting morphological changes due to bedload activity, and the bedload active width, which represents the proportion of the channel experiencing bedload transport.

Details regarding the experimental setup and the data obtained are provided in chapter 2. The morphological active width is analyzed by varying discharge rates and the frequency of topographic surveys used for its calculation, whereas the bedload active width is investigated primarily as a function of discharge. The values of morphological and bedload active widths are then related to various channel morphologies. Subsequently, the two metrics are compared to identify their differences and the conditions under which a stronger link exists between bedload activity and its associated morphological imprint.

3.1 Research questions

This chapter aims to address the following research questions:

- **RQ1**. What is the effect of survey frequency on the estimation of morphological active width? How does discharge influence this estimation?
- **RQ2**. What proportion of the channel experiences bedload transport, and how does this proportion vary with changes in discharge and survey timespan?
- **RQ3**. What is the relationship between the channel areas experiencing bedload transport and those exhibiting measurable morphological changes? How does this relationship evolve with increasing discharge and survey timespan? Additionally, under what circumstances can morphological changes provide insights into the portions of the channel subjected to bedload transport?

3.2 Experimental design

Morphological changes and bedload activity were investigated in the flume described in chapter 2, through a series of five experimental runs, each conducted under a distinct constant water discharge condition (see Table 1 for the main parameters of each run).

Each experimental run comprised three distinct phases:

- **Phase 1**: A constant prescribed discharge was maintained to allow the channel to achieve equilibrium morphology. This phase lasted for 20 Exner times.

- **Phase 2**: to reduce the influence on bedload activity due to the start-up and shout-down flood phase, bedload activity was continuously monitored using the time-lapse (see section 2.5) for 10 Exner times.
- **Phase 3**: Nine flood events, each lasting 0.5 Exner times, were simulated with a constant discharge for each flood. Bed topography was surveyed before each flood event and at the end of the run using a laser scanner (see subsubsection 2.3.1). Bedload activity was also continuously monitored during this phase. In total, 10 topographic surveys were conducted for each experimental run.

A schematic representation of the experimental design is provided in Figure 17.

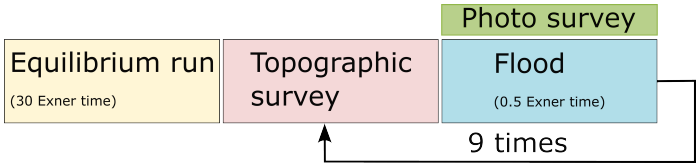

Figure 17 – Experimental methodology scheme where the three phases are presented.

Given the considerable duration of the first phase, which was sufficient to develop a stable morphology at a constant flow rate, bedload monitoring during phase 2 provided a reliable bedload active area value without interruptions. Additionally, bedload activity was monitored during each flood repetition, allowing for a direct comparison between bedload transport and its morphological imprint using DoDs.

3.2.1 Morphological changes

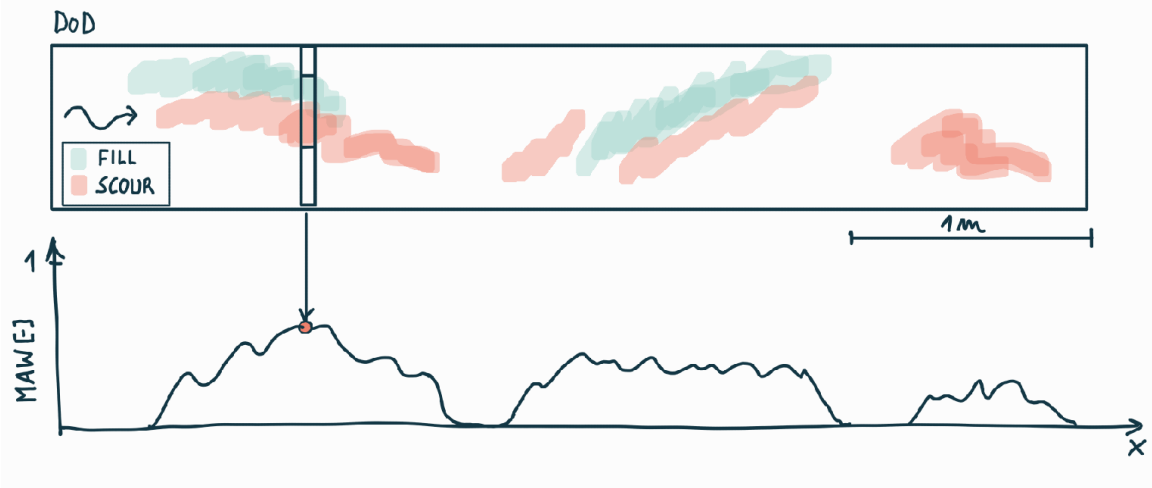

Figure 18 – Scheme for calculating morphological active width (Morphological Active Width (MAW)). A local active width can be calculated for each section as the ratio of the width exhibiting morphological changes to the total channel width. The MAW represents the average over the entire domain of local active width values.

The morphological active area (Morphological Active Area (MAA)) is defined as the portion of the channel where morphological changes occur, encompassing both scours and fills. By normalizing the MAA through division by the total channel area, the Morphological Active Width (MAW) is obtained, representing the average proportion of the channel width affected by morphological changes. A local MAW can also be computed by restricting the analysis to individual cross-sections; however, local values often exhibit substantial variability along the channel. To derive a representative parameter for the entire channel reach, the MAW should be calculated over a spatial domain of sufficient length to ensure stability and minimize variability (see below for more details). Furthermore, the evaluation of MAW depends on the timespan between consecutive surveys, as the observed MAA reflects the cumulative changes occurring over that period.

3.2.2 Bedload activity

Bedload intensity maps are used to identify regions of the channel domain that experienced bedload transport. These maps capture what can be interpreted as instantaneous bedload activity, especially when compared with the temporally discretized observations of morphological activity. Bedload activity is detected during each experimental run to pinpoint areas where bedload transport occurs. For each intensity map, similar to the computation of MAW, the bedload active width (Bedload Active Width (BAW)) is calculated as the average proportion of the channel width affected by bedload transport.

To facilitate a comparison between the Morphological Active Width (MAW) calculated as the difference in bed topography before and after a flood event and the Bedload Active Width (BAW), which is determined on a minute-by-minute basis, additional steps are required.

The instantaneous BAW can be adapted to a temporal scale comparable to that of the MAW by constructing an envelope of each instantaneous Bedload Active Area (Bedlaod Active Area (BAA)) map. This process involves summing all activity maps recorded throughout the flood event to create a composite map that identifies areas of the channel active at least once during the flood. To reduce the impact of transient flashes in bedload detection, only pixels that were active at least twice during the run duration are classified as active. Using this envelope map, the BAW is calculated following the previously described methodology, yielding a value that represents the proportion of bedload active width for the entire flood event.

3.3 Results

3.3.1 MAW and BAW variability analysis

Both the morphological active width (MAW) and the bedload active width (BAW) are calculated as averages over the entire domain of analysis to mitigate the variability observed when considering a single cross-section. To this end, the relationship between the variability in the calculation of these metrics and the length of the domain over which they are computed was investigated.

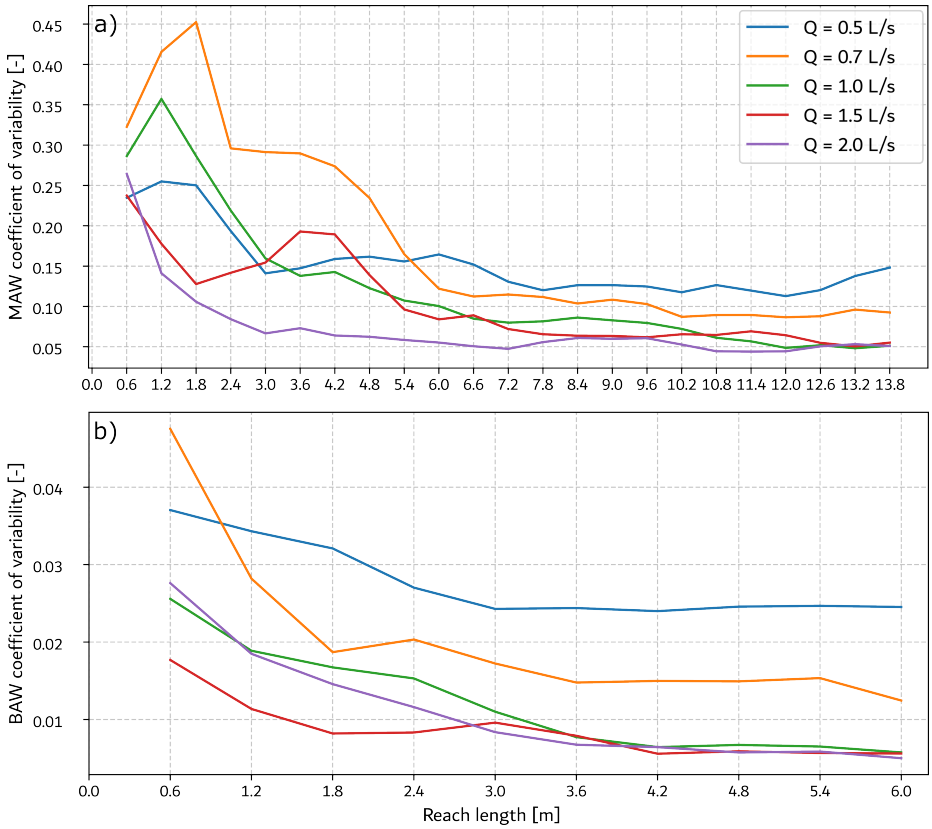

Figure 19 – MAW (a) and BAW (b) coefficient of variability varying the channel domain length up to the maximum surveyed with the two different techniques.

Figure 19a illustrates the coefficient of variability for MAW as a function of channel length, expressed as multiples of the total channel width. The results show a monotonically decreasing trend for all the flow rates. The results indicate that after approximately 12 channel widths, the variability coefficient decreases from an initial value of 35% to below 15%. For larger domain lengths, the variability coefficient stabilizes at values below 10%, with the exception of the test conducted at a discharge of Q = 0.5 L/s, which exhibits higher variability.

Similarly, Figure 19b presents the coefficient of variability for BAW. For analysis domain lengths greater than five channel widths, the variability coefficient decreases significantly, from an initial value of 3.5% to less than 0.1% for higher flow rates. However, tests conducted at discharges of 0.5 L/s and 0.7 L/s exhibit relatively higher variability. The results of this analysis not only underline the importance of evaluating these metrics over a sufficiently long domain but also ensure the reliability of the data obtained through laboratory experiments.

3.3.2 Morphological Active Width - MAW

For each discharge, nine DoDs with a timespan of 0.5 Exner time are available, corresponding to the nine simulated floods. The MAW values calculated for each of the 9 available DoDs are presented in Figure 20a. In Figure 20b, the mean MAW calculated over

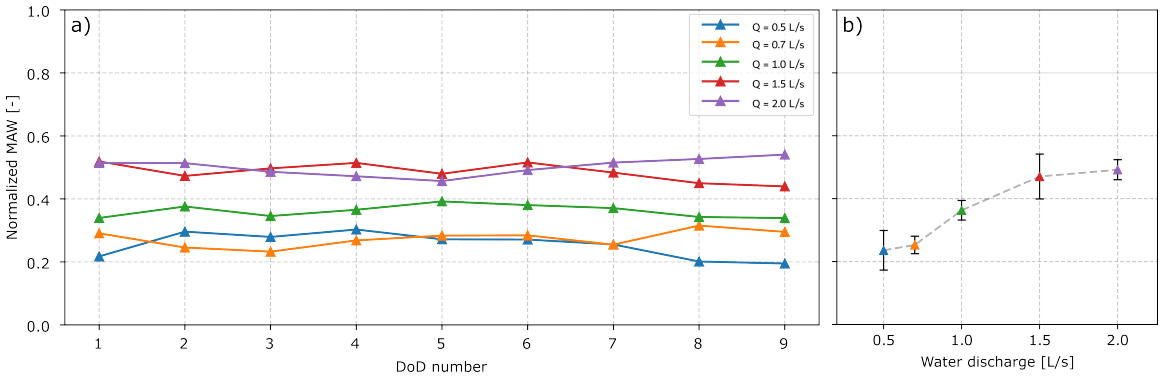

Figure 20 – The morphological active width (MAW) presented for all the available DoD at different discharges (a), and the mean value for each discharge (b). In panel (b) each triangle represents the mean of the MAW over the nine repetitions, whiskers represent one standard deviation of data variability.

the nine repetitions is presented for each discharge. The triangles denote the mean values, while the whiskers indicate one standard deviation of variability.

The MAW increases with increasing water discharge, ranging from 22% for a discharge of 0.5 L/s to 48% for a discharge of 2.0 L/s.

MAW varying survey frequency

The impact of lower survey frequencies can be explored by excluding some topographic surveys from the analysis. For instance, omitting every second DoD enables the computation of MAW over a timespan of 1 Exner time instead of 0.5 Exner time. This approach can be further extended by removing additional DEMs, simulating progressively coarser survey frequency. By systematically reducing the number of surveys, the MAW can be evaluated over timespans of up to 4.5 Exner times (see section A.1). The results for all five runs are shown in Figure 21 as a function of the time interval between surveys.

It should be noted that increasing the timespan between surveys reduces the number of available DoDs, which influences the estimation of standard deviation, as illustrated in Figure 21. Most runs exhibit a similar increasing trend in MAW values, although starting from different baseline values for a survey frequency of 0.5 Exner time. A notable exception is observed for the run with the highest discharge (Q = 2.0 L/s), where the increase in MAW values is smaller. For timespans exceeding 3 Exner times, the MAW values for 2.0 L/s are slightly lower than those for 1.0 L/s, and around 6 Exner times, they are comparable to those for 0.5 L/s.

3.3.3 Bedload Active Width - BAW

In Figure 22a, the instantaneous Bedload Active Width (BAW) values are shown over normalized time for the long preparation runs. In Figure 22b, mean BAW values are represented by coloured dots, with whiskers indicating one standard deviation of variability.

The mean and standard deviation values in Figure 22b were calculated for different discharges over the same normalized time interval. The results indicate that as discharge

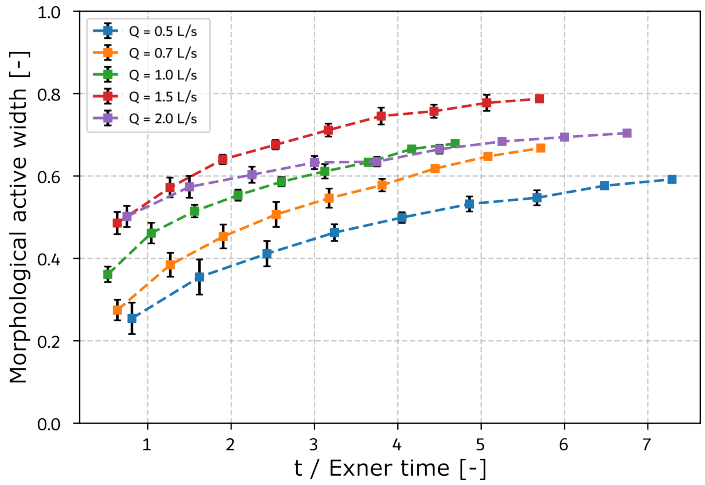

Figure 21 – The morphological active width (MAW) is here computed for different timespan. Each curve represents different discharge values. Each point on the curve represents the mean, while the whiskers represent one standard deviation of data variability.

increases, the instantaneous BAW also increases, with mean values ranging from 17% for Q = 0.5 L/s to 66% for Q = 2.0 L/s.

3.3.4 BAW and MAW comparison

The comparison between bedload activity and its morphological imprint is conducted by comparing MAW and the BAW envelope over the same time interval.

An example is provided in Figure 23, where the DoD and the bedload activity envelope map for Q = 1.0 L/s are presented, both computed over a timespan of 0.5 Exner time. Here, the BAW envelope represents the proportion of bedload activity time relative to the total run duration.

In Figure 24a, MAW and the Bedload active width computed from bedload activity map envelopes (envBAW) are compared across different discharge values. The BAW values range from 32% for Q = 0.5 L/s to 80% for Q = 2.0 L/s.

Notably, the BAW consistently exhibits higher values than the MAW, reflecting the expectation that morphological changes occur only in areas where bedload transport is present. Additionally, the BAW increases more rapidly, resulting in a widening gap between the two metrics as discharge increases.

In Figure 24a, the difference between BAW and MAW values increases with discharge. However, when evaluating the percentage difference using the following equation:

$$\frac{\text{envBAW} - \text{MAW}}{\text{envBAW}}, \tag{25}$$

a trend emerges, showing that the ratio increases with discharge. The values range from25% for Q = 0.5 L/s to 40% for Q = 2.0 L/s (Figure 24b).

By combining data from multiple runs, the BAW dataset can be expanded to construct a total envelope encompassing all available runs. In Figure 25, the BAW values for the total envelope across the nine runs are presented.

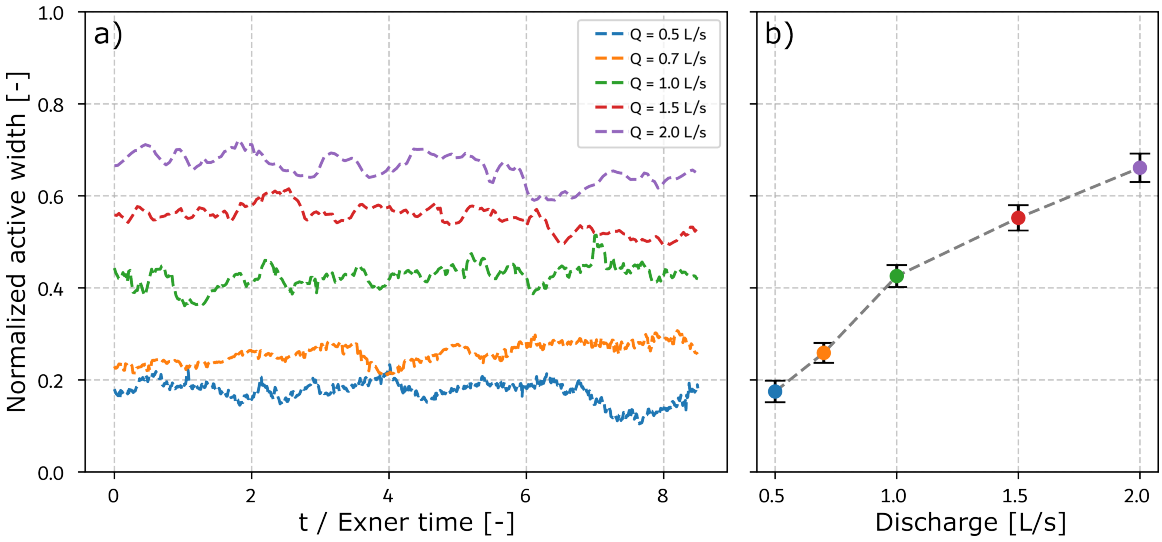

Figure 22 – The quasi-instantaneous bedload active width trend over normalized time (a) and temporally averaged BAW (b) for each discharge. The time is normalized using the Exner time.

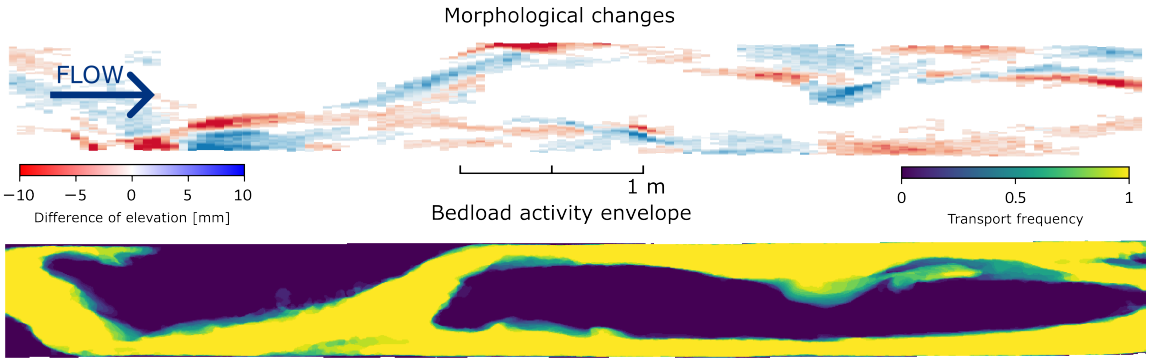

Figure 23 – Example of MAW and BAW envelope comparison for the first run of the 1.0 L/s discharge set.

In Figure 25, mean values are represented by dots, and whiskers denote the standard deviation of data variability. Since the BAW envelope is constructed by superimposing instantaneous BAW maps, it tends to progressively cover the entire channel domain over time. As a result, the upper limit of the graph in Figure 25 represents an asymptotic value to which the curves converge with a rapidity that depends on the flow rate. After approximately 5 Exner times, BAW values range from 0.6 for the lowest discharge to 1.0 for discharges of 1.5 L/s and 2.0 L/s.

3.4 Discussion

This chapter focuses on the concept of river active width, a critical parameter for assessing morphological dynamics in gravel-bed rivers. Specifically, the chapter examines the morphological active width (MAW) and the bedload active width (BAW), both of which

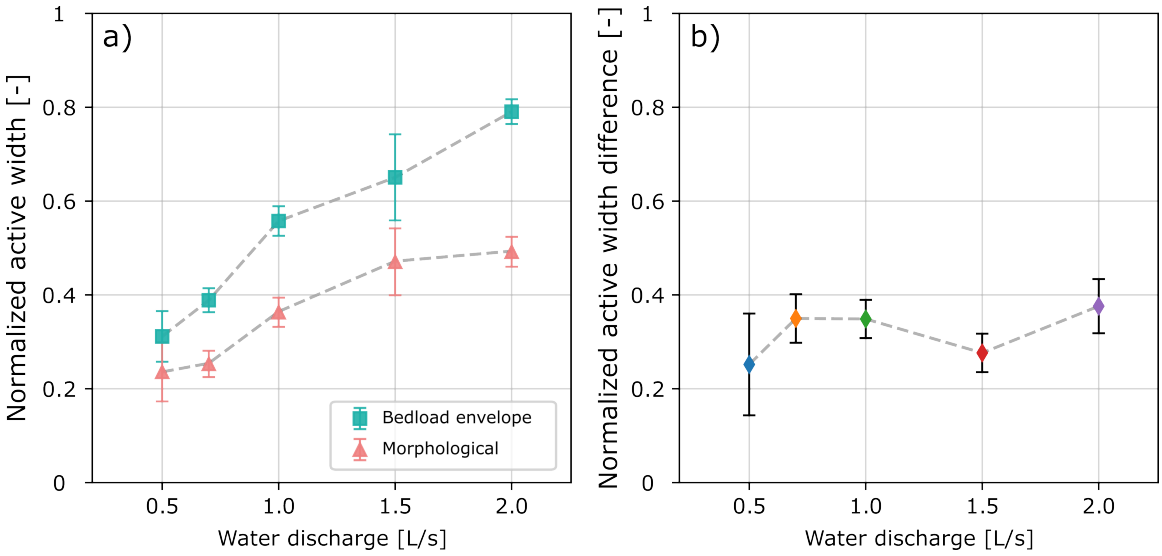

Figure 24 – Morphological and bedload active width for different discharges (a). The ratio between the morphological active width and the bedload active width envelope at increasing flowing discharge (b).

offer valuable insights into channel activity and bed stability. These metrics also facilitate a direct comparison between the area exhibiting bedload transport and the resulting morphological changes on the riverbed.

Using the experimental setup described in chapter 2, it is possible to directly compare the MAW, derived from repeated topographic surveys, with the BAW, calculated from imagery analysis. Moreover, following the methodology proposed by Garcia Lugo et al., 2015, the results can be interpreted with varying specific discharge or, in other words, changing the flow confinement.

In the experiments, the fixed channel width ensured that increasing discharge resulted in increased flow confinement, thereby producing distinct morphologies ranging from braided to wandering. As demonstrated in Garcia Lugo et al., 2015, flow confinement strongly correlates with bed morphology and bedload dynamics, providing a framework to interpret the results presented in the preceding section.

The results of this chapter are based on the measurement of two key metrics: the MAW and BAW. Although these metrics can be assessed via cross sections or punctually, e.g. by exploiting repeated surveys, painted squares and scour chains, these approaches remain limited in terms of spatial representativeness. Concerning MAW, the advent of modern topographic surveying techniques allows considerable portions of the survey domain to be surveyed by reducing time and effectively encompassing large portions of the river in a relatively short time. As far as BAW is concerned, however, any field measurements are still only possible in punctual form. Assessing the performance of these metrics spatially, i.e. varying the domain over which they are assessed, provides important insights into the procedures adopted in topographic surveying. In Figure 19, the trend of the variability coefficient as the dimensions of the analysis domain vary is presented. Within 10 widths (6.0 metres) there is considerable variability of the data, especially for smaller flows and therefore for less confined flows. The trends are monotonically decreasing for all flow rates

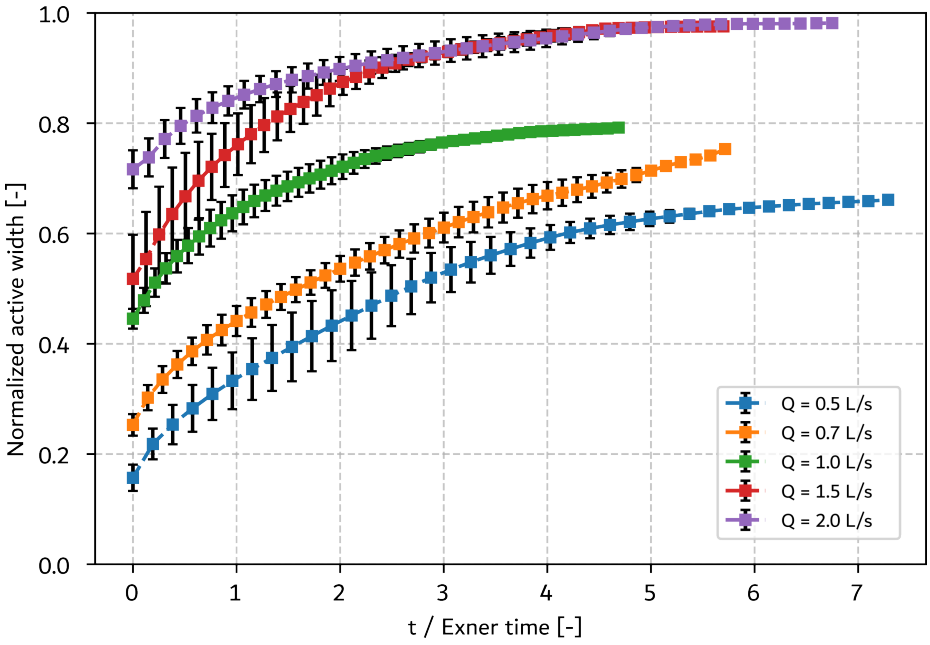

Figure 25 – The BAW trend from the envelope, computed merging consecutive runs data.

considered, and the difference in data variability depends on the specific discharge: for high confined flows the data variability tends to decrease faster than for low confined flows. This could be explained by the tendencies for wandering or alternate bars to develop a stable morphological structure that quickly reduces the variability coefficient. For example, the coefficient of variability that the flow rate at 0.5 L/s reaches after about 10 widths is reached by the largest flow rate at 2.0 L/s, considering only 3 widths. When designing repeated topographic surveys, it is therefore important to carefully evaluate the size of the domain considered, depending on the morphology and degree of flow confinement. Morphologies closer to braiding manifest greater spatial variability and, therefore in field surveys, may need a larger survey size to provide reliable information on morphological activity. The results of this chapter are based on the measurement of two key metrics: the MAW and BAW. Although these metrics can be assessed via cross sections or punctually, e.g. by exploiting repeated surveys, painted squares and scour chains, these approaches remain limited in terms of spatial representativeness. Concerning MAW, the advent of modern topographic surveying techniques allows considerable portions of the survey domain to be surveyed by reducing time and effectively encompassing large portions of the river in a relatively short time. As far as BAW is concerned, however, any field measurements are still only possible in punctual form. Assessing the performance of these metrics spatially, i.e. varying the domain over which they are assessed, provides important insights into the procedures adopted in topographic surveying. In Figure 19, the trend of the variability coefficient as the dimensions of the analysis domain vary is presented. Within 10 widths (6.0 metres) there is considerable variability of the data, especially for smaller flows and therefore for less confined flows. The trends are monotonically decreasing for all flow rates considered. For example, the coefficient of variability that the flow rate at Q = 0.5 L/s reaches after about 10 widths is reached by the largest flow rate at Q = 2.0 L/s, considering

only 3 widths. When designing repeated topographic surveys, it is therefore important to carefully evaluate the size of the domain considered, depending on the morphology and degree of flow confinement. Morphologies closer to braiding manifest greater spatial variability and, therefore, in field surveys, may need a larger survey size to provide reliable information on morphological activity.

The results indicate a significant upward trend in MAW as specific discharge increases. For low specific discharge values, MAW is approximately 20%, while for the maximum specific discharge values, the MAW reaches values of about 50%. As the specific discharge decreases, the flow is distributed across shallower channels, reducing transport capacity and consequently limiting sediment movement and detectable morphological changes.

The analysis presented in Figure 21 highlights the influence of flood duration on MAW estimation. Coarser survey frequency can be interpreted as longer flood and consequently larger temporal distance between surveys since it is not possible to perform topographic surveys during floods.

In rivers, MAW calculations are inherently tied to the scale of flood events. Longer flood durations result in higher MAW values. While the observed trends are generally consistent, the degree of lateral confinement affects the initial MAW values.

As shown in Figure 21, as the timespan between topographic surveys increases, the MAW tends to increase. Since the flume is confined by the artificial banks, it can be assumed that the flow of water will, over time, space across the total channel width. As the discharge increases, the rapidity with which the current spans the total channel width will increase.

Even for the river boundary given by discharge Q =2.0 L/s, the curve appears to be far from reaching the full channel width. This calls for reflection on the dynamics of the MAW. Increasing the timespan, the computed MAW tends to increase. However, compensation and filtering may produce zero net variation even under morphological variation for a long timespan. So, it is likely that even after a long period between surveys, not all the channel domain is likely to show up morphological variation.

Specific discharge also affects BAW values. As flow confinement increases, transitioning from braided to wandering morphologies, there is a progressive rise in the instantaneous mean BAW. This is attributed to the increased transport capacity associated with higher flow confinement, which affects a larger proportion of the channel width. A comparison of MAW and BAW (Figure 24a) reveals that MAW increases more slowly than BAW with increasing confinement. The ratio of MAW to BAW (Figure 24b) ranges from 25% for braided morphologies to 40% for wandering morphologies.

This suggests that, for lower flow confinement, thus for more braiding morphologies, MAW is closer to BAW. In other words, in this type of configuration, it appears that the bedload is more prone to lead to morphological variations and is therefore called "more morphological" (Peirce, 2017; S. Peirce et al., 2018). For high flow confinement, this closeness between MAW and BAW is lost, showing a difference in transport dynamics.

In S. Peirce et al., 2018, the MAW was calculated from laboratory experiments for five different discharge values. DoDs were calculated at a constant timespan, regardless of the trial. What is observed is that in their experiments, the trend of the MAW as the discharge increases grows faster and does not exhibit the curvature that is visible in Figure 24. This can be explained by considering the timespan between the reliefs. In our case, in fact,

higher flow rates correspond to finer timespans. This reduces the MAW value for higher flow rates. Furthermore, it is interesting to note that, even for higher flow rates, the values on average do not exceed 80 % of the total channel width. This confirms what we have seen in our experiments with regard to MAW dynamics. The continuous rework of sediment in some areas of the channel domain leads to zero variations between one relief and the next. This is of great importance when applying the morphological method or, more generally, when one wants to infer sediment transport by observing morphological variations. A limiting case may be migrating bars: if two consecutive reliefs have a timing that coincides with a migration of an entire wavelength, theoretically, null morphological variations could be observed in the face of a past in which the entire channel domain was affected by morphological variations.

The active width of a river can thus be defined in different ways, resulting in varying values. In the absence of continuous bedload transport data, MAW is often used as a proxy for river activity (Ashmore et al., 2011). However, for high specific discharge values, this approach may underestimate the proportion of the channel that is active in terms of bedload transport. For braided morphologies, characteristic of rivers with sufficient lateral space, MAW provides more accurate information on bedload activity. Thus, in this condition, MAw results as a good predictor for bedload activity and can be used to infer in bed stability and bedload dynamics.

The MAW results presented in this chapter were compared with data from field studies available in the literature. The available data consists of topographic surveys, carried out before and after a series of flood events of different durations and intensity for which hydrographs are available. The selected case studies include the Sunwapta River in Canada (Ashmore et al., 2011; S. Peirce et al., 2018), the Tagliamento River in Italy (Capito, Bizzi, et al., 2024; Capito, Pandrin, et al., 2024), and the Rees River in New Zealand (Brasington et al., 2012; Redolfi, 2014). For selected flood events, DEMs and flow measurements are available. The necessary parameters for calculating Exner time, which is essential for data comparison, were obtained using a one-dimensional model based on single cross-sections and uniform flow. The roughness parameter was extracted from the literature, where available or estimated from the roughness parameter table. This approach enabled the estimation of the relationship between flow rate and average water depth, the wet width and the bed shear stress. Additionally, sediment flux (Parker, 1990) and wetted width are computed in the model simulation. The dimensionless stream power (ω) is calculated using the following formula:

$$\omega = \frac{\mathrm{Q_S}}{\mathrm{W_w}\sqrt{\mathrm{g}\frac{\rho_\mathrm{s}-\rho_\mathrm{w}}{\rho_\mathrm{w}}\,\mathrm{d_s^3}}}$$

where Q_S is the estimated sediment flux, $\mathrm{W_w}$ is the wetted width, g is gravitational acceleration, ρ_s is the measured sediment density, and ρ_w is the water density. The duration (t) during which the flow rate Q exceeded the critical sediment entrainment discharge Q_c was used to calculate the ratio t/T_{xnr}. Exner time was determined using Equation 18, using the wet width as the length parameter. From the available DEMs, DoDs were computed, and MAW was calculated as the ratio of areas exhibiting morphological changes to the total wetted area during the flood event, according to the following formula:

$$MAW = \frac{\text{Area of morphological changes}}{\text{Reach length} \times \text{Max wetted width}}. \tag{26}$$

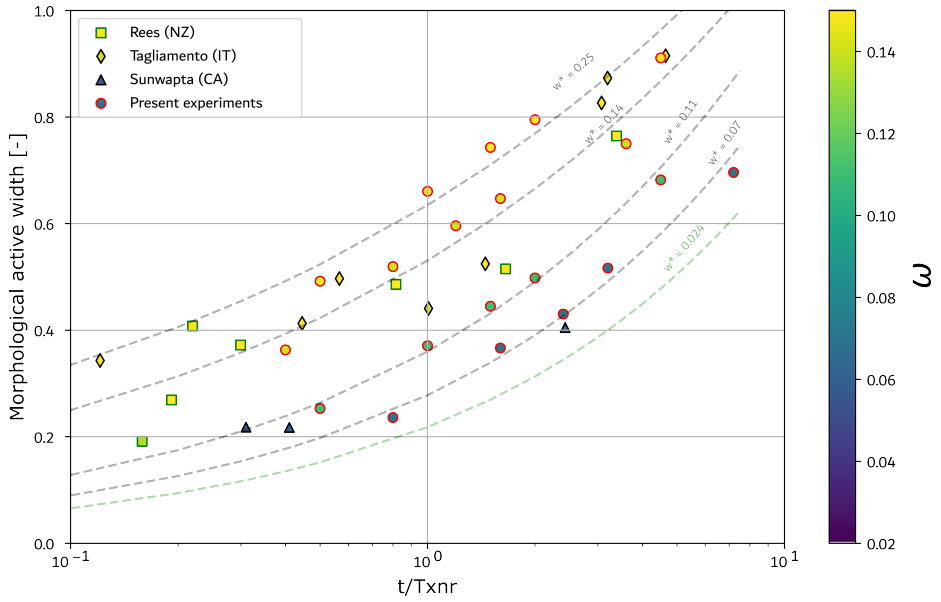

Figure 26 – Comparison of morphological active width computed for the Rees River (NZ), the Tagliamento River (IT), the Sunwapta River (CA), and the present experiments. The time axis is normalized using the Exner time and it is logarithmic. The colour ramp indicates the stream power values.

The results are presented in Figure 26, where the x-axis represents time normalized by Exner time, and the y-axis depicts MAW as defined in Equation 26. As shown in Figure 26, in the three cases presented here, the calculation of Exner time gave comparable results to those chosen for the flood duration in the laboratory. In light of the experimental results and the Exner time of the floods presented in the case studies, the importance of the effects of flood duration in the estimation of MAW emerges. The experimental data also show that flood duration, rather than flood magnitude, plays a key role in MAW estimation. In fact, for all the case studies, the point at greatest t/Txnr in the graph corresponds to the point at which MAW is estimated through the sum of all floods. In the three cases considered here, the event scale is about 1 Exner time. This draws attention to the relationship between the time scale (in the field) and the calculation of the MAW. Indeed, it emerges that the time scale is an element to be taken into account when assessing MAW from field surveys. Furthermore, as the duration of the flood increases, MAW also increases, underscoring the critical role of survey frequency in estimating morphological changes.

CHAPTER 4
NON-MORPHOLOGICAL BEDLOAD

The previous chapter studied the relationship between the bedload and its morphological footprint. Two important metrics were introduced: the morphological active width (hereafter MAW) and the bedload active width (hereafter BAW). Both were computed by evaluating the mean channel width that experienced morphological changes or bedload activity respectively, divided by the total channel width.

In the impossibility of obtaining continuous measurements of sediment transport, MAW is a metric that is used to estimate channel dynamics. It is measured by comparing topographic surveys performed at different timespan and provides the proportion of the channel that experienced net morphological changes. The results obtained show that not all areas active in terms of bedload show appreciable morphological changes, and that therefore morphological changes may provide an underestimate of activity in terms of bedload. The concept of non-morphological bedload was therefore introduced, as a component of bedload that does not produce appreciable morphological changes. Moreover, the previous chapter highlights that the MAW fails in predicting the BAW for high flow confinement, while for low specific disharge value the MAW and the BAW tend to get closer. In this chapter, we will investigate non-morphological bedload, assessing the processes involved and whether this is influenced by the specific flowing discharge.

4.1 Experimental design

The experimental setup used is described in detail in chapter 2. The experimental data employed in this analysis are identical to those described in chapter 3, to which the reader is directed for a detailed description of the experimental design. Key information regarding the various experimental runs is summarized in Table 1.

4.2 Research questions

This chapter seeks to address the following research questions:

- RQ1: What processes govern non-morphological transport?
- RQ2: How does non-morphological transport vary with river confinement and flood duration?
- RQ3: What are the defining characteristics of areas where non-morphological transport occurs?

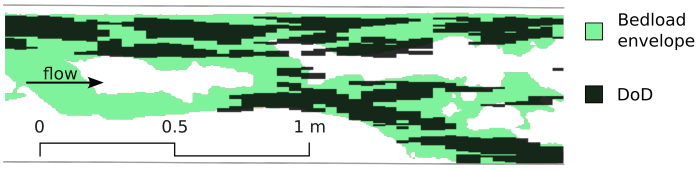

Figure 27 – Example of BAW envelope (green) and morphological active area (black) at a time discretization of 0.5 Exner times. Non-morphological bedload is present where morphological changes (black) are absent.

4.2.1 What is the non-morphological bedload?

By "non-morphological bedload," we refer to a set of conditions rather than a specific phenomenon associated with sediment transport in rivers. In general terms, areas experiencing bedload transport without detectable morphological variations are classified as affected by non-morphological bedload. This definition requires clarification, particularly in light of the limitations inherent in measuring morphological variations. Whether in laboratory flumes or natural rivers, morphological changes are typically measured at the event scale, comparing conditions before and after a flood event. Continuous measurement of morphological changes during floods is not feasible. Consequently, the definition can be refined as follows: non-morphological bedload refers to areas that experience bedload transport but exhibit zero measured morphological change.

An example of non-morphological transport observed during the experiments is presented in Figure 27, where the green areas indicate regions experiencing bedload transport (as observed from the timelapse images), while the black areas represent regions with observable morphological changes, in the same period of time. Referring to Figure 27, it is evident that a significant overlap exists between areas experiencing bedload transport and those showing morphological changes. However, a non-negligible portion of the bedload transport occurs without corresponding morphological variations.

4.2.2 Non-morphological bedload components

To provide a comprehensive explanation, three components contributing to non-morphological bedload are identified. These components relate to the sediment transport dynamic, the methods used to observe morphological variations and the limitations of the measurement instrumentation. These components are discussed in detail below.

Equilibrium transport

The first identified component, referred to as “equilibrium transport,” is derived from Exner’s equation (Equation 12) and the associated mass balance between two control sections. According to Exner’s equation, a change in bed elevation over time occurs due to spatial variation in the solid flow rate q_s. In the absence of spatial variation in q_s, changes in bed elevation cannot be detected, even if bedload transport occurs. This represents a condition in which the sediment inflow from upstream equals the sediment outflow downstream, resulting in a constant sediment volume within the control volume and, consequently, a

stable average bed elevation over time.

Mathematically, equilibrium transport occurs when the spatial derivatives of the sediment flux are zero:

$$\frac{\partial q_s}{\partial x} = \frac{\partial q_s}{\partial y} = 0. \tag{27}$$

Compensation effects

The second component, termed "compensation," occurs when alternating episodes of scour and fill take place at the same location during the time interval between consecutive topographic surveys (Ashmore and Church, 1998; Goff and Ashmore, 1994b; Lindsay and Ashmore, 2002). Compensation affects the estimation of scour and fill volumes and, consequently, the accuracy of sediment transport calculations based on step-length approaches (Ashmore and Church, 1998; S. N. Lane et al., 1995; McLean and Church, 1999; Nicholas and Sambrook Smith, 1998; Pandrin and Bertoldi, 2024) and the assessment of channel stability (Ashmore and Church, 1998; B. Lane et al., 2022; S. N. Lane et al., 2003).

In some cases, compensation may influence the estimation of morphological active width, although its impact is typically less pronounced. For example, when the algebraic sum of scour and fill depths equals zero, compensation directly affects the active width. This specific scenario, referred to as "pure compensation," occurs when consecutive surveys measure identical bed elevations at a given location despite intermediate episodes of scour and fill.

Filtering effects

As described in section 2.4, the DoD analysis incorporates a filtering algorithm to eliminate possible errors and unrealistic variations in the DoD. This filtering process can affect the identification of areas with minimal morphological changes, including those caused by grain settling or slow morphological evolution. Consequently, areas with subtle morphological changes may not meet the detection threshold established by the algorithm.

4.3 Results

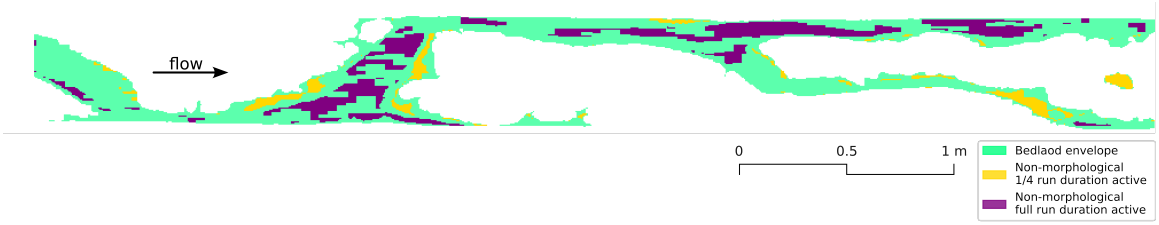

Figure 28 – Example of non-morphological bedload activity duration for Q = 0.7 L/s. The figure highlights areas that are active for at least 1/4th of the run duration and areas that are active for the entire run duration compared with the total bedload (green).

Table 3 – DoD scheme for compensation and filtering effects estimation.

DoD	Timespan	Compensation effects	Filtering effects
DoD 1-0	1	Scour (Fill)	No changes
DoD 2-1	1	Fill (Scour)	No changes
DoD 2-0	2	No changes	Scour or Fill

The analysis begins with an investigation into the duration of bedload activity in areas of non-morphological transport, and thus to assess their contribution in terms of activity duration. In order to assess the distribution of the most active areas from the least, a simplified class division was chosen. Specifically, we assess how long these areas remain active and whether the duration of activity varies spatially, creating discernible patterns. The areas affected by non-morphological bedload were categorized based on their duration of activity during each experimental run. Active areas were classified into two groups: those active for less than one-quarter of the run duration and those active for more than three-quarters of the run duration.

For instance, Figure 28 presents the results of this classification for a run conducted at a flow rate of Q = 0.7 L/s. Similar spatial patterns were observed for different flow rates.

Areas active for less than one-quarter of the run duration (highlighted in yellow) are generally fragmented, small, and located at the periphery of the bedload active area. In contrast, areas active for more than three-quarters of the run duration (highlighted in purple) tend to be more compact and extensive, situated near the center of the active bedload areas. These preliminary analyses indicate that non-morphological bedload is significant in terms of activity duration, warranting further investigation.

4.3.1 Non-morphological bedload components estimation

The objective of this section is to estimate the bedload components identified in the previous section. To ensure consistency with earlier analyses, the estimation of these three components is expressed as a proportion of the total channel width. This is achieved by dividing the areas where each of the components is identified by the total channel area. Such an approach facilitates direct comparison with previously reported results.

The compensation and filtering components can be quantified by considering the structure of the data obtained from the topographic survey (Figure 55) and the information presented in Table 3.

Consider two consecutive DoDs at the finest temporal discretization (e.g., DoD1-0 and DoD2-1) and the DoD encompassing both (DoD2-0), the latter having a temporal resolution twice as coarse. Compensation occurs when a switch between scour and fill (or vice versa) is observed. Specifically, pure compensation arises when the consecutive DoDs at the finest timespan exhibit opposite morphological changes, while the overall DoD (DoD2-0) records no morphological change. This scenario reflects a case in which the morphological changes in individual DoDs (DoD1-0 and DoD2-1) have equal magnitudes but opposite signs, thereby canceling each other when assessing the morphological changes between

DEM0 and DEM2 using DoD2-0.

Using the available data, it is possible to map compensation occurrences at a temporal resolution equal to half of the finest available discretization. Furthermore, this analysis can be extended to increasingly coarse temporal discretizations.

By referring to Table 3, it is also possible to identify areas influenced by the filtering effect of the algorithm processing the DoDs. For instance, consider two consecutive DoDs in which no morphological change is recorded (e.g., DoD1-0 and DoD2-1) and a combined DoD (DoD2-0) that does record morphological change. In this case, DoD1-0 and DoD2-1 develop morphological changes below the detection threshold, which are filtered out, resulting in no recorded change in the individual DoDs. However, a measurable change is detected when evaluating morphological changes over a longer temporal interval (DoD2-0). As with compensation, areas affected by filtering effects can be estimated at a temporal resolution equal to half of the finest available discretization. The results are presented in Figure 29 for varying river confinement conditions and increasing flood durations.

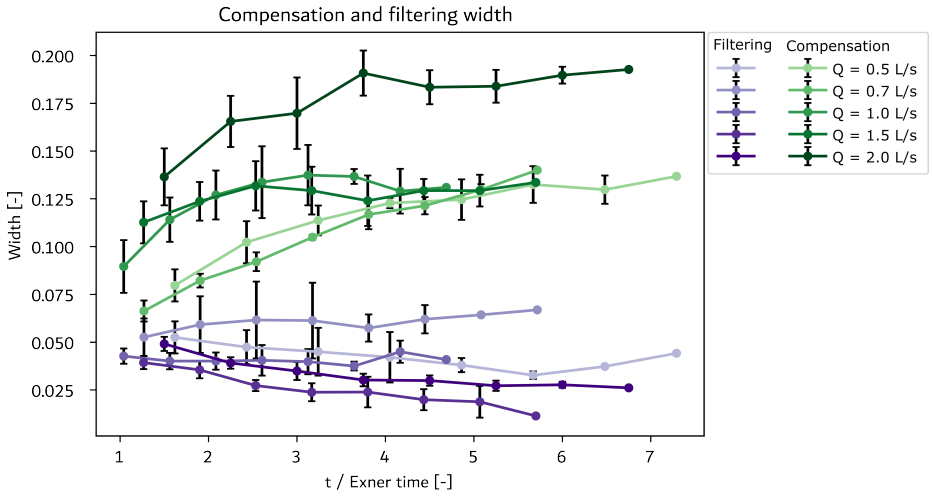

Figure 29 – Values of total width portion that experienced compensation (green) and filtering effects (purple) for each discharge, changing flood duration. Dots reveal mean values and whiskers reveal data variability.

As shown in Figure 29, the effect of compensation increases with flood duration. For the finest timespan, compensation ranges from 7% for Q = 0.5 L/s to 13% for Q = 2.0 L/s. At longer flood durations, compensation values increase to 12% for Q = 0.5 L/s and 20% for Q = 2.0 L/s. Although an upward trend is observed across all runs, it is noteworthy that, for flood durations equivalent to the longest observed, compensation stabilizes at approximately 12% for all runs except Q = 2.0 L/s, which deviates significantly, reaching 20

The normalized active width of areas affected by filtering remains lower than that of areas influenced by compensation. Except for the flood run at Q = 0.5 L/s, a decreasing trend in filtering effects is observed as flood duration increases. For the maximum temporal discretization of 0.5 Exner time, the values are approximately 5%, whereas for flood durations around six Exner times, the values range from 2% for Q = 2.0 L/s to 7% for Q = 0.5 L/s.

The compensation and filtering components enable a more accurate estimation of morphological variations. By definition, the MAW (Figure 21)—augmented by the compensation component and reduced by the filtering component—represents the envelope of the all DoDs map at 0. 5 Exner time. In fact, the Morphological active width computed from morphological changes map envelopes (envMAW) can be computed to estimate, at the maximum discretization available, which areas exhibit morphological changes during the succession of runs performed at constant discharge. By summing an increasing number of consecutive DoD maps (where 1 means morphologically active and 0 means inactive) we can obtain a map that shows how many time a certain survey cell has been active. This allows us to compare the morphological active area over the consecutive runs exploiting the 0.5 Exner time discretization instead of considering DoDs at increasing timespan.

The relationship between the various bedload components and their morphological imprints is illustrated in Figure 30.

Filtering effects on the active width are represented in purple, while compensation effects are shown in green. The MAW, the MAW derived from envelopes, and the BAW derived from envelopes are depicted in grey, blue, and red, respectively. As highlighted at the beginning of this chapter, the area between the grey and red curves corresponds to non-morphological bedload, representing portions of the channel experiencing bedload transport without measurable morphological changes. Notably, the gap between the curves remains nearly constant as flood duration and lateral confinement vary. Part of this gap can be attributed to survey frequency effects. By utilizing the maximum temporal discretization in the topographic survey and generating individual DoD maps, this area is significantly reduced.

It is important to note that the pure compensation evaluated here specifically pertains to its impact on the active width.

The component of non-morphological transport associated with equilibrium bedload remains to be evaluated. The non-morphological transport lies, excluding filtering effects, between the grey and red curves in Figure 30. Consequently, the component related to equilibrium bedload lies between the blue and red curves.

As illustrated in Figure 30, the component related to equilibrium bedload increases as the lateral confinement rate increases. With increasing flood duration, the non-morphological bedload remains almost constant, whereas the compensatory component increases, thereby reducing the component associated with equilibrium transport. For the lowest lateral confinement rate, corresponding to the discharge of 0.5 L/s, the equilibrium bedload component diminishes entirely after approximately six Exner times.

By focusing on the equilibrium bedload, its contribution throughout the flood duration and under varying flow confinement conditions can be evaluated. In Figure 31, the trends of equilibrium bedload relative to the total bedload are presented. As shown, the percentage of bedload classified as equilibrium decreases progressively with increasing flood duration across all levels of flow confinement. Additionally, the equilibrium bedload percentage depends on the specific flow rate. For the same flood duration, the proportion of equilibrium bedload relative to the total decreases as specific discharge decreases. For example, at approximately six t/T_{xnr}, the equilibrium bedload proportion is about 10% for the discharge of 2.0 L/s, whereas it approaches 0% for the discharge of 0.5 L/s.

The structure of the available data enables the spatial localization of the various com-

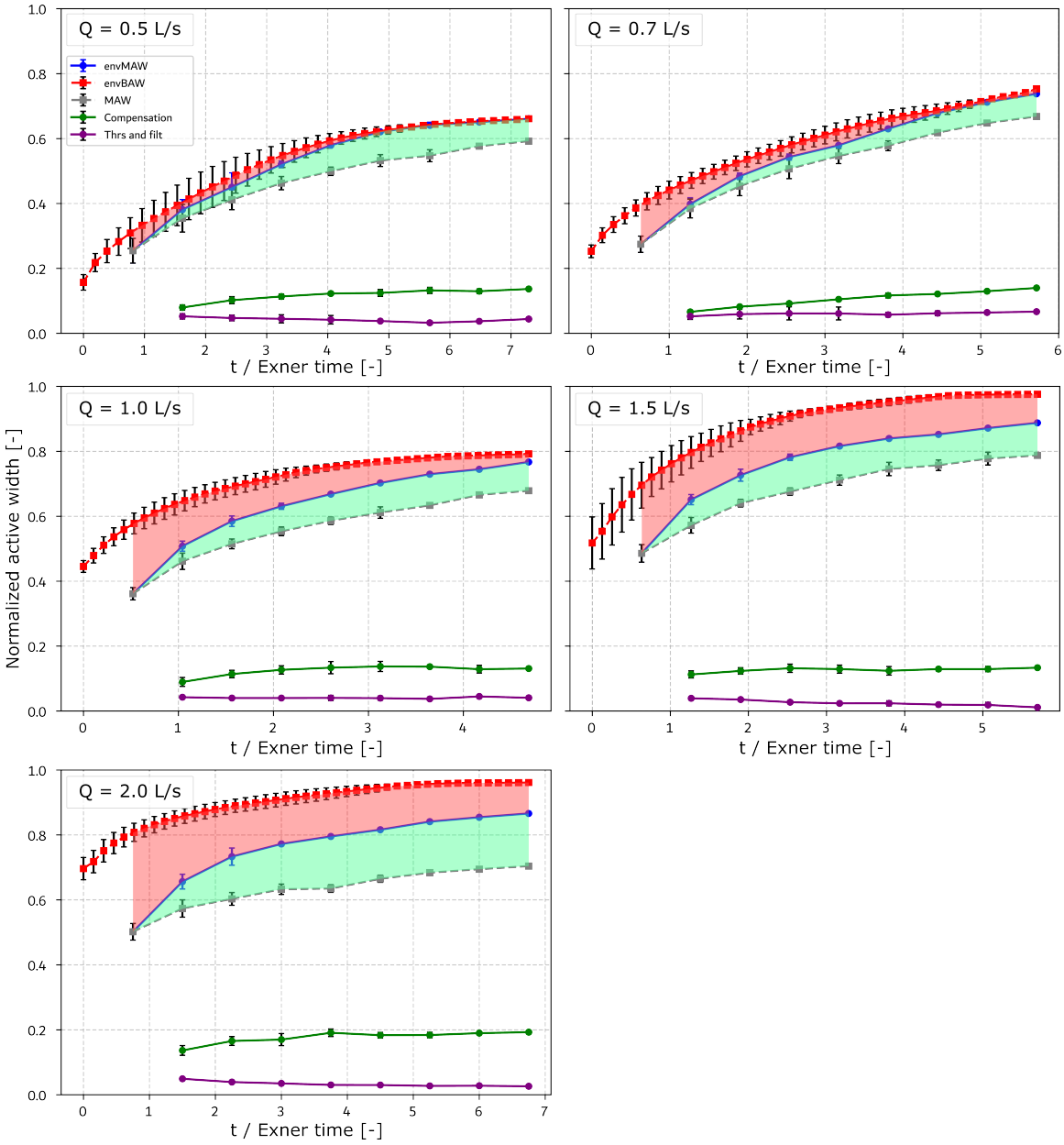

Figure 30 – Filtering component (purple), compensation component (green), MAW (grey), envMAW (blue) and envBAW (red). The compensation and filtering component (green area) and the "equilibrium" component (red area) are highlighted. Dots represent mean values and whiskers represent data variability. Results are presented for each discharge, varying the flood duration.

ponents of non-morphological bedload. Specifically, it is possible to identify areas where compensatory effects occur, where the filtering algorithm acts, and where equilibrium bedload is present. In Figure 32, an example map is provided, illustrating these components for the lowest (0.5 L/s) and highest (2.0 L/s) river confinement levels. All runs exhibit similar spatial patterns in the components of non-morphological transport.

The areas affected by filtering are fragmented and predominantly located in peripheral

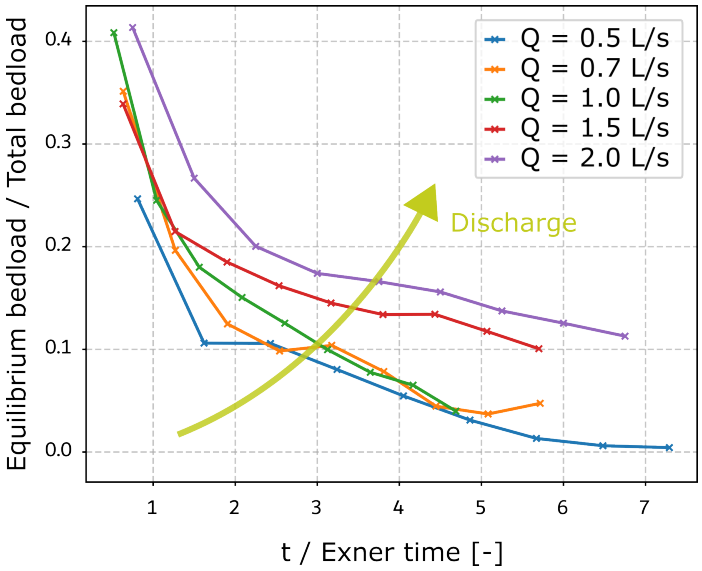

Figure 31 – The ratio between the "equilibrium" bedload and the total bedload is presented for each discharge, varying the flood duration.

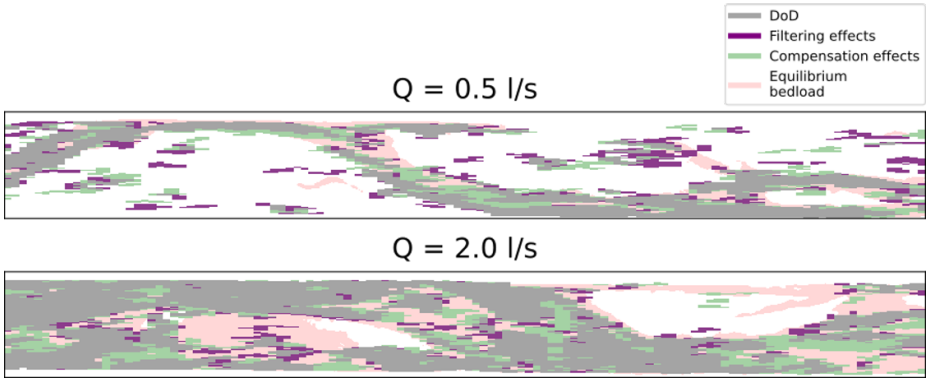

Figure 32 – Morphological and bedload activity components localized on the channel domain for the Q = 0.5 L/s and Q = 2.0 L/s discharge. Flow from left to right.

regions. Conversely, areas influenced by compensation are less fragmented and more centrally situated within the bedload active area. Areas associated with equilibrium transport are distributed across both peripheral and central zones within the bedload active area.

4.3.2 Non-morphological bedload intensity

The spatially distributed information facilitates further analysis. One important question is the characteristics of the active areas in terms of bedload intensity. By utilizing data from time-lapse imagery, spatial information on bedload intensity is obtained (see chapter 2), allowing an investigation into the intensity of bedload in areas influenced by different components of the non-morphological bedload.

In Figure 33, the bedload intensity is depicted for the various bedload components. The data were extracted using the finest available temporal discretization (1.0 Exner times) and

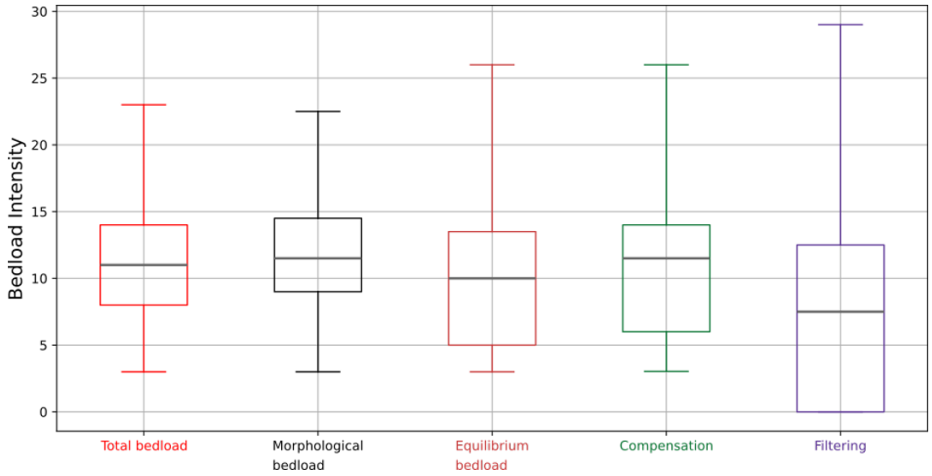

Figure 33 – Boxplot with the bedload intensity values divided into different categories. Bedload intensity is presented in terms of delta saturation. Results are presented for the Q = 0.5 L/s discharge. Different discharges reveal similar trends.

refer to Q = 0.5 L/s. Runs at different discharges reveal similar trends. The categories presented include: the total bedload (corresponding to the bedload active area), the morphological bedload, and the three components of non-morphological bedload (equilibrium, compensation, and filtering). On the y-axis, the saturation difference between consecutive images is displayed, serving as a proxy for bedload intensity (for additional details on this technique, refer to Redolfi et al., 2017).

As shown in Figure 33, the equilibrium bedload exhibits intensities comparable to those of the morphological bedload. Similarly, areas subject to compensation display intensities analogous to those of the equilibrium bedload and the morphological bedload. In contrast, areas affected by filtering exhibit lower intensity values compared to the other categories of non-morphological bedload.

4.4 Discussion

This chapter investigates the bedload component that does not result in detectable morphological changes, referred to as the non-morphological bedload.

The analysis of the activity duration in areas characterized by non-morphological bedload reveals distinct spatial patterns when dividing these areas into those active for more than 3/4 and less than 1/4 of the total flood duration. Preliminary observations suggest that the non-morphological bedload active for more than 3/4 of the flood duration is localized in compact, central regions aligned with the flow direction. These regions, while non-negligible in extent compared to the total bedload-active area, exhibit spatial continuity in their patterns. This continuity indicates that the phenomenon is not localized but rather associated with sediment transfer along flow directions. Consequently, it is plausible that a significant portion of bedload, in terms of both sediment transport contribution and activity duration, does not produce detectable morphological changes.

Three distinct components of the non-morphological bedload are identified:

- Compensatory phenomena occur when a transition between scour and fill phases is observed between successive topographic surveys (Lindsay and Ashmore, 2002; Pandrin and Bertoldi, 2024). Regarding active width, only pure compensation leads to a loss of information. Within the investigated flood duration range (Figure 30), the effect of compensation increases with flood duration. After one Exner time, pure compensation affects an average of 7 % of the total width for the lowest specific discharge and 14 % for the highest specific discharge. These percentages increase to 13 % and 20 %, respectively, after a flood duration of six Exner times. Compensation strongly depends on the frequency of topographic surveys: higher survey frequency improves the resolution of morphological changes. In scenarios lacking high-frequency bed elevation monitoring, where surveys are conducted in dry conditions via event scaling, quantifying compensation effects is critical for accurately estimating channel activity and bedload contributions Pandrin and Bertoldi, 2024.

- Filtering effects in morphological variation assessments are influenced by survey instrumentation and the relationship between morphological changes and sediment size. Although less significant than compensation, the areas impacted by filtering also show a dependency on flood duration. Notably, the filtering-related component exhibits an opposite trend to compensation. As survey frequency increases, the impact on active width grows. For a flood duration of one Exner time, filtering-related effects range from 1% to 5% for the maximum simulated flood duration and stabilize at approximately 5%, irrespective of specific discharge values (Figure 29).

- The third component is equilibrium bedload, characterized by an equilibrium condition where bedload does not induce morphological changes (Equation 27). This component is identified by exclusion from the compensatory and filtering components. Furthermore, it is spatially localized in areas of pure equilibrium transport, where no compensation or filtering occurs. During a flood, equilibrium transport may also occur alongside compensatory or filtering effects.

In Figure 30, these three components are depicted as flood duration increases. Given the relationship between survey frequency and compensatory effects, the equilibrium transport component is likely underestimated. With higher survey frequencies, the initial point of the envMAW curve (blue), which coincides with the MAW curve, would be positioned lower than for a survey frequency of 0.5 Exner time. Consequently, the envMAW envelope curve would shift downward, increasing the equilibrium transport component. This trend would persist until filtering effects, which intensify with shorter survey intervals, dominate.

Compensation effects increase with both flow confinement and flood duration, indicating a heightened tendency for bedload to rework the same areas rather than migrating laterally. When the flow is less confined, lateral migration reduces compensatory effects. For instance, constant lateral migration within a steady cross-section does not generate compensation. Brading rivers show high lateral dynamics with a positive relation with the discharge (Middleton et al., 2019), and experience fewer compensatory effects. However, as flood duration increases, compensatory effects intensify across all confinement levels. This is because longer flood durations result in more areas undergoing scour-and-fill transitions, increasing the likelihood of MAW being affected.

In the application of morphological methods, compensation is often considered to be the only component that can appear in the balance, leading to an underestimation of morphological changes and thus of solid transport. These analyses show how the equilibrium bedload can play an important role and lead to a significant underestimation of the bedload in the application of the morphological method. The equilibrium bedload component is often overlooked or completely ignored. With this in mind, the results presented in this chapter lend themselves to new interpretations of previously obtained results, and the variability of the morphologies of the experiments is easily adapted to provide new possible applications of the morphological method. The equilibrium bedload (Figure 30 and Figure 31) decreases significantly as the specific discharge decreases and as the flood duration increases. In low-confinement contexts, the flow tends to disperse into a greater number of channels, resulting in shallower flow depths. Consequently, the transport capacity approaches the entrainment threshold. As a result, bedload transport is reduced and may exhibit greater spatial variability. This increased spatial variability renders the transport more morphological, as bedload is more likely to produce detectable morphological variations. Results from S. Peirce et al., 2018 suggest that the morphological active width, bulk change, and bedload transport rates all exhibit a similar lower threshold for detection around $0.17\ Wm^{-1}$ (1.14 L/s, $\omega^* \sim 0.09$). This indicates that in dynamic rivers, there is no significant bedload transport without observable net morphological change at the channel scale. Traditionally, bedload entrainment thresholds have been defined at the grain scale (Buffington and Montgomery, 1997); however, evidence from the experiments carried out by S. Peirce et al., 2018 suggests that the grain-scale bedload threshold may be similar, if not identical, to the threshold for detectable morphological change in braided rivers (see also Peirce, 2017). The importance of this finding lies in its confirmation that bedload transport in braided rivers involves more than just the exchange of grains on a static bed. Rather, it encompasses active processes of erosion and deposition that are both driven by and regulated by the river's morphology. Conversely, higher specific discharge leads to more concentrated bedload transport, potentially characterized by reduced spatial variability.

As flood duration increases, the contribution of equilibrium bedload tends to decrease across all degrees of confinement. This trend is likely related to the temporal variability of bedload transport. Equilibrium bedload corresponds to temporally stable conditions, but as flood duration increases, the areas that exhibit exclusively equilibrium bedload decrease rapidly, especially in contexts of high spatio-temporal variability.

The findings discussed thus far illustrate the challenges of estimating active areas in terms of bedload from morphologically active areas. These difficulties arise from the underestimation of morphologically active areas (due to compensatory and filtering effects) and the inability to map active areas in terms of equilibrium bedload using topographic surveys alone.

Furthermore, the results presented in Figure 33 indicate that the non-morphological bedload component, in terms of intensity, is comparable to that of the morphological bedload. The lowest intensities are observed in areas with minimal morphological variations, such as those influenced by filtering. By contrast, areas affected by compensation and equilibrium bedload exhibit transport intensities comparable to those of morphological and total transport. These findings suggest that sediment fluxes associated with non-morphological

transport are not negligible.

The presence of non-morphological bedload does not compromise the reliability of the inverse method as described in Ashmore and Church, 1998; Vericat et al., 2017. However, it does negatively impact sediment transport estimation using morphological methods, where the calculation of bedload flux is affected by compensatory and filtering effects, as well as the non-negligible equilibrium bedload component.

The application of virtual velocity methods and path length estimation will be discussed in detail in Chapters chapter 5 and chapter 6. With respect to the estimation of non-morphological bedload, which is the focus of this chapter, it is evident that flow confinement significantly influences its impact on bedload transport estimates. In low-confinement morphologies, the non-morphological transport component appears to be substantially lower, although its precise quantification remains challenging. These observations underscore the importance of applying such methods under optimal conditions, where more accurate estimates can be obtained.

CHAPTER 5
TRACERS DISPLACEMENT ANALYSIS

The use of tracers is an effective but time-consuming methodology to study sediment dynamics (Hassan and Roy, 2016). The use of tracers provides information on sediment mobility in terms of travel distance and displacement patterns (Church and Hassan, 1992a; Ferguson and Wathen, 1998). It is known that morphology plays a key role in tracer displacement and that this influences the distance travelled by the sediment, but a clear relationship has not yet been formulated (Church and Hassan, 1992b; McDowell and Hassan, 2020; Papangelakis and Hassan, 2016).

In this chapter we will investigate the relationship between morphology and tracer displacement using a laboratory flume and fluorescent and paramagnetic tracers.

5.1 Research questions

This chapter seeks to address the following research questions:

- RQ1: what is the effect of morphology and morphological changes on tracer displacement patterns?
- RQ2: can morphological dynamics allow us to predict tracer displacement?

5.2 Experimental design

This chapter presents the results of three sets of runs, conducted in the laboratory flume described in chapter 2. Each set of runs is characterised by a constant discharge released into the flume. The discharges tested are Q = 0.5 L/s, Q = 0.7 L/s e Q = 1.0 L/s. All tests are conducted starting from a morphology generated by a constant discharge Q = 1.0 L/s that can be considered as the formative discharge. During each run, the position of fluorescent tracers is investigated using image time-lapses that provide every 4 seconds a photograph of the entire tracers population along the channel domain. The experimental setup is presented in chapter 2. The experiments result in a set of 12 runs for each discharge, for a total of 36 runs. The complete experiment scheme is reported in Figure 56.

In Figure 34 the workflow followed for each set of discharges is presented, which is divided into the following phases:

- **Phase 1**: starting from a flat morphology, a constant flow rate Q = 1.0 L/s flows for an estimated period of 30 Exner times. This leads to a characteristic equilibrium morphology for the formative discharge of Q = 1.0 L/s. The Q = 1.0 L/s is, thus, the formative discharge for all three sets of runs.

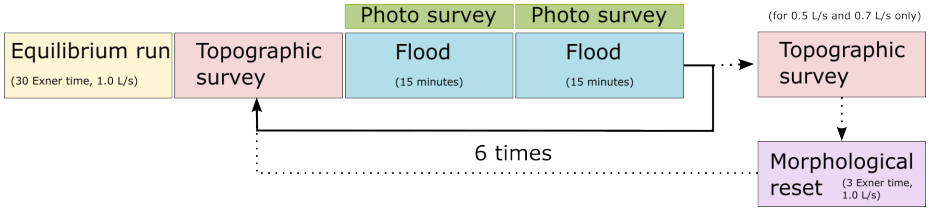

Figure 34 – Scheme describing the experimental workflow for each set of discharge. The morphological reset is carried out every 2 runs for discharges other than the formative discharge.

$Q[l/s]$	0.5	0.7	1
$h[\,\mathrm{m}]$	0.0075	0.0077	0.0079
$W_{\mathrm{Wet}}/B[-]$	0.51	0.66	0.83
$BAW/W_{\mathrm{Wet}}\,[-]$	0.35	0.37	0.41
$\theta[-]$	0.019	0.026	0.036
$\theta_{\mathrm{active}}\,[-]$	0.070	0.073	0.077
Exner Time $[\,\mathrm{min}]$	319	156	69

Table 4 – Main parameters for each run.

- **Phase 2**: a topographic survey is conducted before starting the tracer experiments, and then two consecutive experiments using tracers are carried out. Tracers are placed in specific cross-sections (one for each experiment release), and tracers are placed where bedload is observed to avoid unnecessary sediment contamination by tracers. The duration of each run is 15 minutes, the flow rate is constant and depends on the test set. During each run, the channel is illuminated by UV lights to make the tracers visible, and a photographic survey produces a timelapse with a timespan of 4 seconds to provide tracer's position over the channel domain. At the end of each run, the entire channel is monitored with UV light to collect all the present tracers using a magnet. This ensures a full tracer's recovery. The different runs are carried out by moving the analysis area from downstream to upstream along the laboratory flume. Although tracers are recovered at the end of each run, this reduces the effects of any tracers exhumed during the run. Every two runs, a topographic survey is carried out. For Q = 0.5 L/s and Q = 0.7 L/s only, a third phase is necessary to maintain the morphology.

- **Phase 3**: when the flow rate during the runs is different from the formative flow rate Q = 1.0 L/s, after two consecutive runs a topographic survey and morphological reset is carried out to re-establish an equilibrium morphology at Q = 1.0 L/s. The morphological reset consists of an equilibrium run during which a Q = 1.0 L/s constant discharge flows to re-establish the formative discharge morphology.

Morphological changes are computed, making the difference between DEMs. This produced scour and deposition maps for each run following the methodology presented in chapter 2.

The main parameters of each run are presented in Table 4. The variables presented in Table 4 are averaged values, and the critical Shields number θ_c used for calculating

the bedload active width is 0.047, based on the Meyer-Peter and Müller (1948) formula. The Shields number θ is computed over the wetted width W_{Wet}, while the active Shields number θ_{active} is calculated for the active width W_{active}. At a flow rate of Q = 1.0 L/s, the stream nearly occupies the entire channel width W, while at lower flow rates, the W_{Wet}/W ratio decreases.

For each run, the timelapses are analysed using a Python script (see section 2.6 for more details) that extracts tracer position with respect to the reference system of the photographic survey. Only a portion of the entire run duration is analyzed. The time at which the flow rate released reached the set constant value was considered as the start time of the run. The system start-up time that brings the laboratory flume from simple hydration to the set discharge value was therefore eliminated (see section 2.6 for more details). By continuously monitoring the number of tracers present during the run, it was decided to terminate the analysis once the number of tracers present in the flume fell below 75% of the maximum reached, since tracers move downstream over the analysis domain. This makes it possible to focus the analysis on sediment transport dynamics that are consistent with the size of the survey area.

5.2.1 Tracer position and topographic information

Taking advantage of the experimental setup described in detail in chapter 2, it is possible to couple the position of the tracers extracted from the timelapse with data on the elevation (DEM) and morphological dynamics (DEM of Difference - DoD). The position of the tracers on the timelapse is converted concerning the reference system of the topographic survey. Thus, it is possible to associate each detected tracer with an elevation and a DoD value. Tracer elevation and related DoD vaule are extracted considering the closest DEM and DoD available.

5.3 Results

At the beginning of each run, as the water flows through the channel, the areas where sediment transport is present are identified. Tracers are placed in the areas where transport is visible, making a cross-sectional strip that slightly exceeds the area involved in transport. During the run, the tracers move downstream, and after an initial entrainment phase, they tend to settle mainly in shallow areas and/or where transport is very low. Some tracers travel a long distance in the initial phase, moving directly out of the frame boundaries. The effect of morphology is significant as the presence of bifurcations and confluences influence the tracer trajectories. One element that has generated great variability in the runs is the feeding point, i.e. the position of the stream-wise stripe of the tracers. In some cases, the tracers travelled a very short distance and stopped after a few tens of centimetres. In other cases, the tracers separated due to the presence of a bifurcation. In others, it was possible to set up two feeding points by exploiting the presence of two parallel active channels. In the latter configuration, in some cases, it happened that the two branches converged into a single branch.

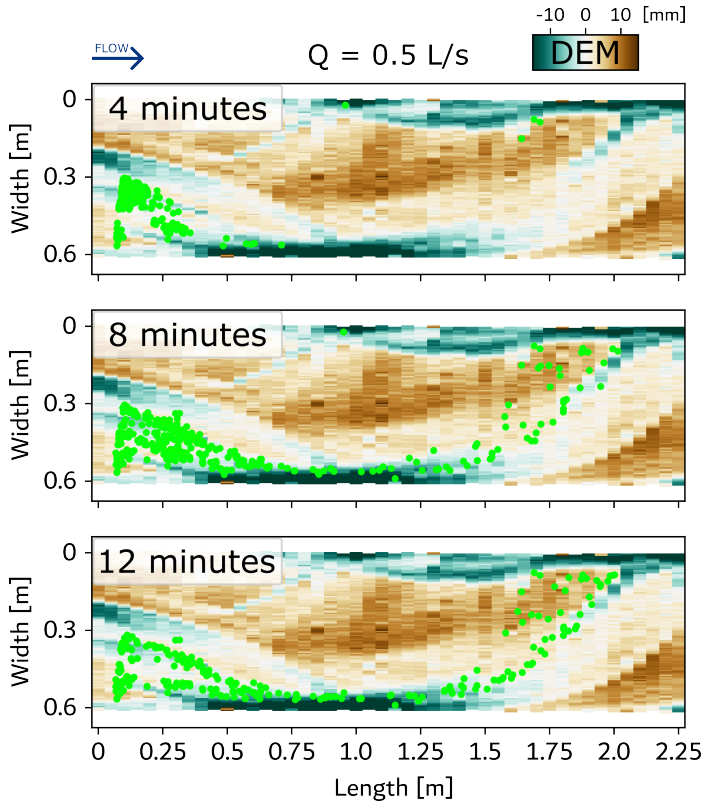

Figure 35 – Tracer displacements a 4, 8, and 12 minutes for the Q = 0.5 L/s run over the DEM.

As an example, we report the tracer displacement at three different time instants for three different discharge runs. In Figure 35 tracer displacements at 4, 8, and 12 minutes from the run start are presented for the Q = 0.5 L/s run. The tracers, placed in an active channel, moved downstream following the trajectory of the channel to the right. Towards the end of the run, many stopped in the shallow area outside the curve on the left. In Figure 36 tracer displacements are presented for the same instants for the Q = 0.7 L/s run. In this case, two active channels were identified and two separate tracer strips were placed. Due to the presence of a confluence downstream, the tracers followed a convergent trajectory and stopped approximately one metre from the feeding point. In Figure 37 tracer displacements are presented for the same instants for the Q = 1.0 L/s run. In this case, the tracers placed in the active channel scattered downstream of the feeding point and stopped in a large area at a higher elevation than the channel, travelling up to 2 m from the feeding point.

Within this chapter, we will use a single run as an example on which we will present the analyses performed. The results will then be presented in aggregate form for the different flow rate values.

5.3.1 Tracer position and DEMs-DoDs coupling

An example of the data obtained from the experiments and the overlap with the DEM and DoD is presented in Figure 38, where the position of the tracers in relation to the

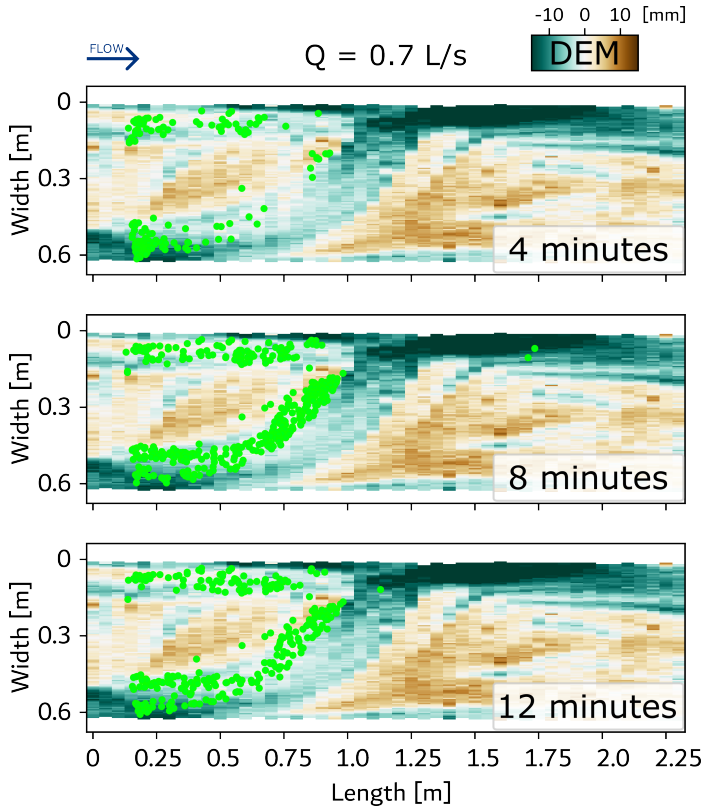

Figure 36 – Tracer displacements a 4, 8, and 12 minutes for the Q = 0.7 L/s run over the DEM.

topographical data for the run number 7 at discharge Q = 0.7 L/s is presented at the last instant of the run. The position of the tracers is put in relationship with the morphological component to answering the first research question. For each image of the time-lapse the number of detected tracers is computed to monitor the number of tracers in the survey domain.

In Figure 39 the evolution in the number of tracers that are detected in the channel domain (green curve) for the run number 7 at flow rate Q = 0.7 L/s is presented. Moreover, the number of tracers is divided depending on their position in the DoD.. Thus, it is possible to track the number of tracers that belongs to scour area (red), fill area (blue), and no-change area (gray). As presented in section 2.6, the initial position of the tracers is derived from the first photograph of the survey. This is used as a mask for subsequent images. In fact, in Figure 39, only the tracers that have moved downstream from their initial position are shown. After the initial start-up phase, the number of tracers in fill positions increases rapidly until it reaches a peak zone around 175 tracers. The number of tracers in scour zones remains relatively lower and does not exceed 25 tracers. The same applies to the number of tracers in areas considered to be no-change. The total number of tracers (green curve) reached the maximum value of approximately 200 tracers starts to gradually decrease, showing that an increasing component of tracers has left the analysis domain. For this reason, the following analyses are conducted over a time window from the time when the flow rate reached steady state to the time when the tracers present were greater than 75% of the maximum reached, i.e. over a time period of 8 minutes.

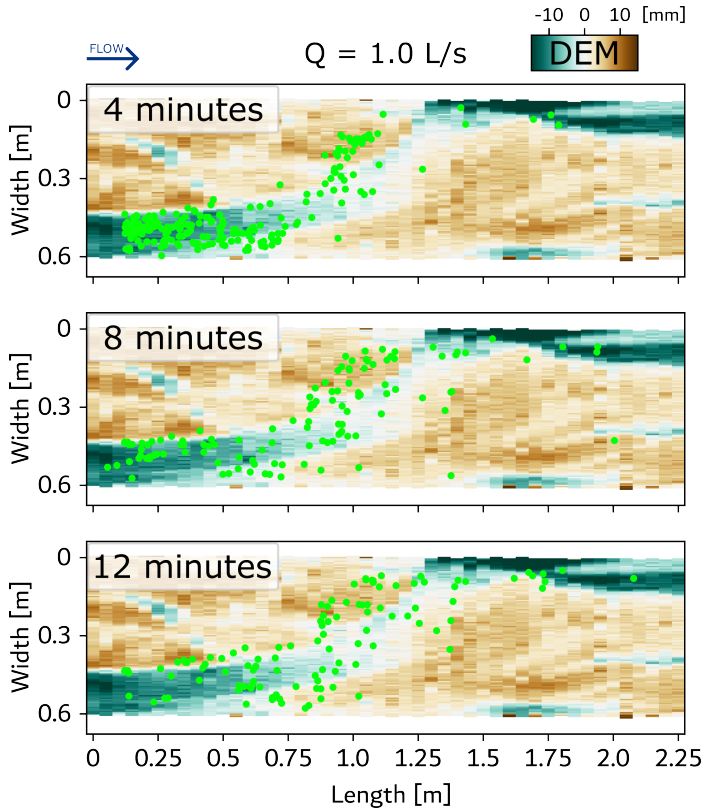

Figure 37 – Tracer displacements a 4, 8, and 12 minutes for the Q = 1.0 L/s run over the DEM.

In Figure 40a we can see that, compared to the detrended DEM values, the tracers tend to be located at lower elevations with a peak around -15 mm. In Figure 40b it can be seen that the majority of tracers are located in areas of deposition, up to 15 millimetres above the DoD filtering threshold, and areas where morphological changes are not measurable. Tracers in excavation zones show minimum values around -10 mm.

It is possible to extend the analyses made for individual runs by aggregating all data for each discharge. In this way, the effect of discharge on tracer displacement can be assessed. In particular, we will evaluate the effect of discharge on tracer displacement both in terms of elevation and in terms of morphological dynamics.

In Figure 41 the distributions of DEM and DoD values for all available runs at different discharge are presented.

In Figure 41a, the elevation values of the DoD points at which tracers are found are presented. The average values are, for all three discharges, close to zero. A slight discharge effect is visible in the increase of the mean value and the upper end of the elevations as the discharge increases. There is also an increase in variability with increasing discharge as shown by the box-plot whiskers.

In Figure 41b, the proportion of total tracers belonging to areas of scour, no-change, or fill is presented. The graph shows that the average proportion of tracers present in fill areas remains almost unchanged as the flow rate varies, and is around 30%. There are more tracers present in fill zones than in scour zones. The average proportion of the total number of tracers in scour zones varies from 6% for flow rate Q = 0.7 L/s to 20%

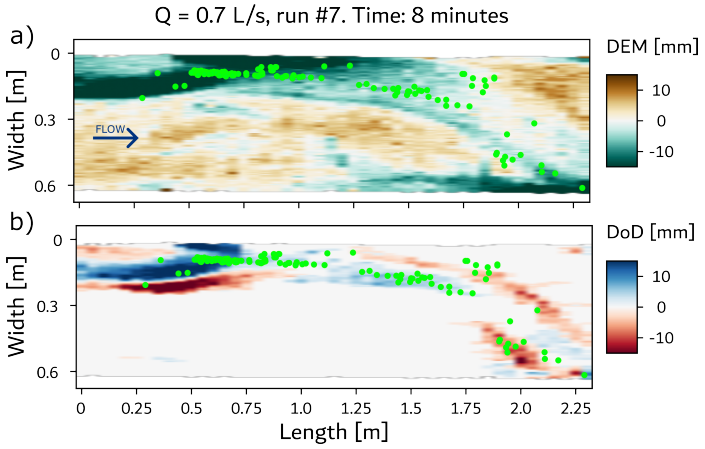

Figure 38 – Example of tracer overlapping with respect to DEM (a) and DoD (b). The tracers are indicated by green dots. The position is relative to the last available frame, after a 8-minute run. The length of the analysis domain is given by the size of the wooden frame holding the UV LED stripes.

for flow rate Q = 0.7 L/s and then reaches 16% for flow rate Q = 1.0 L/s. For the three tested reaches, the highest average proportion of tracers in the total was attributable to areas where no morphological variation could be measured. In general, there is a reduction in the variability of the data as the discharge increases, except for the proportion of tracers in scour zones.

5.3.2 Tracers distribution

By counting the number of tracers along the transverse axis of the channel, a longitudinal distribution of the number of tracers per frame can be obtained. This allows us to monitor the progress of the tracers stream-wise.

To explain the tracers displacement, in Figure 42 the longitudinal distribution of the tracers is presented as an example. In this example, tracers move downstream for a short distance (300 mm) and they stop. Some of them pass over and stop from 1000 mm to 2000 mm. With the passage of time, the peak of the most upstream distribution remains more or less unchanged in terms of position, while a peak strengthens downstream at the 1500 mm position. In runs where distinct peaks can be seen, these tend to stabilise in terms of position after an initial phase.

With the purpose of answering the second research question, in this section we will investigate the tracers distribution along the longitudinal coordinate. In particular, we investigated the presence of sediment accumulation zones and the location, where present, of the mode distributions.

We decided to implement the Gaussian Mixture Model (GMM), a probabilistic approach to clustering and modelling data, widely employed in scenarios where the underlying distribution consists of multiple overlapping subpopulations. GMM assumes that the data can be represented as a weighted sum of Gaussian distributions, each characterized by its own mean, variance, and weight. This technique is particularly effective in identifying

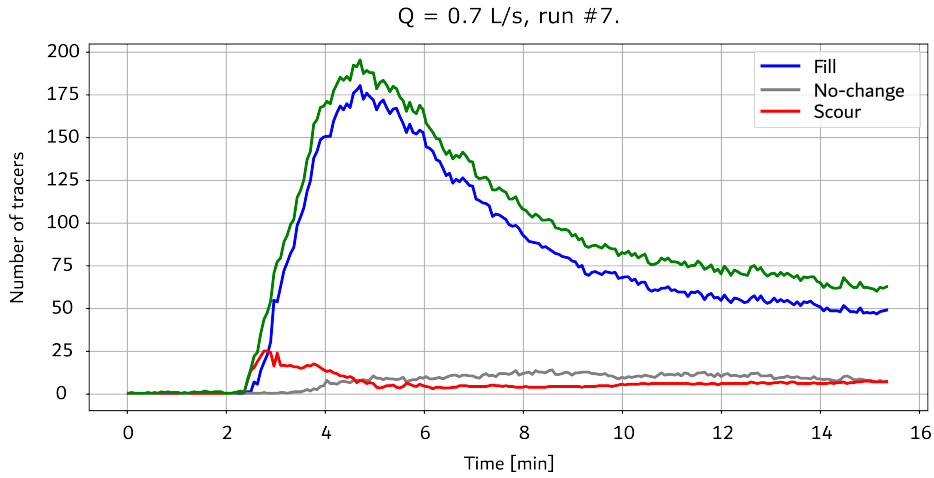

Figure 39 – Number of tracers in scour, fill and no-change areas over time. The chart is referred to the run number 7 with discharge Q = 0.7 L/s. The temporal discretization is 4 seconds.

subgroups within a dataset where the boundaries are not clearly defined. Here, the GMM model is used to derive the mode of tracer distributions along the longitudinal axis. The use of the GMM technique occurred following a literature search on how to distinguish different distributions within a population of data. The optimal conditions for applicability are stringent but, as far as application to our data is concerned, the GMM results were qualitatively screened and only distributions were selected for which there was the distinct presence of two modes with a sufficient number of tracers for each mode. The application of this method can be observed in Figure 43 for the example run. In Figure 43a, the normalised frequency distribution of the longitudinal coordinates of the tracers after 8 minutes is shown. In Figure 43b, the total distribution of tracers is divided according to the GMM model into two distinct modes. This made it possible to assess how many modes were present for each run and the longitudinal coordinate of the median of the modes thus obtained.

In the example shown in Figure 44, it is possible to observe the longitudinal co-ordinate with respect to the feeding position of the position of the modes (solid lines) referring to the left y-axis, and the trend in the number of tracers (dashed lines) belonging to each mode, referring to the right y-axis.

In Figure 44 Mode A is the one closest to the feeding point and is characterized by the greatest number of tracers. The longitudinal coordinate changes from 200 mm to 400 mm. Mode B is characterized by a longitudinal coordinate that increases in the first phase of the test. At the end of the test it reaches 1200 mm. The number of tracers in this mode is constant and around 75 tracers. In most cases, the position of the fashions remains almost constant over time. Instead, the number of tracers constituting it varies, as observed in Figure 42 where an exchange of tracers between upstream and downstream fashions is observed. After a short settling phase, the position of the two modes with respect to the feeding point remains constant.

In Table 5 is presented the percentage, over the total number of runs, of cases in those 2 modes are detected and 2 separate branches are exploit to conduct the experiment.

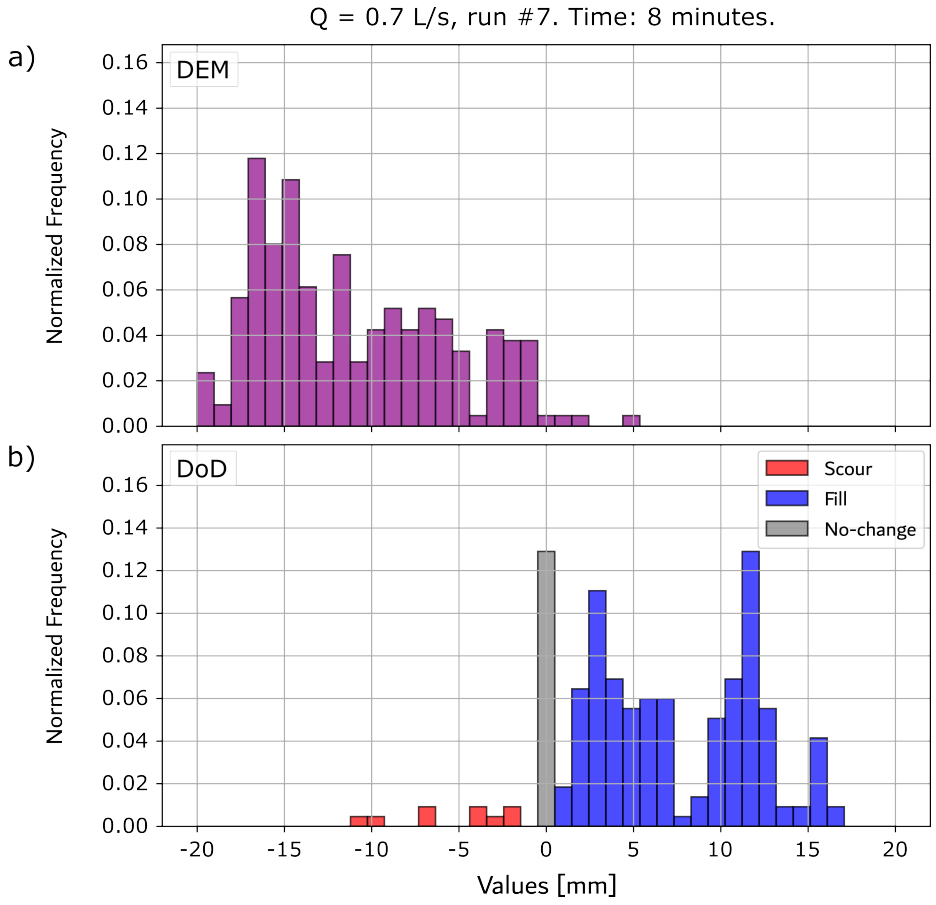

Figure 40 – Distribution of DEM (a) and DoD (b) values of the totality of tracers in the channel domain. The chart is referred to the run number 7 with discharge Q = 0.7 L/s.

5.3.3 Distance between modes and fill area

As noted above, looking at the distributions of tracers along the longitudinal co-ordinate it is possible to identify areas where tracers tend to accumulate. In 75% of cases, in fact, two distinct fashions can be observed. Moreover, the position of the modes remains stable over time. In some cases, after an initial growth phase, the number of tracers in the more upstream mode tends to decrease, while the number of tracers in the more downstream mode increases. Moreover, as already mentioned, the position of these fashions remains stable over time.

It is therefore interesting to assess what the distance between the fashions is and what the discharge effect is. In this section, the relationship between the distance between the

Table 5 – Number and percentage of runs that exhibit two modes and runs where two branches are present.

	2 modes	2 branches
Number of runs	27	10
Percentage over total	75%	28%

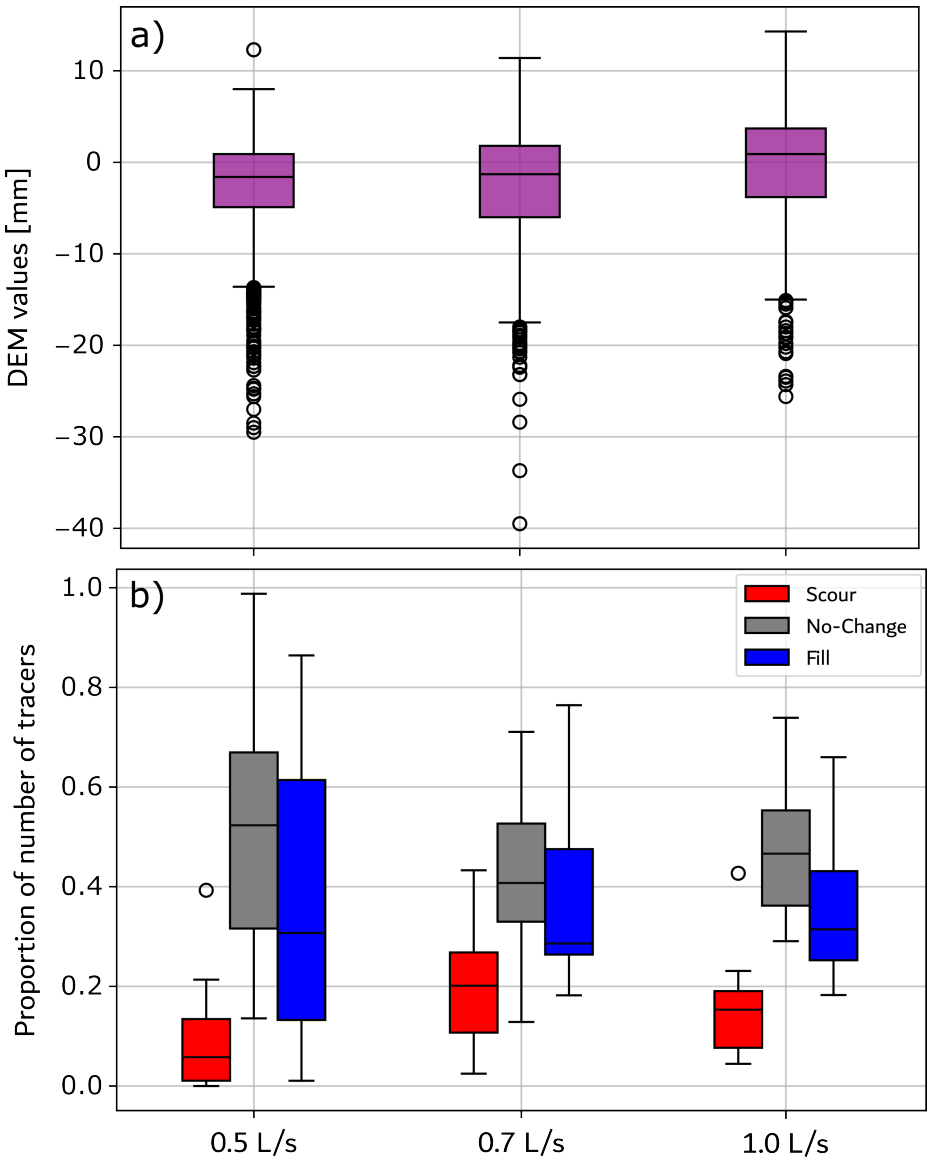

Figure 41 – Caption.

modes of the distribution (following the application of GMM) and the distance between the main deposition zones is investigated. The relative distance between two modes can be calculated as the difference in terms of the longitudinal coordinate of the two modes. The distance between modes is calculated by considering the last available time instant.As the analysis window is assessed, the last instant is characterised by the stable position of the two modes.

In Figure 46 a the distance between the modes is presented for different discharge values. As the discharge increases, the distance between modes decreases from 1150 mm for Q =0.5 L/s , to 800 mm for Q = 0.7 L/s, to 700 mm for Q = 1.0 L/s.

In cases where obvious modes can be seen, an influence of morphology is likely. In fact, tracers stop on bars and generally deposit zones. It is therefore interesting to assess the distance between the deposition zones in order to compare it with the distance between

the modes of the distributions.

Fill areas, are evaluated by working on the DoD. Specifically, the number of cells that are characterized by fill are counted for each section. The number of fill cells for each DoD cross section is reported in Figure 45c.

The signal of the number of fill cell is then filtered with a Savitzky-Golay filter to reduce any spikes (dashed curve). The Savitzky-Golay filter (Savitzky and Golay, 1964) was applied to smooth noisy data while preserving the peaks features, ensuring minimal distortion of the signal characteristics. For peak detection, the `find_peaks` algorithm from SciPy (Heinzel et al., 2002) was employed, enabling the identification of prominent topographic features based on their prominence and spatial distribution.

In Figure 46a distance between the deposition areas can be observed for each discharge. As the flow rate increases, the distance between the main storage areas decreases, which averages around 1500 millimeters for Q = 0.5 L/s, 950 mm for Q = 0.7 L/s and 750 mm for Q = 1.0 L/s. The data variability slightly decreases as the discharge increases. Figure 46 collected the results of the analysis related to the distance between tracer distribution modes and the distance between the main deposition areas. In Figure 46 the two graphs show similar values, especially for higher discharge. Both metrics show a similar trend as flow rate increases although the distance between modes generally shows less and more constant variability.

5.3.4 The effect of discharge on tracer displacement

With the intention of answering the third research question, in this section we will evaluate the distance tracers travel along the longitudinal axis of the laboratory flume and we will compute a mean tracer velocity. The travelled distance was calculated as the distance between the feeding area and the midpoint of the longitudinal coordinates of all tracers present at the last time instant. In fact, the distance between the midpoint of the longitudinal coordinates of all tracers tends to increase over time although the distance between modes is fairly constant. This is due to the fact that although the tracers are positioned on two distinct modes (when present), the number of tracers belonging to the downstream mode tends to increase by shifting the midpoint of the longitudinal tracer positions downstream. The time interval considered for calculating the distance travelled was evaluated with the intention of measuring the average displacement of the totality of the tracers, thus also considering periods when the tracers were partially stationary. The mean distance travelled by the tracer (Figure 47) shows a clear effect of discharge. The average values ranges from 450 mm for discharge Q =0.5 L/s, to 600 mm for discharge Q = 0.7 L/s, to 720 mm for discharge Q = 1.0 L/s. The runs at discharge Q = 0.7 L/s show the greatest variability while the runs at discharge Q = 0.5 L/s and 1.0 L/s show similar variability.

Tracers virtual velocity

By dividing the average distance travelled by the tracers by the duration of the time interval in which this was evaluated, the average speed of the tracer population can be calculated considering both periods of movement and periods of episodic rest ()Einstein, 1936; Ferguson and Wathen, 1998; Liébault et al., 2012. In Figure 48 are presented the average

velocity values expressed in millimeters per second. The velocity values show a strong dependence on the flow rate values. In fact, as the flow rate increases, the velocity values increase, exhibiting average values of 1 mm/s for Q = 0.5 L/s, 3 mm/s for Q = 0.7 L/s, and 3.5 mm/s for Q = 1.0 L/s. The Q =0.7 L/s discharge run, although with greater variability, presents an average value of 3 m/s that is very similar to the Q = 1.0 L/s discharge.

5.4 Discussion

In this chapter, we studied the tracer displacement of fluorescent tracers in a laboratory flume. The intention is to evaluate the effects of morphology on transport dynamics in three different cases of constant discharge. The dataset used is of great value as it collects information on tracer displacement every 4 seconds and couples information from the DoD and DEM Figure 38.

Experimental observations clearly demonstrate the strong conditioning of the distances travelled by tracers and their associated morphology. Indeed, an analysis of the tracer distributions reveals predominantly bimodal patterns in the runs where tracers travelled across the entire analysis domain. subsection 5.3.3 suggests that the distance between the modes is linked to the primary depositional zones, which are shaped by the morphological features, as proposed by R. S. Pyrce and Ashmore, 2003. In fact, the distance distributions between the modes of the bimodal distributions (Figure 46b) and the distances between depositional areas (Figure 46a) exhibit a clear correlation.

As shown in Figure 44 and Figure 45 clear multimodal trend is observed, driven by depositional zones. As hypothesized by Hassan et al., 1992, these zones appear to "trap" sediments. Additional confirmation of this observation comes from the fact that during different experiments, the depositional areas of the tracers coincide. Upon further analysis of the distances between depositional areas in the DoD and the distance between modes as a function of flow rate (Figure 46), it becomes apparent that, as the flow rate increases, the distance between depositional areas tends to decrease. This trend is likely linked to changes in the active channel width. Specifically, as the flow rate increases, both the wetted width and active width of the channel change, with many secondary channels becoming inactive at a flow rate of 0.5 l/s. The variation in the active channel width, particularly in a channel with the same morphology as the one studied, suggests that, at flow rates lower than those at which the channel was formed, certain morphological features—and their potential to act as sediment "traps"—are not activated, resulting in an increased distance between depositional areas.

In the work of McDowell et al., 2021, the final positions of tracers generally coincide with depositional areas. This result, anticipated by Ashmore and Church, 1998, was later observed in the laboratory by Kasprak et al., 2015; R. S. Pyrce and Ashmore, 2005. In particular, Kasprak et al., 2015 observed how most of the tracers were detected in areas of often slight (less than 2 mm) deposition. However, in this study, it is observed that tracers were primarily detected in areas that later proved to be under the filtering threshold and depositional areas. This implies that the tracer paths are constrained, with this constraint being dictated by the morphology. Additionally, the modes within the distributions remain relatively constant over the run period considered Figure 44, suggesting that while the

tracer cloud generally moves downstream, individual tracers predominantly jump from one depositional area to another.

The high recovery rate ensured by the fluorescent and paramagnetic tracers is very high if compared with field studies that involve passive tracers. The work of Vázquez-Tarrío and Batalla, 2019 provides a collection of 30 datasets where the main parameters of tracer displacement are collected, with a recovery rate of 50% on average. In Lamarre and Roy, 2008 and Milan, 2013 the relationship between travel distance and the bed morphology is quite clear in step-pool and pool-riffle morphology, while for large gravel bed rivers, this is still unclear. This is probably due to the spatial complexity of depositional patterns, where a clear succession of cross-sectional accumulation areas are difficult to obtain. Vázquez-Tarrío and Batalla, 2019 studied the effects of lower than the formative discharge in tracer displacement. The Authors argue that large boulders and gravel bars may slow down the sediment in their movement downstream. Macro-bed forms, indeed, can concentrate the current and the sediment flux into specific paths. This leads to a fester sediment delivery downstream. These results are in contrast to what we observed in our experiments. In fact, with the same morphology, as the discharge increases, the speed of the tracers moving downstream increases. This could be because the grain size is constant in our experiments and therefore slowdown effects are absent.

The results show a clear relationship between morphology and tracer displacement, in particular the relationship between mode distance and the distance between the main deposition areas. This result may suggest different ways of analysing tracer displacement and provide useful insights into bedload dynamics. Furthermore, the obtained results boost the implementation of the morphological method according to step-length-based approaches.

Assessing the correspondence between the position of the main deposition areas and the position of the tracers can provide useful information on the dynamics of bedload transport. In fact, it is possible to observe how tracers are transported and tend to be deposited mainly in the erosion or equilibrium bedload areas. In these terms, morphological dynamics play a key role and thus there is a strong correlation between morphology and transport dynamics as expected given the formulation of the morphodynamic problem. Step-length-based approaches can therefore provide important information on sediment dynamics and thus can lead to an informed design of survey campaigns. For example, placing tracers immediately upstream of a large deposit area may not provide useful results. For the same reason, the search for tracers can be directed to the main deposit areas avoiding unnecessary time speculation. However, these methods do not provide any information on the mass flow, for which it is necessary to know the distance travelled by the tracers and the time during which they were in motion. Furthermore, it is important to point out that the study of tracer displacement is subject to a strong assumption, namely that tracer displacement is representative of the entire sediment population, both in terms of grain size and entrainment.

The path-length estimate from the DoD was compared with some field data (McQueen et al., 2021) in terms of tracer displacement and the relationship between the location of DoDs and the morphological dynamics taking place along the San Juan River. The analyses are reported in Capito, Pandrin, et al., 2024. Field data show a strong correlation between tracer displacement and ongoing morphological dynamicsh. Most of the tracers employed do not exceed the first large erosion zone they encounter from the feeding point durate a year with moderate flow.

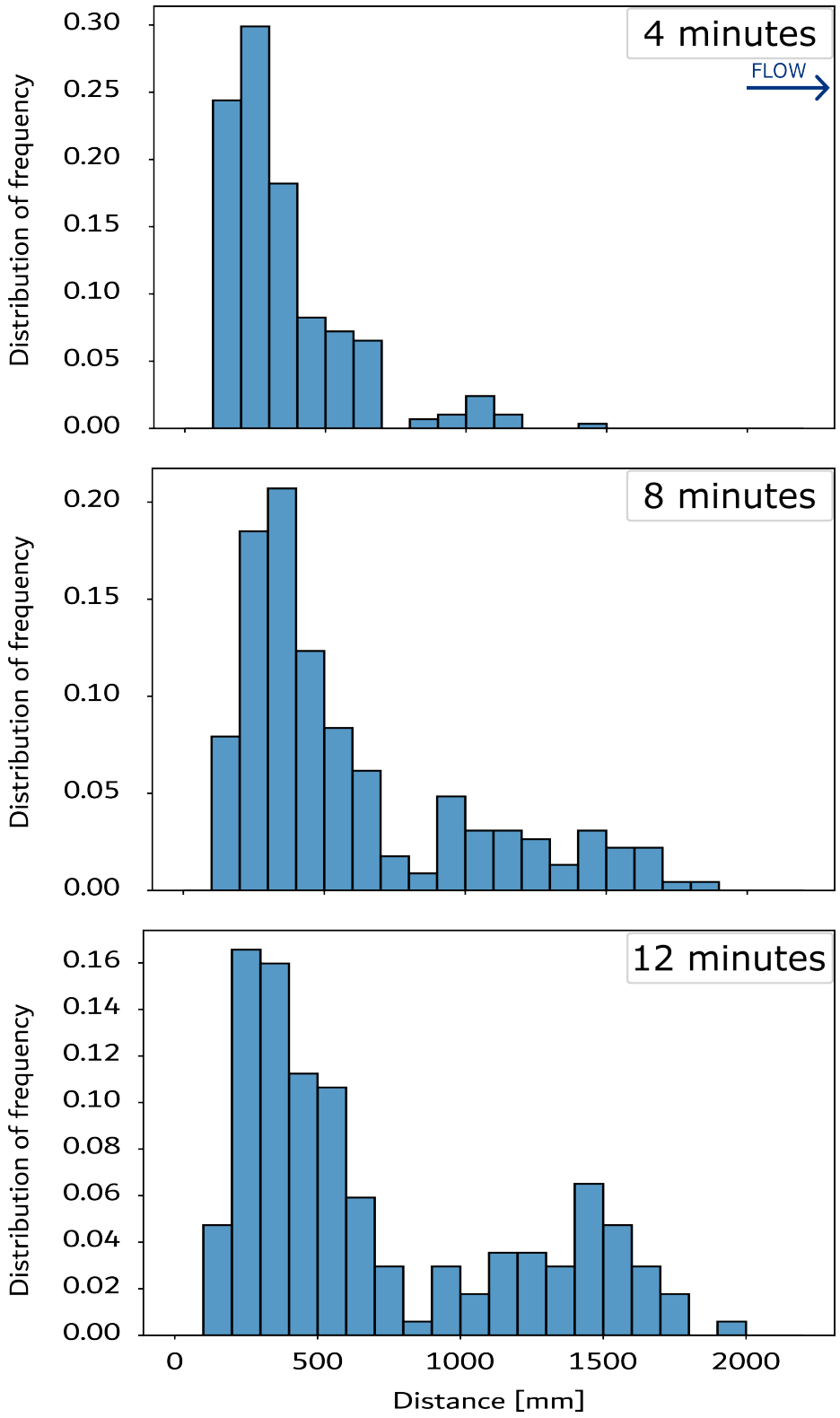

Figure 42 – Longitudinal distribution of the number of tracers at 4, 8, and 12 minutes for discharge Q = 0.7 L/s run.

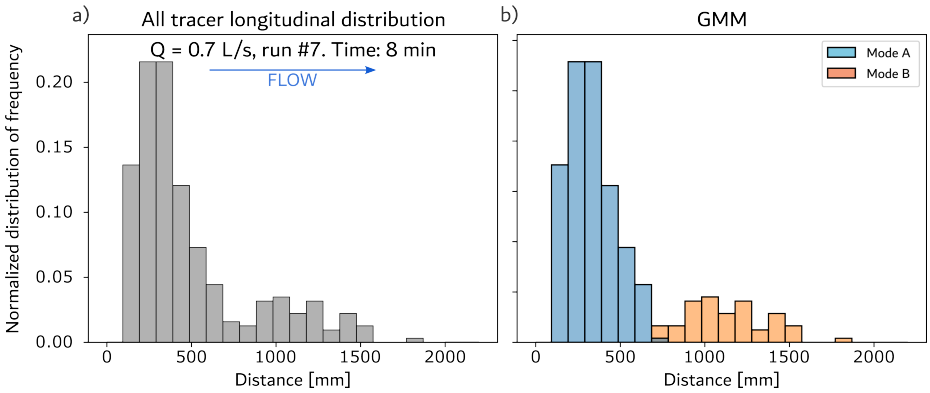

Figure 43 – Normalized distribution of frequency (a) and modes identification with GMM method (b) for the run number 7 with discharge Q = 0.7 L/s.

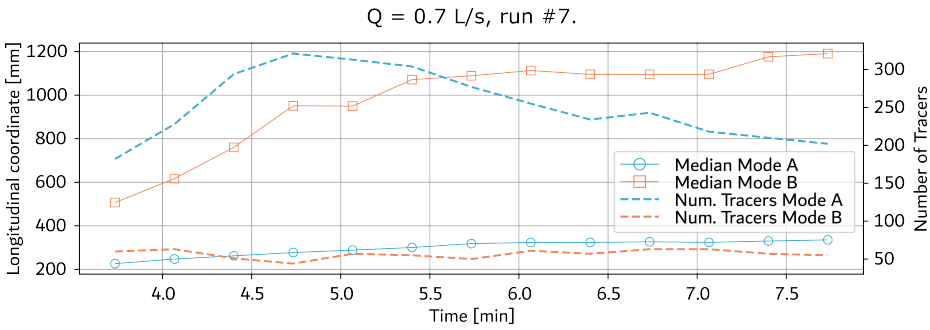

Figure 44 – Modes position along the longitudinal coordinate and number of tracers belonging for each mode over time for the run number 7 with discharge Q = 0.7 L/s

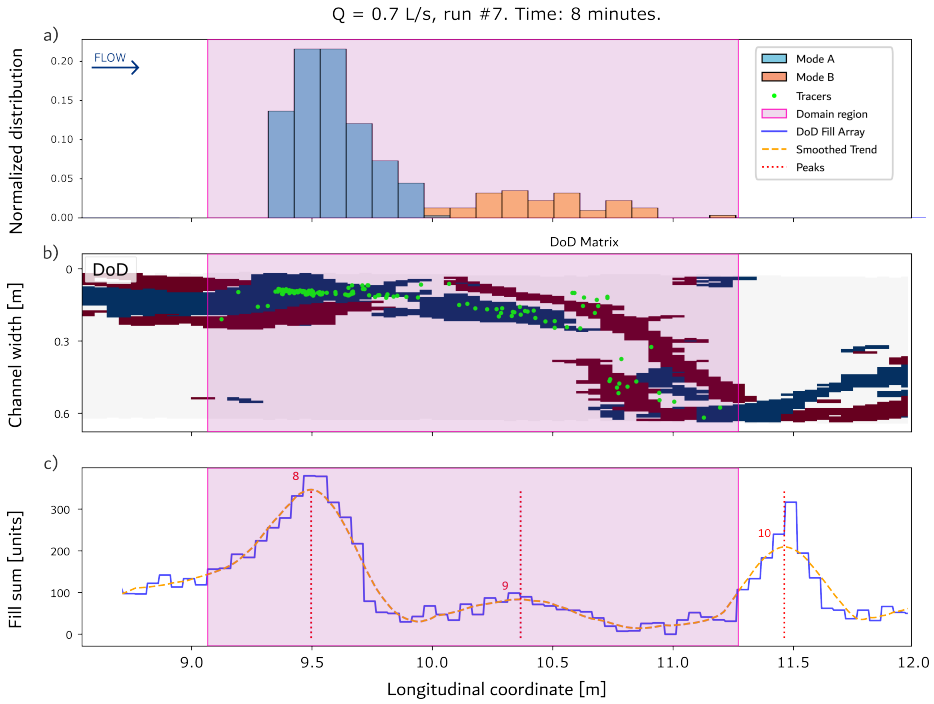

Figure 45 – Tracers distribution along the longitudinal coordinate divided accordingly with the GMM algorithm (a), DoD and tracer displacement overlapping (b), number of fill cell for each cross-section and peak identification (c). Water flows from left to right.

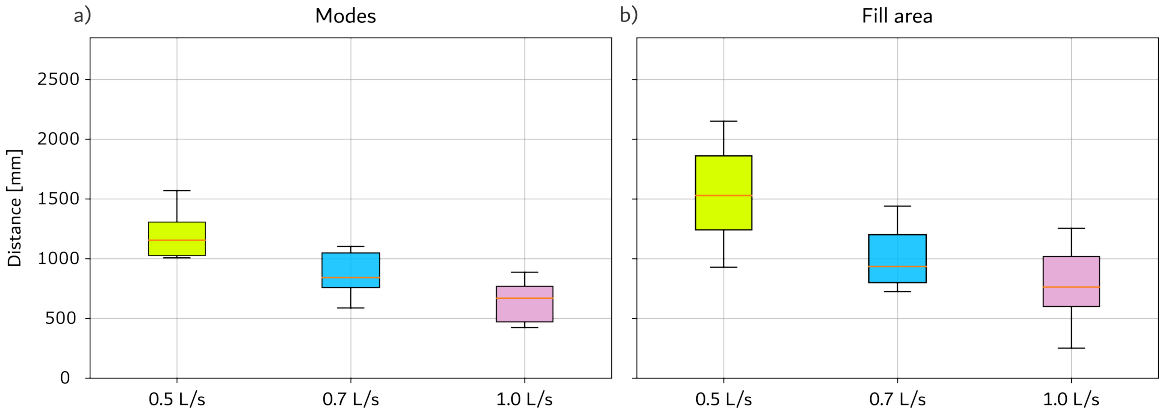

Figure 46 – For each discharge the distance along the longitudinal coordinate of fill areas (a) and modes (b) is presented.

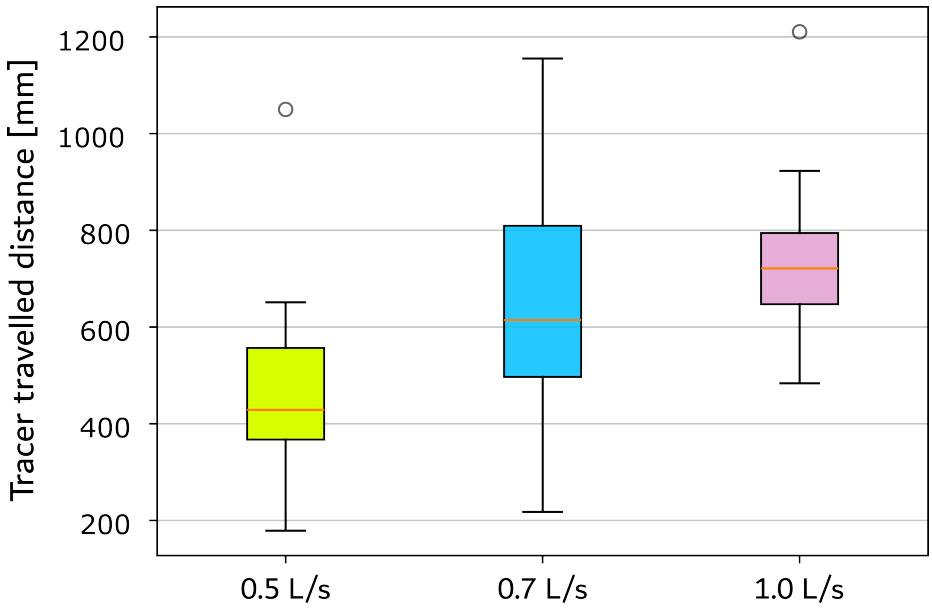

Figure 47 – Travelled distance from the feeding position and the midpoint of the tracers displaced in the channel domain. Results are divided by the flowing discharge.

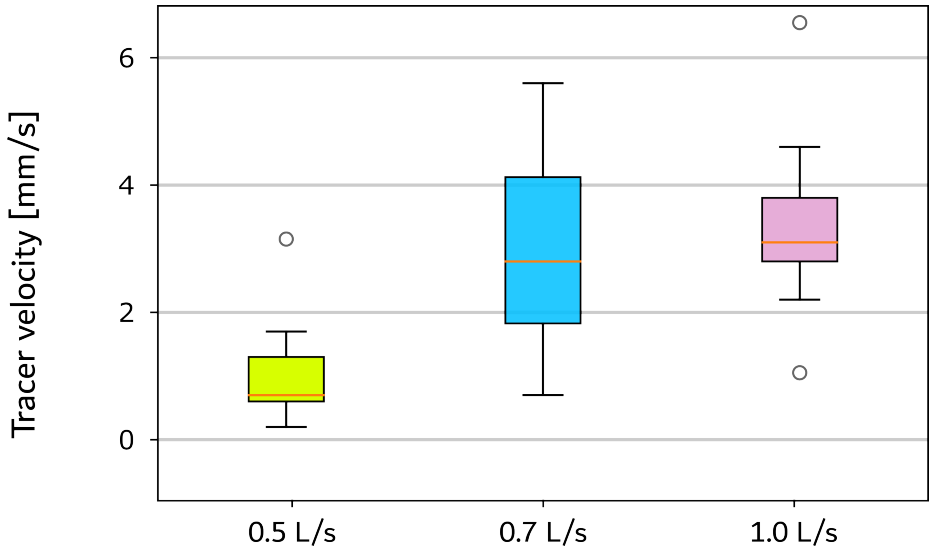

Figure 48 – Tracers virtual velocity computed as the mean travelling distance divided by the duration of the time interval in which tracer displacement is evaluated. Results are presented for the three flowing discharges.

CHAPTER 6
BEDLOAD ESTIMATION

6.1 Introduction

As explained in chapter 1, the inverse method (Ashmore and Church, 1998; Vericat et al., 2017) in the formulation based on Exner's equation provides the bedload variation over space, looking at the morphological changes over time. Once a known sediment flux through a certain cross-section is given, the sediment budgeting approach can be applied, and the morphological method provides the spatial distribution of bedload by integrating Equation 12. This approach can be applied in various time scales, from the event scale to the multi-event time scale. The sediment budgeting approach provides the bedload spatial distribution considering the morphological changes measured over time, and assumes that the known sediment flux at a given cross section is a good estimation of the sediment transport. The sediment budgeting approach derives the spatial distribution of the morphological bedload since the spatial distribution is based on the DoDs. This introduces This introduces limitations that is important to take into account: although a known sediment flux cross section is available, the spatial distribution of bedload is related to morphological bedload only. The known sediment flux incorporates the non-morphological bedload as well, which shows a considerable intensity and extension as presented in the previous chapters. So, the known and comprehensive sediment flux simply shifts the spatial variation of the morphological bedload upward but does not represent the spatial variation of the whole sediment transport. Anyway, the sediment budgeting approach is useful to obtain information about the catchment evolution in terms of sediment and bedload dynamics, and channel stability.

When it is not possible to incorporate a zero-flux section into the domain boundaries, the study of particle displacement can provide useful information on the sediment path length and then the virtual velocity. Coupling this information with the volume of eroded sediment, we can estimate the sediment flux using Equation 10. This method assumes that the eroded sediment computed by a DoD can be used as a proxy for the moved (or entrained) sediment during a certain event. Moreover, it assumes that the travelled distance measured using the tracers is representative of the entire entrained sediment population during the considered event, and that it is possible to define, once the sediment is entrained, how much time it takes to stop. In this way, a sediment flux can be computed.

In this paragraph, the virtual velocity (which is one of the main ingredients of this approach) is discussed. If we consider a simplified condition where a rectangular-shaped river section experienced bedload, the virtual velocity of sediment moving downstream should be constant over time. The discharge is constant, and so is the transport capacity. The reach is in a near equilibrium state where the sediment at the inlet is the same as the sediment at the outlet, but morphological changes occur due to the spatial variability of the sediment transport. Given a constant and known bedload flux (see Equation 10), we obtain that the virtual velocity estimation depends on the volume of eroded sediment as follows:

$$v_b = \frac{Q_S L_C}{\sum V_e (1-p) \rho_S} \tag{28}$$

Increasing the observation time and excluding compensatory effects, the eroded volume tends to increase and so does the virtual velocity of sediment. This revealed ambiguity is because at the basis of the virtual velocity approach formulated by Equation 10 lies that the time interval over which the virtual velocity and the eroded sediment have to be the same.

Thus, we propose a slightly different approach that involves the step length and morphological metrics as well. An estimation of the sediment flux can be obtained by considering the specific volumetric flux multiplied by the sediment step-length, following the formulation:

$$Q_s = \frac{\sum V_e}{\Delta T \times L_c} \times P_L \tag{29}$$

where $\sum V_e$ is the eroded volume computed from DoD at timespan ΔT, L_c is the survey streamwise length and P_L is the sediment path length. In this case, L_c has to be greater than the path length and long enough to result in morphological metrics stability as shown in chapter 3. This revisited method lies in the idea that the volume of eroded sediment can be computed from DoDs for which the epochs of surveying are known. Moreover, this avoids the time dependency shown in Equation 10 where increasing the timespan between surveys probably means increasing the volume of eroded material. Later on, in this chapter, we will apply this formulation to compare the measured bedload at the flume outlet with the sediment flux estimated with Equation 29.

Compensation processes, where a switch between scour and fill processes occurs in the same place between two consecutive topographic surveys, can negatively affects the estimation of morphological changes (Lindsay and Ashmore, 2002; Vericat et al., 2017). Compensation effects can be estimated, and show a strong dependency with flow confinement and survey frequency, as highlighted in chapter 4. Compensation can negatively affect the estimation of morphological changes and thus the estimation of eroded volumes in the application of morphological methods using this metric. Even if the tracer's displacement would be representative of the entire sediment population, and so incorporate equilibrium bedload as well, the volume of eroded sediment would be still affected by compensation and travelling bedload.

6.2 Research questions

This chapter aims to address the following research questions:

- What is the effect of survey frequency in the morphological approach implementation?
- What is the reliability of bedload estimation using morphological-derived path length?

6.3 Methods

In this section, we will take advantage of the data presented in the previous chapters to answer the research questions. We will analyse the data from repeated topographic surveys presented in chapter 3 and investigate the role of survey frequency in estimating bedload flux through the implementation of the morphological method. As shown for the morphological active width (MAW), the proportion of the channel that exhibit morphological changes, we can compute the volume of eroded volume varying the survey frequency. As with the MAW, having a limited number of DEMs available, decreasing the survey frequency means removing more and more DEMs. This implies that the number of DoDs calculated goes from 9 for the highest temporal discretization to 1 for the coarsest. This consequently reduces the variability of the data.

The path length data were obtained from the work of Capito, Pandrin, et al., 2024 which is based on the same laboratory experiments presented in chapter 3 and chapter 4.

Capito, Pandrin, et al., 2024 analyzed fill areas patterns and through the implementation of a novel method in signal analysis, they extract a path length of sediment displacement. Path length data are available for Q = 0.7 L/s, Q = 1.0 L/s, Q = 1.5 L/s and Q = 2.0 L/s discharges and are computed from DoD at the finest discretization. Moreover, during the last 20 Exner time of the preparation run, bedload flux was measured without interruption at the channel outlet providing, for each discharge, a reliable measurement of Q_S.

Bedload flux is then computed using Equation 29. The volume of eroded sediment and step length variability are taken into account estimating the Q_S variability with the following formula

$$\sigma_{Q_S} = \frac{(1-p)\rho_S}{\Delta T L_C} \times \sqrt{\mu_{P_L}^2 \sigma_{V_E}^2 + \mu_{V_E}^2 \sigma_{P_L}^2 + \sigma_{V_E}^2 \sigma_{P_L}^2} \tag{30}$$

where V_e is the eroded volume computed from DoD at timespan ΔT, L_c is the survey streamwise length and P_L is the sediment path length. μ and ρ are mean value and standard deviation respectively.

It is possible to calculate Q_S, and the associated estimate of the standard deviation, by varying the survey frequency. In fact, it is sufficient to update the values of V_E and ΔT relative to the survey frequency analysed.

Knowing the bedload flux it is possible to estimate the expected path-length reversing Equation 10 that turns into:

$$P_L = \frac{Qs \Delta T L_C}{\sum V_E (1-p)\rho_S} \tag{31}$$

where Q_S is the measured bedload flux, V_e is the eroded volume computed from DoD at timespan ΔT, L_c is the survey streamwise length. p is porosity and ρ_S is sediment density. The standard deviation of the estimated P_L can be computed as following:

$$\sigma_{P_L} = \frac{\Delta T L_C}{(1-p)\rho_S} \frac{1}{|\mu_{V_E}|} \sqrt{{\sigma_{Q_S}}^2 + \frac{{\mu_{Q_S}}^2 * {\sigma_{V_E}}^2}{\mu_{V_E}^2}} \tag{32}$$

where μ and ρ are mean value and standard deviation respectively.

Table 6 – Volume error estimated comparing the scour volume computed with a timespan of 4 Exner time and and cumulative volume after the same time.

Discharge [L/s]	Volume underestimation
0.5	-55 %
0.7	-55 %
1.0	-71%
1.5	-68%
2.0	-69%

6.4 Results

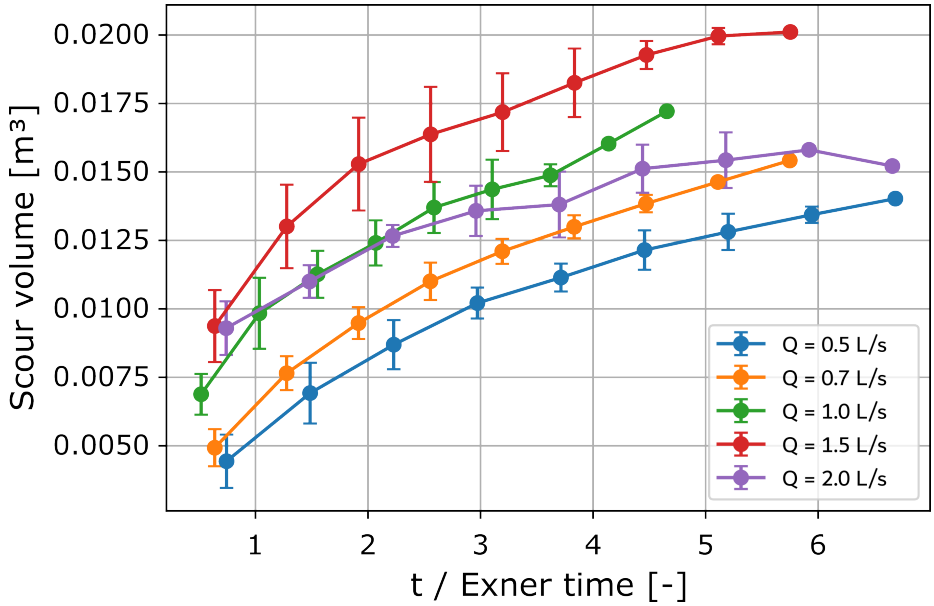

Figure 49 – Scour volume in cubic meters computed varying survey frequency. Dots represent mean values and whiskers represent data variability. Data are presented for Q = 0.5 L/s, Q = 0.7 L/s, Q = 1.0 L/s, Q = 1.5 L/s, and Q = 2.0 L/s discharge.

In Figure 49, the volume eroded during the different run is presented varying the survey frequency. Dots represent mean values and whiskers are one standard deviation of data variability. Values ranges from 0.004 m^3 to 0.014 m^3 for the Q = 0.5 L/s discharge, and from 0.09 m^3 to 0.02 m^3 for the Q = 1.5 L/s discharge. The latter shows the highest values. In general, increasing the discharge the volume increases. One exception is the Q = 2.0 L/s discharge that shows starting values close to the Q = 1.5 L/s discharge and ends close to the Q = 0.5 L/s discharge values. In general, the scour volume tends to double its value over 5 Exner time.

By comparing the volume calculated by decreasing the survey frequency with that calculated by cumulatively summing up the eroded volume at the maximum temporal discretization, it is possible to obtain an estimate of the effect of compensation on the volume estimation (Figure 50).

Table 7 – Values of path length from Capito, Pandrin, et al., 2024, measured bedload flux at the channel outlet, estimated bedload flux using Equation 29, and error between measured and estimated bedload flux.

Discharge [L/s]	Path length [mm]		Measured Qs [g/s]		Estimated Qs [g/s		Error
	μ	σ	μ	σ	μ	σ	
0.7	1320	585	0.33	0.18	0.28	0.13	-14%
1.0	1460	178	0.78	0.3	0.83	0.13	+7%
1.5	860	800	2.39	0.7	0.87	0.82	-56%
2.0	930	496	3.34	0.98	1.20	0.65	-63%

In Table 6, the relative error is presented at 4 t / Exner time. Volume underestimation shows values that range from -55.24% for Q = 0.5 L/s discharge to -69.06% for Q = 2.0 L/s discharge, with an increasing underestimation increasing the discharge.

6.5 Bedload estimation

In Figure 51 the estimated bedload values are presented varying survey frequency. Dots represent mean values and whiskers are one standard deviation of data variability. The bedload flux is estimated using Equation 29. Step length values from Capito, Pandrin, et al., 2024 and measured sediment flux at the channel outlet are presented for the available discharge in Table 7 with mean values and standard deviation. Volumes of eroded sediment computed varying the survey frequency are presented in Figure 49. Path length data are available for Q = 0.7 L/s, Q = 1.0 L/s, Q = 1.0 L/s, and Q = 2.0 L/s. Path length mean values ranges from 930 mm to 1460 mm with no significant trend with discharge. Path length is estimated both considering the whole DoD and considering scour and fill separately. For each discharge, a mean and standard deviation value is used to compute the sediment flux. Measured bedload flux at the channel outlet shows values that range from 0.33 g/s for Q = 0.7 L/s discharge to 3.34 g/s for Q = 2.0 L/s discharge. Estimated values using Equation 29 range from 0.28 g/s for Q = 0.5 L/s discharge and 1.20 g/s for Q = 2.0 L/s discharge. Error is computed as following:

$$error = \frac{Q_{S,measured} - Q_{S,estimated}}{Q_{S,measured}} \tag{33}$$

For Q = 0.7 L/s shows -14% of relative error, Q = 1.0 L/s shows +7% of relative error, Q = 1.5 L/s shows -56% of relative error, and Q = 2.0 L/s shows -63% of relative error. For Q = 0.7 L/s and Q = 1.0 L/s the relative error is lower than 15%. Rather, Q = 1.5 L/s and Q = 2.0 L/s shows relative error close to -60/

In Figure 51 bedload estimation using Equation 29 varying the survey frequency is presented for all the available discharges. Dots represent mean values and whiskers are one standard deviation of data variability. Varying the survey frequency, bedload flux estimation tents to decrease for all the discharges (Figure 51). The Q = 0.7 L/s discharge run degreases from 0.28 g/s to 0.1 g/s, the Q = 1.0 L/s discharge decreases from 0.83 g/s to 0.23 g/s, the Q = 1.5 L/s discharge decreases from 0.87 g/s to 0.21 g/s and the Q = 2.0 L/s

discharge decreases from 1.20 g/s to 0.21 g/s. As the flow rate increases, the decrease in estimated bedload flux is more abrupt, showing a clear effect of discharge in the decreasing trend.

In Figure 52, the bedload flux is estimated varying the survey frequency. Dots represent mean values and whiskers are one standard deviation of data variability. The path length used in the computation is reported in Table 7. The volume of eroded sediment used in the computation is the cumulative sum of the volume eroded in each run at the finest time discretization (blue line in Figure 50). The bedload flux estimated shows values that remain almost constant varying survey frequency. Data variability increases increasing the discharge.

6.6 Path length estimation

In this paragraph we investigate the expected path length knowing the bedload flux and the eroded volume. This can be done using Equation 31.

In Figure 53 values of estimated path length are presented varying survey frequency in eroded volume computation from DoDs. Dots represent mean values and whiskers are one standard deviation of data variability. The bedload flux used in the computation the one measured at the channel outlet (Table 7). Decreasing the survey frequency, the path length increases from values that range from 1.5 m to 2.5 m for the finest discretization up to 4 m for the Q = 0.7 L/s discharge and 14 m for the Q = 2.0 L/s discharge. A clear discharge effect is present with higher estimated path length values that belong to the higher discharge value. Moreover, for higher discharges, the estimated path-length values increase more rapidly.

Value of the estimated path-length computed using the cumulative volume of single runs is presented in Figure 54. Dots represent mean values and whiskers are one standard deviation of data variability. Estimated path length shows constant values that ranges from 1.4 m for Q = 1.0 L/s discharge up to 2.5 m for Q = 2.0 L/s discharge. Data variability shows constant values and an evident discharge effect is not present both in the mean and variability values.

6.7 Discussion

The calculation of eroded volume is a key parameter in bedload estimates through the implementation of step-length-based methods, and thus bedload estimation can be negatively affected by morphological changes computation. The experiments conducted with a constant sediment flux show that halving the topographic survey frequency does not double the eroded volume (Figure 49). This leads to an underestimation of the sediment flux once the temporal distance between surveys is too long. Since is not possible to increase the survey frequency above the event scale, the possible underestimation have to be taken into account.

This effect is due to the presence of compensation and negatively affects the calculation of the eroded volume. At 4 t / Exner time, the effects of compensation reduce the runs at Q = 0.5 L/s and Q = 0.7 L/s discharge by about 55%, while they reach the 70% for Q = 1.0 L/s,

Q = 1.5 L/s, and Q = 2.0 L/s discharge. Compensation plays an important role not only in the estimation of MAW but also in the calculation of volumes (chapter 4). These effects can be limited by increasing the survey frequency as much as possible. Furthermore, as discussed in section 3.4, the analysed field data show that the event scale for a flood in the studied gravel-bed rivers is around a few Exner times, which is sufficient to develop a considerable underestimation of the eroded volume. Moreover, the results presented in this chapter could help researchers to perform more effective bedload estimations: the effects of compensation and travelling bedload tend to reduce significantly of those rivers that exhibit a low confined flow, with braiding-wandering morphologies.

The comparison between the bedload flux estimation by the morphological method and the solid discharge data measured at the channel outlet during the experiments allowed us to evaluate the effects of the survey frequency on the bedload flux estimation. The bedload flux was estimated using the eroded volume and the path-length was calculated according to the methodology proposed by Capito, Pandrin, et al., 2024. This application should be used with caution. The path length approach can provide useful information on bedload dynamics, but does not represent the tracer's travelled distance. Since it is reasonable to assume that sediment goes from the eroded zone to the deposition zone, the assumption under which this approach is valid is that all the eroded volume goes from the source zone to the deposition zone. Another point that needs further investigation is the eroded volume computation. Assuming that there are not limitations in the time scale at which the morphological changes can be computed, a question remains open: what is the extension of the channel domain over which the eroded volume should be computed? Is this the volume of eroded sediment over which tracers are placed? The erosion patches just upstream? The entire eroded sediment, computed in a channel domain that is large enough to avoid L_C dependencies? If the latter excludes a certain number of uncertainties in the choice (once the eroded patches can be easily identified) of which is the eroded patches that are more related to the tracer's displacement studied, is necessary to assume that the path length used for the computation is representative of the entire domain over which the eroded volume is computed.

It was therefore possible to verify the effectiveness of eroded volume calculation and step-length estimation in the implementation of the morphological method and compare the estimated values with the measured value. Relative errors in the estimation for the lowest flows remain below 15%. For the highest flows, an underestimation of the bedload flux close to 60% is observed. It is possible to interpret these results in the light of the effects of flow confinement on the morphological dynamics. As shown in chapter 4 the effects of compensation increase with flow confinement. This can be interpreted considering that, for higher specific discharge, the current tends to rework the sediment in the same areas. This makes confined systems more prone to manifest compensation processes. In the context of low specific discharge, the current has a greater possibility to migrate laterally. Lateral migration does not produce compensatory effects and this could explain the lower compensation for lower discharge. These results are promising and demonstrate the validity of step-length-based approaches. Furthermore, comparing the measured bedload flux and the estimated bedload flux we point out the effectiveness of calculating the step-length based on the distance between the main depositional areas The presence of compensation leads to a significant decrease in the estimated bedload flux. As the survey frequency decreases,

there is a reduction in the estimate of Qs which is faster the higher the discharge. By decreasing the survey frequency, compensation leads to a reduction in the estimated value of bedload flux. The effects of the greater presence of compensation in more confined systems also have effects on the sediment flux estimate, which drops more drastically than in less confined systems.

The estimation of the path-length using the cumulative sum of erode volume at the finest discretization could lead to further investigations. The path length can be interpreted as a length scale of sediment transport processes and can provide useful insights when coupled with metrics that describe the spatial distribution of morphological units. It would be useful to test this relationship in further experiments, in a wider range of morphology, where sediment transport can be coupled with tracer displacement and repeated topographic surveys.

An important component, as shown in chapter 4, is the one related to the non-morphological component of the bedload. This component does not appear in the bedload flux estimate by the morphological method. For less confined systems, this component is lower (see chapter 4) and could be the reason why the bedload flux estimates for the Q = 0.7 L/s discharge and Q = 0.7 L/s discharge are more accurate. The equilibrium component of the non-morphological bedload could be present even in areas where compensation or morphological bedload occurs.

This leads to a reflection on the application of the morphological method and the expected results. In systems where the morphological component prevails, the morphological method can give good results. In systems in which the non-morphological component is not negligible, the morphological method should be used with caution.

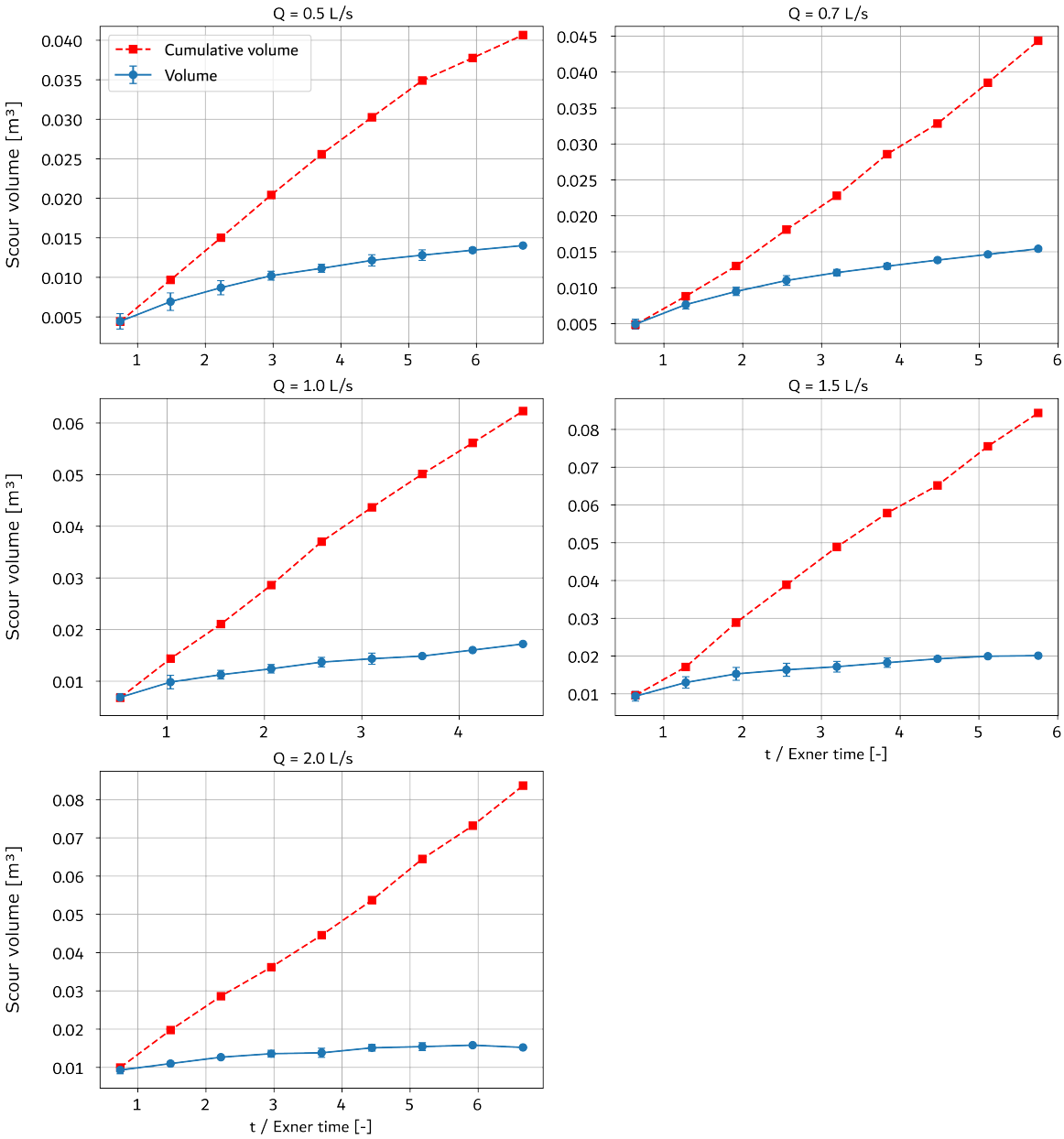

Figure 50 – Compensation volume computed varying survey frequency compared with the cumulative sum of scour volume computed for each run.

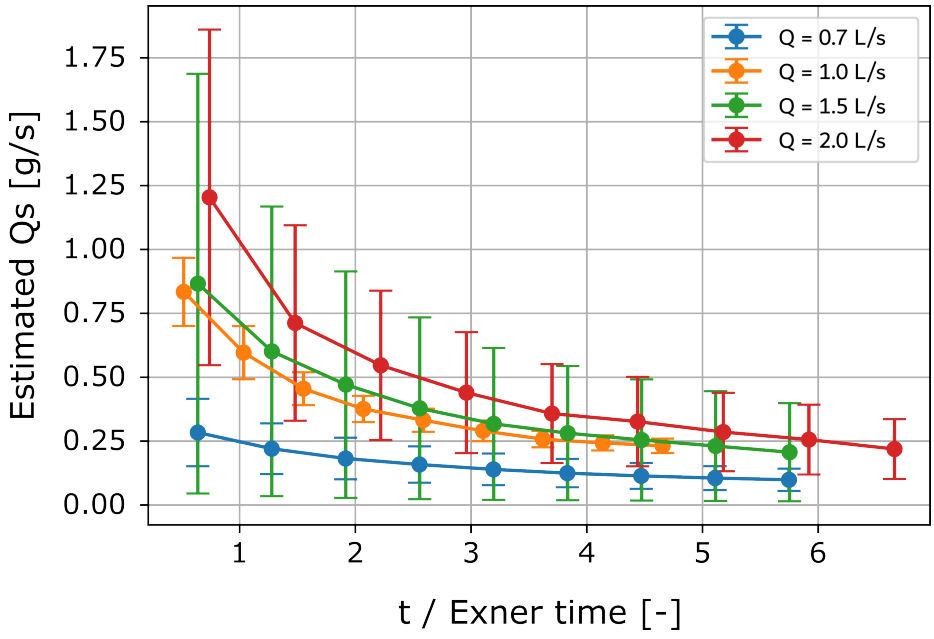

Figure 51 – Estimated bedload flux varying survey frequency in volume computation. Dots represent mean values and whiskers represent data variability.

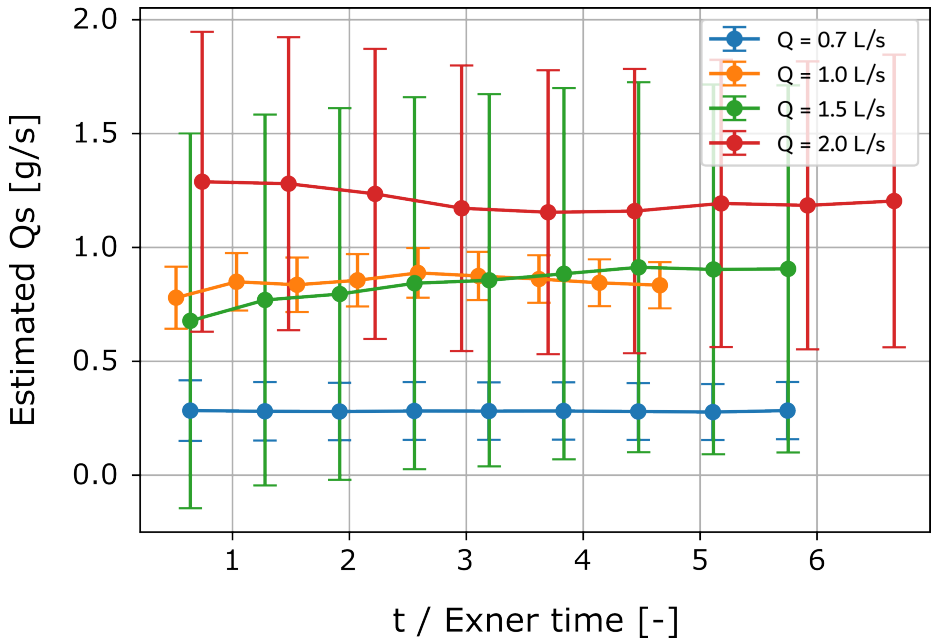

Figure 52 – Estimated bedload flux varying survey frequency in volume computation. Volume is computed as the cumulative sum of eroded volume at the finest temporal discretization. Dots represent mean values and whiskers represent data variability.

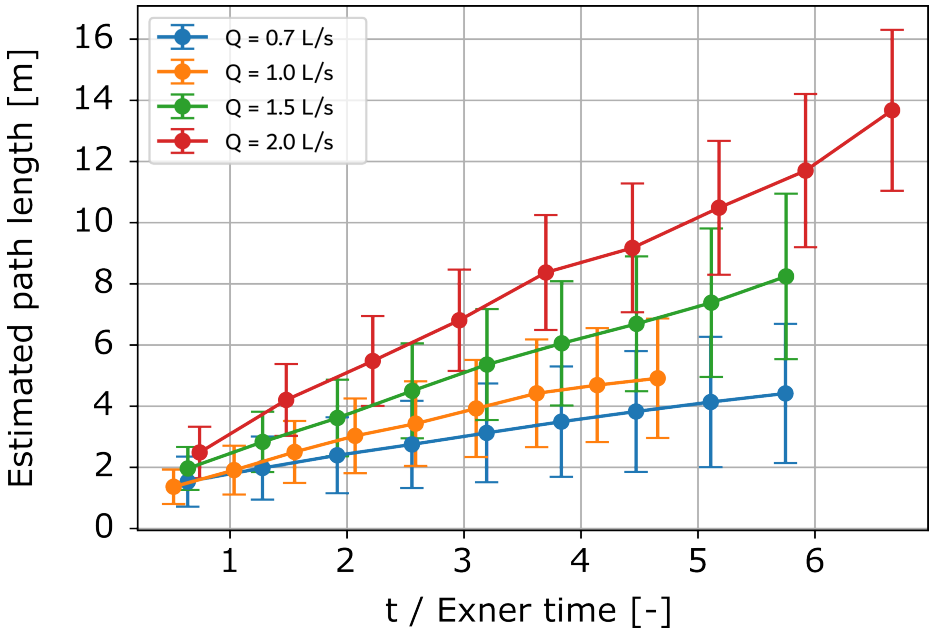

Figure 53 – Estimated path length varying survey frequency in volume computation. Eroded volume is computed from DoDs taken a different timespan. Dots represent mean values and whiskers represent data variability.

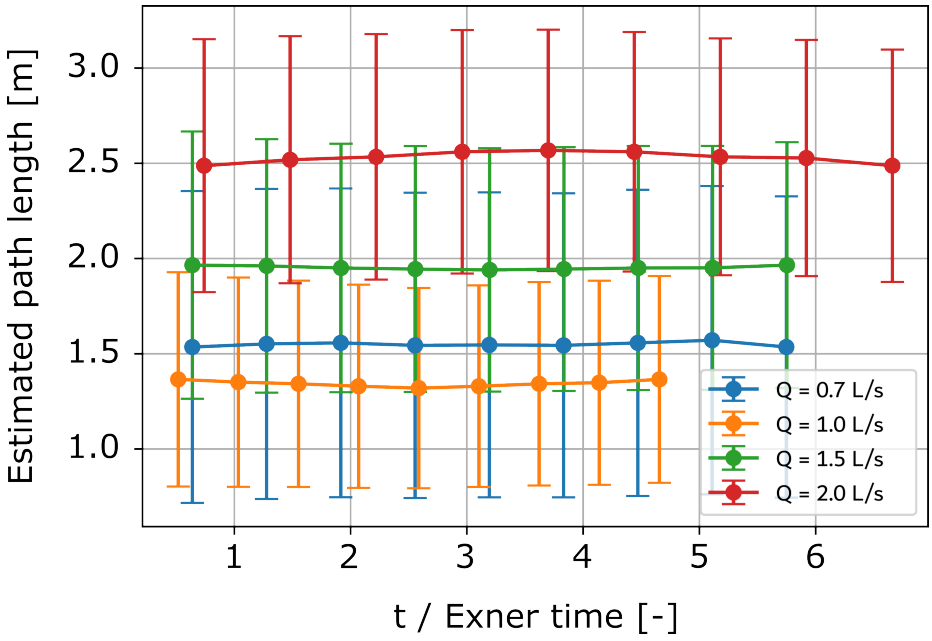

Figure 54 – Estimated path varying survey frequency in volume computation. Volume is computed as the cumulative sum of eroded volume at the finest temporal discretization. Dots represent mean values and whiskers represent data variability.

CHAPTER 7
CONCLUSION

This thesis has aimed to evaluate the relationship between bedload transport and its morphological imprint, a fundamental principle underlying the morphological method. This method estimates bedload flux by analysing morphological variations derived from repeated topographic surveys. Understanding this relationship is crucial for improving the accuracy and applicability of sediment transport assessments in fluvial environments.

In the implementation of the morphological method, the measurement of morphological variations plays a key role. Therefore, assessing what is the minimum size of the analysis domain to obtain effective MAW estimates has considerable practical implications. New survey technologies (LiDAR, drones, etc.) have greatly simplified topographic surveys, allowing for greater speed, lower costs, and greater spatial representativeness. The experiments conducted reveal how, depending on the morphology, the size of the analysis domain that can be considered acceptable varies. For morphologies tending towards alternating bars, only a few widths in terms of longitudinal development of the analysis domain are sufficient to obtain reliable MAW measurements. For morphologies closer to braiding, where the morphological method yields greater results due to the lesser influence of compensation and equilibrium bedload, the minimum length required is around six widths.

The findings of this research underscore the significant role that channel morphology plays in governing bedload transport processes. Specifically, less confined flows exhibit a stronger correlation between the Morphological Active Width (MAW) and the Bedload Active Width (BAW), which has important implications for transport estimates obtained through the morphological method using the virtual velocity approach. Moreover, the study reveals that the effects of compensation, dominant in comparison to those of Digital Elevation Model of Difference (DoD) filtering, tend to decrease in river morphologies characterised by greater lateral mobility. This suggests that flow confinement, and so specific discharge and mobility exert considerable influence on the accuracy of sediment flux estimations derived from morphological observations. In addition to compensation, whose effects and dynamics were studied in this thesis work, an important role in the application of the morphological method is played by the equilibrium bedload. The equilibrium bedload is non-negligible in terms of both area and intensity. The equilibrium bedload can extend up to 40% of the entire area that experienced bedload activity by evaluating a time discretisation of 0.5 Exner time. This percentage tends to decrease rapidly when considering the envelope of morphologically active areas and tends to cancel out around 6 Exner time envelopes for less confined flows. Areas that manifest equilibrium bedload manifest a bedload intensity that is comparable to morphologically active areas, supporting the thesis that equilibrium bedload cannot be neglected. Unlike the effects of compensation, equilibrium bedload has never before been considered as a component that leads to the underestimation of bedload through the application of the morphological method. In particular, the validity of the sediment budgeting approach remains, as the known flow section also includes the equilibrium bedload component. In the virtual velocity method, on the other hand,

the equilibrium bedload component is completely neglected. This leads to considerable underestimation of bedload flux, in particular on those rivers characterised by high flow confinement (high specific discharge). In braiding morphologies or, however, in river characterised by low specific discharge, bedload processes tend to be more morphological. It is likely to be due to the flow confinement: confined flows tend to rework the same sediment since moving laterally is often not possible. This increases non-morphological bedload and equilibrium bedload. Low confined flows have the room to move laterally, a behaviour that reduces and almost eliminates compensation. Bank erosion produces net variations that are easily detected by repeated topographic surveys. In such contexts, the application of the morphological methods produces a more reliable estimation. Moreover, the application of the virtual velocity approach involves the eroded sediment as a proxy of the sediment that moves through a river reach. Reduction of the non-morphological bedload leads to more reliable estimation of the bedload flux. This provides useful insights into the applicability of the virtual velocity approach and may be useful in assessing the reliability of the estimate based on the morphological characteristics and temporal discretisation of the available data.

Additionally, this study highlights the necessity of conducting frequent and spatially extensive topographic surveys to achieve reliable estimates of transported sediment volumes. The incorporation of tracers in laboratory experiments has further elucidated the influence of morphology on bedload dynamics, revealing a strong relationship between path length and the spatial distribution of primary deposition zones. These experimental insights contribute to a more refined understanding of how morphological characteristics regulate sediment transport mechanisms. However, the strong hypothesis at the base of the virtual velocity approach remains: tracers have to describe the entire sediment population for all the entrained grainsize, different feeding points need to be tested to describe the path length of the entrained sediment and an accurate estimation of the eroded sediment through repeated topographic surveys is needed. In particular, I think that the complete description of sediment dynamics through tracer implementation remains challenging due to the high intrinsic variability in bedload. Our outcomes highlighted the influence of bed morphology in tracer displacement that, on the one hand, draws attention to the causes of spatial variability and high complexity, and on the other hand, provides useful insights on field campaign design.

The analyses conducted in this study advance the methodological framework for sediment transport quantification; further investigations are required to address remaining uncertainties. In particular, a more comprehensive understanding of equilibrium transport conditions and their implications for long-term sediment budget assessments is needed. For what concerns the virtual approach, I think that the laboratory scale would help to move steps forward on bedload dynamics through the implementation of tracers. Although energy-demanding, tracers in the laboratory may help researchers fill the gaps that remain in the field application of the virtual velocity approach: the location and number of the feeding points, the extension of the analysis domain and the effects of field related unbeatable limitations (presence of water in the main channel, disturbances in the position of the tracers, low recovery rate, etc.) affect the estimation of bedload flux.

Overall, the results presented in this thesis emphasise the strengths of the morphological method in estimating bedload flux in gravel-bed rivers. By enhancing our ability to quantify

sediment transport through morphological analysis, this research contributes to the broader field of fluvial geomorphology and supports the development of improved management strategies for sediment dynamics in natural river systems.

APPENDIX A

A.1 DEM and DoD scheme

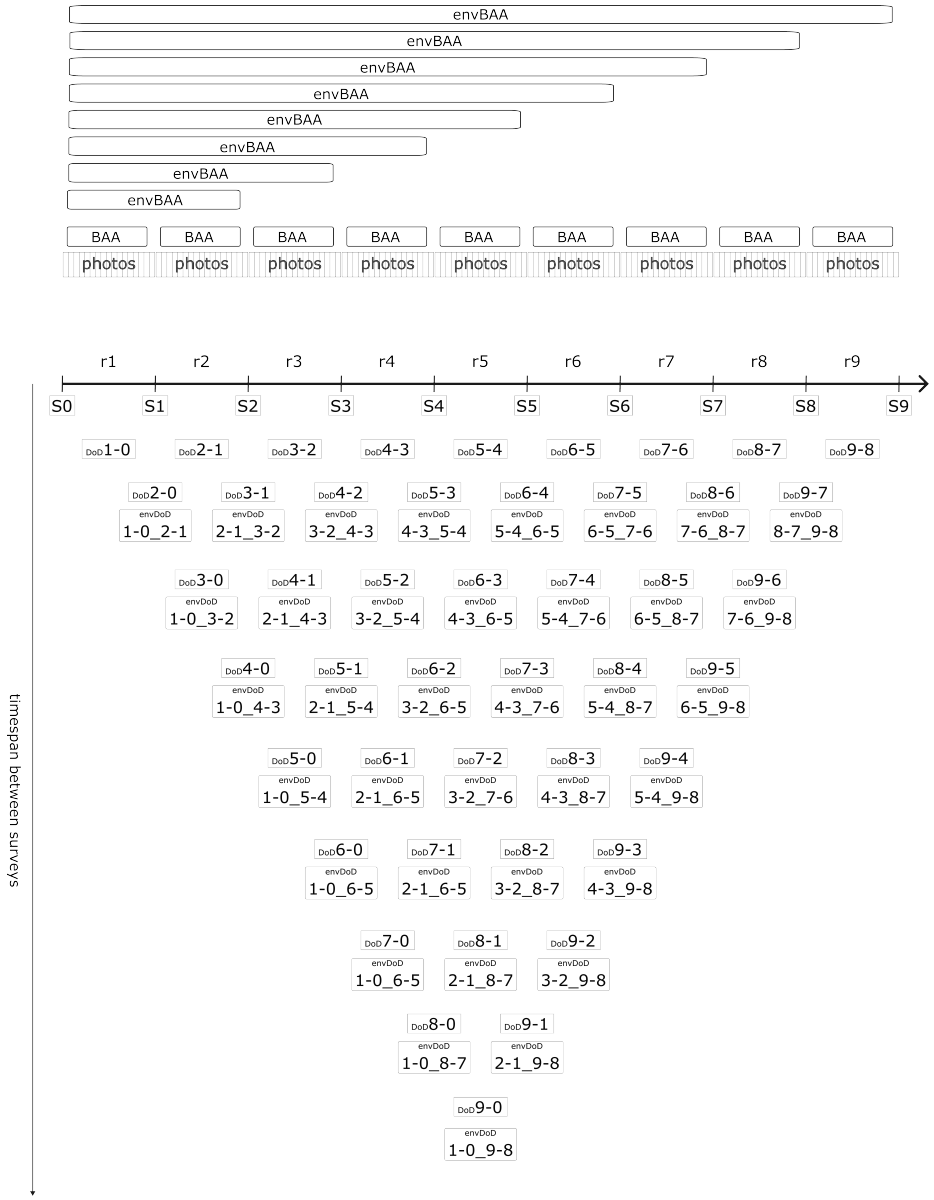

Figure 55 – Topographic and bedload activity data structure.

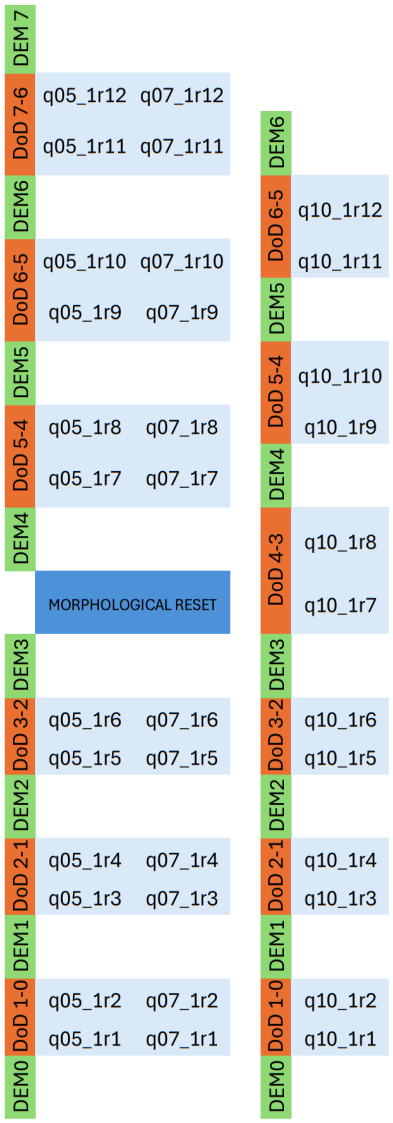

Figure 56 – Tracers experiments structure.

BIBLIOGRAPHY

Anderson & Pitlick. (2014). Using repeat lidar to estimate sediment transport in a steep stream. *J. Geophys. Res. Earth Surf.*, *119*(3), 621–643. https://doi.org/10.1002/2013JF002933

Ashmore. (1991). How Do Gravel-Bed Rivers Braid? *Can. J. Earth Sci.*, *28*(3), 326–341. https://doi.org/10.1139/e91-030

Ashmore. (2013). 9.17 Morphology and Dynamics of Braided Rivers. In *Treatise on Geomorphology* (pp. 289–312). Elsevier. https://doi.org/10.1016/B978-0-12-374739-6.00242-6

Ashmore, Bertoldi, & Gardner. (2011). Active Width of Gravel-Bed Braided Rivers. *Earth Surf. Process. Landforms*, *36*(11), 1510–1521. https://doi.org/10.1002/esp.2182

Ashmore & Church. (1998). Sediment transport and river morphology: A paradigm for study. *Gravel-bed Rivers in the Environment*, *345*, 115–139.

Bertoldi, Ashmore, & Tubino. (2009). A Method for Estimating the Mean Bed Load Flux in Braided Rivers. *Geomorphology*, *103*(3), 330–340. https://doi.org/10.1016/j.geomorph.2008.06.014

Bertoldi, Zanoni, & Tubino, M. (2009). Planform Dynamics of Braided Streams. *Earth Surf. Process. Landforms*, *34*(4), 547–557. https://doi.org/10.1002/esp.1755

Brasington, Vericat, & Rychkov. (2012). Modeling River Bed Morphology, Roughness, and Surface Sedimentology Using High Resolution Terrestrial Laser Scanning. *Water Resour. Res.*, *48*(11). https://doi.org/10.1029/2012WR012223

Brenna, A., & Surian, N. (2023). Coarse sediment mobility and fluxes in wide mountain streams: Insights using the virtual velocity approach. *Geomorphology*, *427*, 108625. https://doi.org/10.1016/j.geomorph.2023.108625

Brenna, A., Surian, N., & Mao, L. (2020). Response of A Gravel - Bed River To Dam Closure: Insights From Sediment Transport Processes And Channel Morphodynamics. *Earth Surf. Process. Landforms*, *45*(3), 756–770. https://doi.org/10.1002/esp.4750

Brenna, Surian, & Mao. (2019). Virtual Velocity Approach for Estimating Bed Material Transport in Gravel-Bed Rivers: Key Factors and Significance. *Water Resour. Res.*, *55*(2), 1651–1674. https://doi.org/10.1029/2018WR023556

Brewer, P. A., & Passmore, D. G. (2002). Sediment Budgeting Techniques in Gravel-Bed Rivers. *Geological Society, London, Special Publications*, *191*(1), 97–113. https://doi.org/10.1144/GSL.SP.2002.191.01.07

Buffington, J. M., & Montgomery, D. R. (1997). A Systematic Analysis of Eight Decades of Incipient Motion Studies, with Special Reference to Gravel-Bedded Rivers. *Water Resour. Res.*, *33*(8), 1993–2029. https://doi.org/10.1029/96WR03190

Bunte & Abt. (2003). Sampler size and sampling time affect bed load transport rates and particle sizes measured with bed load traps in gravel-bed streams. *Erosion and Sediment Transport Measurements in Rivers: Technological and Methodological Advances*, *Proceedings Oslo Workshop 2002*, 126–133.

Bunte, K., & Abt, S. R. (2005). Effect of Sampling Time on Measured Gravel Bed Load Transport Rates in a Coarse-Bedded Stream: Effects of sampling time on measured transport. *Water Resour. Res.*, *41*(11). https://doi.org/10.1029/2004WR003880

Capito, L. M., Bizzi, S., Surian, N., & Bertoldi, W. (2024). Braiding morphological scales is sediment transport: Path length estimation from flume experiments to network-scale sediment transport model validation.

Capito, L. M., Pandrin, E., Bertoldi, W., Surian, N., & Bizzi, S. (2024). Path length and sediment transport estimation from DEMs of difference: A signal processing approach. *Earth Surf. Dynam.*, *12*(1), 321–345. https://doi.org/10.5194/esurf-12-321-2024

Church, M. (2006). Bed material transport and the morphology of alluvial river channel. *Annu. Rev. Earth Planet. Sci.*, *34*(1), 325–354. https://doi.org/10.1146/annurev.earth.33.092203.122721

Church, M., & Hassan, M. A. (1992a). Size and Distance of Travel of Unconstrained Clasts on a Streambed. *Water Resour. Res.*, *28*(1), 299–303. https://doi.org/10.1029/91WR02523

Church, M., & Hassan, M. A. (1992b). Size and distance of travel of unconstrained clasts on a streambed. *Water Resources Research*, *28*(1), 299–303. https://doi.org/10.1029/91WR02523

Curran, J. C., Waters, K. A., & Cannatelli, K. M. (2015). Real time measurements of sediment transport and bed morphology during channel altering flow and sediment transport events. *Geomorphology*, *244*, 169–179. https://doi.org/10.1016/j.geomorph.2015.03.009

Einstein, H. A. (1936). *Der Geschiebetrieb als Wahrscheinlichkeitsproblem*. https://doi.org/10.3929/ETHZ-A-000092036

Erwin, S. O., Schmidt, J. C., Wheaton, J. M., & Wilcock, P. R. (2012). Closing a Sediment Budget for a Reconfigured Reach of the Provo River, Utah, United States. *Water Resour. Res.*, *48*(10), 2011WR011035. https://doi.org/10.1029/2011WR011035

Ferguson, R. I., & Wathen, S. J. (1998). Tracer-Pebble Movement along a Concave River Profile: Virtual Velocity in Relation to Grain Size and Shear Stress. *Water Resour. Res.*, *34*(8), 2031–2038. https://doi.org/10.1029/98WR01283

Ferguson, R. (2003). The Missing Dimension: Effects of Lateral Variation on 1-D Calculations of Fluvial Bedload Transport. *Geomorphology*, *56*(1–2), 1–14. https://doi.org/10.1016/S0169-555X(03)00042-4

Ferguson, R., & Ashworth, P. (1992, January 1). Spatial patterns of bedload transport and channel change in braided and near braided rivers. In P. Billi, R. Hey, C. Thorne, & P. Taconni (Eds.), *Dynamics of gravel-bed rivers* (pp. 477–492). John Wiley and Sons.

Garcia, C., Laronne, J. B., & Sala, M. (1999). Variable source areas of bedload in a gravel-bed stream. *Journal of Sedimentary Research*. https://doi.org/http://dx.doi.org/10.2110/jsr.69.27

Garcia Lugo, G. A., Bertoldi, W., Henshaw, A. J., & Gurnell, A. M. (2015). The Effect of Lateral Confinement on Gravel Bed River Morphology. *Water Resour. Res.*, *51*(9), 7145–7158. https://doi.org/10.1002/2015WR017081

Goff & Ashmore. (1994a). Gravel transport and morphological change in braided sunwapta river, Alberta, Canada. *Earth Surf Processes Landf*, *19*(3), 195–212. https://doi.org/10.1002/esp.3290190302

Goff & Ashmore. (1994b). Gravel Transport and Morphological Change in Braided Sunwapta River, Alberta, Canada. *Earth Surf. Process. Landforms*, *19*(3), 195–212. https://doi.org/10.1002/esp.3290190302

Gomez, B. (1991). Bedload transport. *Earth-Science Reviews*, *31*(2), 89–132. https://doi.org/10.1016/0012-8252(91)90017-A

Grams, P. E., Topping, D. J., Schmidt, J. C., Hazel, J. E., & Kaplinski, M. (2013). Linking morphodynamic response with sediment mass balance on the Colorado River in Marble Canyon: Issues of scale, geomorphic setting, and sampling design. *JGR Earth Surface*, *118*(2), 361–381. https://doi.org/10.1002/jgrf.20050

Habersack & Laronne, J. B. (2001). Bed Load Texture in an Alpine Gravel Bed River. *Water Resour. Res.*, *37*(12), 3359–3370. https://doi.org/10.1029/2001WR000260

Habersack, Nachtneb El, H., & Laronne, J. (2001). The continuous measurement of bedload discharge in a large alpine gravel bed river. *Journal of Hydraulic Research*, *39*(2), 125–133. https://doi.org/10.1080/00221680109499813

Haschenburger, J. K., & Church, M. (1998). Bed Material Transport Estimated from the Virtual Velocity of Sediment. *Earth Surf. Process. Landforms*, *23*(9), 791–808. https://doi.org/10.1002/(SICI)1096-9837(199809)23:9<791::AID-ESP888>3.0.CO;2-X

Hassan, M. A., & Bradley, D. N. (2017, May 6). Geomorphic Controls on Tracer Particle Dispersion in Gravel-Bed Rivers. In D. Tsutsumi & J. B. Laronne (Eds.), *Gravel-Bed Rivers* (pp. 159–184). John Wiley & Sons, Ltd. https://doi.org/10.1002/9781118971437.ch6

Hassan, M. A., Church, M., & Ashworth, P. J. (1992). Virtual Rate and Mean Distance of Travel of Individual Clasts in Gravel-Bed Channels. *Earth Surf. Process. Landforms*, *17*(6), 617–627. https://doi.org/10.1002/esp.3290170607

Hassan, M. A., & Ergenzinger, P. (2005). Use of Tracers in Fluvial Geomorphology. In G. M. Kondolf & H. Piégay (Eds.), *Tools in Fluvial Geomorphology* (pp. 397–423). John Wiley & Sons, Ltd. https://doi.org/10.1002/0470868333.ch14

Hassan, M. A., & Roy, A. G. (2016, April 6). Coarse Particle Tracing in Fluvial Geomorphology. In G. M. Kondolf & H. Piégay (Eds.), *Tools in Fluvial Geomorphology* (1st ed., pp. 306–323). Wiley. https://doi.org/10.1002/9781118648551.ch14

Heinzel, G., Rudiger, A., & Schilling, R. (2002). Spectrum and spectral density estimation by the Discrete Fourier transform (DFT), including a comprehensive list of window functions and some new flat-top windows.

Helley, E., & Winchell, S. (1971). *Development and calibration of a pressure-difference bedload sampler*. 10.3133/ofr73108

Hergault, V., Frey, P., Métivier, F., Barat, C., Ducottet, C., Böhm, T., & Ancey, C. (2010). Image processing for the study of bedload transport of two-size spherical particles in a supercritical flow. *Exp Fluids*, *49*(5), 1095–1107. https://doi.org/10.1007/s00348-010-0856-6

Hubbell, D. W. (1964). Apparatus and Techniques for Measuring Bedload. *United States Government Printing Office*.

Kasprak, A., Wheaton, J. M., Ashmore, P. E., Hensleigh, J. W., & Peirce, S. (2015). The Relationship between Particle Travel Distance and Channel Morphology: Results from Physical Models of Braided Rivers. *J. Geophys. Res. Earth Surf.*, *120*(1), 55–74. https://doi.org/10.1002/2014JF003310

Kondolf, G. M. (2016). Tools in Fluvial Geomorphology. *John Wiley & Sons, Ltd*, 568.

Lamarre, H., & Roy, A. G. (2008). The role of morphology on the displacement of particles in a step–pool river system. *Geomorphology*, *99*(1–4), 270–279. https://doi.org/10.1016/j.geomorph.2007.11.005

Lane, B., Guillon, H., Byrne, C., Pasternack, G. B., Kasprak, A., & Sandoval-Solis, S. (2022). Channel-reach Morphology and Landscape Properties Are Linked across a Large Heterogeneous Region. *Earth Surf Processes Landf*, *47*(1), 257–274. https://doi.org/10.1002/esp.5246

Lane, S. N., Richards, K. S., & Chandler, J. H. (1995). Morphological Estimation of the Time-Integrated Bed Load Transport Rate. *Water Resources Research*, *31*(3), 761–772. https://doi.org/10.1029/94WR01726

Lane, S. N., Westaway, R. M., & Murray Hicks, D. (2003). Estimation of Erosion and Deposition Volumes in a Large, Gravel-Bed, Braided River Using Synoptic Remote Sensing. *Earth Surf. Process. Landforms*, *28*(3), 249–271. https://doi.org/10.1002/esp.483

Laronne, J., Outhet, D., Carling, P., & McCabe, T. (1994). Scour Chain Employment in Gravel Bed Rivers. *CATENA*, *22*(4), 299–306. https://doi.org/10.1016/0341-8162(94)90040-X

Liébault, F., Bellot, H., Chapuis, M., Klotz, S., & Deschâtres, M. (2012). Bedload Tracing in a High-Sediment-Load Mountain Stream. *Earth Surf. Process. Landforms*, *37*(4), 385–399. https://doi.org/10.1002/esp.2245

Liébault, F., Piégay, H., Cassel, M., & Arnaud, F. (2024). Bedload tracing with RFID tags in gravel-bed rivers: Review and meta-analysis after 20 years of field and laboratory experiments. *Earth Surf Processes Landf*, *49*(1), 147–169. https://doi.org/10.1002/esp.5704

Lindsay & Ashmore. (2002). The Effects of Survey Frequency on Estimates of Scour and Fill in a Braided River Model. *Earth Surf. Process. Landforms*, *27*(1), 27–43. https://doi.org/10.1002/esp.282

Lucía, A., Recking, A., Martín-Duque, J. F., Storz-Peretz, Y., & Laronne, J. B. (2013). Continuous monitoring of bedload discharge in a small, steep sandy channel. *Journal of Hydrology*, *497*, 37–50. https://doi.org/10.1016/j.jhydrol.2013.05.034

Mao, L., Picco, L., Lenzi, M. A., & Surian, N. (2017). Bed material transport estimate in large gravel-bed rivers using the virtual velocity approach. *Earth Surf Processes Landf*, *42*(4), 595–611. https://doi.org/10.1002/esp.4000

Mao, L., & Surian, N. (2010). Observations on sediment mobility in a large gravel-bed river. *Geomorphology*, *114*(3), 326–337. https://doi.org/10.1016/j.geomorph.2009.07.015

Mao, L., Toro, M., Carrillo, R., Brardinoni, F., & Fraccarollo, L. (2020). Controls Over Particle Motion and Resting Times of Coarse Bed Load Transport in a Glacier-Fed Mountain Stream. *J. Geophys. Res. Earth Surf.*, *125*(4). https://doi.org/10.1029/2019JF005253

McDowell, C., Gaeuman, D., & Hassan, M. A. (2021). Linkages between Bedload Displacements and Topographic Change. *Earth Surf Processes Landf*, *46*(15), 3127–3142. https://doi.org/10.1002/esp.5221

McDowell, C., & Hassan, M. A. (2020). The Influence of Channel Morphology on Bedload Path Lengths: Insights from a Survival Process Model. *Earth Surf. Process. Landforms*, *45*(12), 2982–2997. https://doi.org/10.1002/esp.4946

McLean, D. G., & Church, M. (1999). Sediment transport along lower Fraser River: 2. Estimates based on the long-term gravel budget. *Water Resources Research*, *35*(8), 2549–2559. https://doi.org/10.1029/1999WR900102

McQueen, R., Ashmore, P., Millard, T., & Goeller, N. (2021). Bed Particle Displacements and Morphological Development in a Wandering Gravel-Bed River. *Water Res.*, *57*(2). https://doi.org/10.1029/2020WR027850

Merz, J. E., Pasternack, G. B., & Wheaton, J. M. (2006). Sediment budget for salmonid spawning habitat rehabilitation in a regulated river. *Geomorphology*, *76*(1–2), 207–228. https://doi.org/10.1016/j.geomorph.2005.11.004

Middleton, L., Ashmore, P., Leduc, P., & Sjogren, D. (2019). Rates of planimetric change in a proglacial gravel-bed braided river: Field measurement and physical modelling. *Earth Surf Processes Landf*, *44*(3), 752–765. https://doi.org/10.1002/esp.4528

Milan, D. J. (2013). Sediment routing hypothesis for pool-riffle maintenance. *Earth Surf Processes Landf*, *38*(14), 1623–1641. https://doi.org/10.1002/esp.3395

Neill, C. R. (1971). River bed transport related to meander migration rates. *Journal of the Waterways, Harbors and Coastal Engineering Division*, *97*(4), 783–786. https://doi.org/10.1061/AWHCAR.0000135

Nicholas, A., & Sambrook Smith, G. (1998). Relationships between flow hydraulics, sediment supply, bedload transport and channel stability in the proglacial virkisa river, iceland. *Geografiska Annaler: Series A, Physical Geography*, *80*(2), 111–122. https://doi.org/10.1111/j.0435-3676.1998.00030.x

Pandrin, E., & Bertoldi, W. (2024). Are we measuring morphological changes in gravel bed rivers with the appropriate frequency? In *River Flow 2022* (1st ed.). CRC Press, Taylor & Francis.

Paola, C., Straub, K., Mohrig, D., & Reinhardt, L. (2009). The "unreasonable effectiveness" of stratigraphic and geomorphic experiments. *Earth-Science Reviews*, *97*(1–4), 1–43. https://doi.org/10.1016/j.earscirev.2009.05.003

Papangelakis, E., & Hassan, M. A. (2016). The Role of Channel Morphology on the Mobility and Dispersion of Bed Sediment in a Small Gravel-Bed Stream: Role of Morphology on the Mobility and Dispersion of Bed Sediment. *Earth Surf. Process. Landforms*, *41*(15), 2191–2206. https://doi.org/10.1002/esp.3980

Papanicolaou, A. N., Diplas, P., Balakrishnan, M., & Dancey, C. L. (1999). Computer Vision Technique for Tracking Bed Load Movement. *J. Comput. Civ. Eng.*, *13*(2), 71–79. https://doi.org/10.1061/(ASCE)0887-3801(1999)13:2(71)

Parker, G. (1990). Surface-based bedload transport relation for gravel rivers. *Journal of Hydraulic Research*, *28*(4), 417–436. https://doi.org/10.1080/00221689009499058

Passalacqua, P., Belmont, P., Staley, D. M., Simley, J. D., Arrowsmith, J. R., Bode, C. A., Crosby, C., DeLong, S. B., Glenn, N. F., Kelly, S. A., Lague, D., Sangireddy, H., Schaffrath, K., Tarboton, D. G., Wasklewicz, T., & Wheaton, J. M. (2015). An-

alyzing high resolution topography for advancing the understanding of mass and energy transfer through landscapes: A review. *Earth-Science Reviews*, *148*, 174–193. https://doi.org/10.1016/j.earscirev.2015.05.012

Peirce. (2017). *Morphological Bedload Transport in Gravel-Bed Braided Rivers*.

Peirce, S., Ashmore, P., & Leduc, P. (2018). The Variability in the Morphological Active Width: Results from Physical Models of Gravel-Bed Braided Rivers: Morphological Active Width: Physical Models of Braided Rivers. *Earth Surf. Process. Landforms*, *43*(11), 2371–2383. https://doi.org/10.1002/esp.4400

Pierce, J. K., & Hassan, M. A. (2020). Back to Einstein: Burial-Induced Three-Range Diffusion in Fluvial Sediment Transport. *Geophys. Res. Lett.*, *47*(15). https://doi.org/10.1029/2020GL087440

Piton, G., & Recking, A. (2016). Design of Sediment Traps with Open Check Dams. I: Hydraulic and Deposition Processes. *J. Hydraul. Eng.*, *142*(2), 04015045. https://doi.org/10.1061/(ASCE)HY.1943-7900.0001048

Piton, G., & Recking, A. (2017). The Concept of Travelling Bedload and Its Consequences for Bedload Computation in Mountain Streams: HOW TO ACCOUNT FOR ALLOGENIC SUPPLY IN BEDLOAD TRANSPORT EQUATIONS? *Earth Surf. Process. Landforms*, *42*(10), 1505–1519. https://doi.org/10.1002/esp.4105

Pyrce & Ashmore. (2003). Particle Path Length Distributions in Meandering Gravel-Bed Streams: Results from Physical Models. *Earth Surf. Process. Landforms*, *28*(9), 951–966. https://doi.org/10.1002/esp.498

Pyrce, R. S., & Ashmore, P. E. (2003). The Relation between Particle Path Length Distributions and Channel Morphology in Gravel-Bed Streams: A Synthesis. *Geomorphology*, *56*(1–2), 167–187. https://doi.org/10.1016/S0169-555X(03)00077-1

Pyrce, R. S., & Ashmore, P. E. (2005). Bedload Path Length and Point Bar Development in Gravel-Bed River Models. *Sedimentology*, *52*(4), 839–857. https://doi.org/10.1111/j.1365-3091.2005.00714.x

Radice, A., Malavasi, S., & Ballio, F. (2006). Solid transport measurements through image processing. *Exp Fluids*, *41*(5), 721–734. https://doi.org/10.1007/s00348-006-0195-9

Redolfi, M. (2014). *New Methods for the Analysis of Braided Rivers Morphodynamics.* [Doctoral dissertation, University of Trento].

Redolfi, M., Guidorizzi, L., Tubino, M., & Bertoldi, W. (2017). Capturing the Spatiotemporal Variability of Bedload Transport: A Time-Lapse Imagery Technique. *Earth Surf. Process. Landforms*, *42*(7), 1140–1147. https://doi.org/10.1002/esp.4126

Reid, I., Layman, J. T., & Frostick, L. E. (1980). The Continuous Measurement Of Bedload Discharge. *Journal of Hydraulic Research*, *18*(3), 243–249. https://doi.org/10.1080/00221688009499550

Rickenmann, D., Turowski, J. M., Fritschi, B., Klaiber, A., & Ludwig, A. (2012). Bedload transport measurements at the Erlenbach stream with geophones and automated basket samplers. *Earth Surf Processes Landf*, *37*(9), 1000–1011. https://doi.org/10.1002/esp.3225

Savitzky, Abraham., & Golay, M. J. E. (1964). Smoothing and Differentiation of Data by Simplified Least Squares Procedures. *Anal. Chem.*, *36*(8), 1627–1639. https://doi.org/10.1021/ac60214a047

Vázquez-Tarrío, D., & Batalla, R. J. (2019). Assessing Controls on the Displacement of Tracers in Gravel-Bed Rivers. *Water*, *11*(8), 1598. https://doi.org/10.3390/w11081598

Vázquez-Tarrío, D., Recking, A., Liébault, F., Tal, M., & Menéndez-Duarte, R. (2019). Particle Transport in Gravel-Bed Rivers: Revisiting Passive Tracer Data: Particle Transport in Gravel-Bed Rivers. *Earth Surf. Process. Landforms*, *44*(1), 112–128. https://doi.org/10.1002/esp.4484

Vericat, D., Church, M., & Batalla, R. J. (2006). Bed load bias: Comparison of measurements obtained using two (76 and 152 mm) Helley-Smith samplers in a gravel bed river. *Water Resources Research*, *42*(1), 2005WR004025. https://doi.org/10.1029/2005WR004025

Vericat, D., & Batalla, R. J. (2010). Sediment transport from continuous monitoring in a perennial Mediterranean stream. *CATENA*, *82*(2), 77–86. https://doi.org/10.1016/j.catena.2010.05.003

Vericat, D., Wheaton, J. M., & Brasington, J. (2017). Revisiting the Morphological Approach: Opportunities and Challenges with Repeat High-Resolution Topography. In D. Tsutsumi & J. B. Laronne (Eds.), *Gravel-Bed Rivers* (pp. 121–158). John Wiley & Sons, Ltd. https://doi.org/10.1002/9781118971437.ch5

Wilcock, P. R. (2001). Toward a Practical Method for Estimating Sediment-Transport Rates in Gravel-Bed Rivers. *Earth Surf. Process. Landforms*, *26*(13), 1395–1408. https://doi.org/10.1002/esp.301

Williams. (2012). DEMs of Difference. *British Society for Geomorphology*.

Williams, Rennie, C. D., Brasington, J., Hicks, D. M., & Vericat, D. (2015). Linking the spatial distribution of bed load transport to morphological change during high-flow events in a shallow braided river. *JGR Earth Surface*, *120*(3), 604–622. https://doi.org/10.1002/2014JF003346

Wohl, E., Bledsoe, B. P., Jacobson, R. B., Poff, N. L., Rathburn, S. L., Walters, D. M., & Wilcox, A. C. (2015). The Natural Sediment Regime in Rivers: Broadening the Foundation for Ecosystem Management. *BioScience*, *65*(4), 358–371. https://doi.org/10.1093/biosci/biv002

Zaidan, J., Poupardin, A., Bennabi, A., Marin, F., & Benamar, A. (2024). Novel 3D Structural-Light Scanner Technique for Continuous Monitoring of Pier Scour in Laboratory. *JMSE*, *12*(9), 1566. https://doi.org/10.3390/jmse12091566